SORPTION ENHANCED CHEMICAL LOOPING STEAM ETHANOL REFORMING FOR HYDRO
GEN PRODUCTION USING CALCIUM OXIDE/NICKEL OXIDE/IRON OXIDE MULTIFUNCTIO
NAL CATALYST

Miss Janenipa Saupsor

A Dissertation Submitted in Partial Fulfillment of the Requirements
for the Degree of Doctor of Engineering in Chemical Engineering
Department of Chemical Engineering
FACULTY OF ENGINEERING
Chulalongkorn University
Academic Year 2019

การปฏิรูปเอทานอลด้วยไอน้ำแบบเคมิคอลลูปปิงที่ส่งเสริมด้วยการดูดซับเพื่อผลิตแก๊สไฮโดรเจน ด้วยตัวเร่งปฏิกิริยาหลายหน้าที่ แคลเซียมออกไซด์/นิกเกิลออกไซด์/เหล็กออกไซด์

น.ส.เจนนิภา สืบเสาะ

วิทยานิพนธ์นี้เป็นส่วนหนึ่งของการศึกษาตามหลักสูตรปริญญาวิศวกรรมศาสตรดุษฎีบัณฑิต
สาขาวิชาวิศวกรรมเคมี ภาควิชาวิศวกรรมเคมี
คณะวิศวกรรมศาสตร์ จุฬาลงกรณ์มหาวิทยาลัย
ปีการศึกษา 2562
ลิขสิทธิ์ของจุฬาลงกรณ์มหาวิทยาลัย

Thesis Title	SORPTION ENHANCED CHEMICAL LOOPING STEAM ETHA NOL REFORMING FOR HYDROGEN PRODUCTION USING CALCIUM OXIDE/NICKEL OXIDE/IRON OXIDE MULTIFUNC TIONAL CATALYST
By	Miss Janenipa Saupsor
Field of Study	Chemical Engineering
Thesis Advisor	Professor Suttichai Assabumrungrat, Ph.D.

Accepted by the FACULTY OF ENGINEERING, Chulalongkorn University in Partial Fulfillment of the Requirement for the Doctor of Engineering

.... Dean of the FACULTY OF

ENGINEERING

(Associate Professor Supot Teachavorasinskun, D.Eng.)

DISSERTATION COMMITTEE

.... Chairman

(Assistant Professor Worapon Kiatkittipong, Ph.D.)

.... Thesis Advisor

(Professor Suttichai Assabumrungrat, Ph.D.)

.... Examiner

(Associate Professor Anongnat Somwangthanaroj, Ph.D.)

.... Examiner

(Associate Professor Kasidit Nootong, Ph.D.)

.... Examiner

(Rungthiwa Methaapanon, Ph.D.)

เจนนิภา สืบเสาะ : การปฏิรูปเอทานอลด้วยไอน้ำแบบเคมิคอลลูปปิงที่ส่งเสริมด้วยการดูดซับเพื่อ
ผลิตแก๊สไฮโดรเจน ด้วยตัวเร่งปฏิกิริยาหลายหน้าที่ แคลเซียมออกไซด์/นิกเกิลออกไซด์/เหล็ก
ออกไซด์. (
SORPTION ENHANCED CHEMICAL LOOPING STEAM ETHANOL REFORMING FOR HYDR
OGEN PRODUCTION USING CALCIUM OXIDE/NICKEL OXIDE/IRON OXIDE MULTIFUNCTI
ONAL CATALYST) อ.ที่ปรึกษาหลัก : ศ. ดร.สุทธิชัย อัสสะบำรุงรัตน์

งานวิจัยนี้เป็นการศึกษากระบวนการปฏิรูปเอทานอลแบบเคมิคอลลูปปิงที่ส่งเสริมด้วยการดูดซับเพื่อ
ผลิตแก๊สไฮโดรเจนซึ่งทำการศึกษาทั้งด้านการใช้เครื่องมือทางคอมพิวเตอร์เข้าช่วยและการทดลอง โดย
แบบจำลองของสี่กระบวนการในการผลิตแก๊สไฮโดรเจนได้ถูกสร้างในโปรแกรมทางคอมพิวเตอร์ ประกอบไปด้วย
แบบจำลองของกระบวนการผลิตแบบดั้งเดิมอย่างกระบวนการปฏิรูปเอทานอลด้วยไอน้ำและแบบจำลองของ
กระบวนการที่พัฒนาแล้วอีกสามกระบวนการ ได้แก่ กระบวนการปฏิรูปเอทานอลด้วยไอน้ำที่ส่งเสริมด้วยการดูด
ซับ กระบวนการปฏิรูปเอทานอลแบบเคมิคอลลูปปิงและกระบวนการปฏิรูปเอทานอลแบบเคมิคอลลูปปิงที่
ส่งเสริมด้วยการดูดซับ โดยใช้นิกเกิลออกไซด์เป็นตัวนำพาออกซิเจนและใช้แคลเซียมออกไซด์เป็นตัวดูดซับ ซึ่ง
กระบวนการทั้งหมดจะถูกพิจารณาภายใต้การดำเนินการแบบไม่ต้องการความร้อนจากภายนอก โดยความ
ต้องการพลังงานของกระบวนการผลิตนั้นจะได้มาจากพลังงานที่ได้จากการเผาไหม้ของแก๊สไฮโดรเจนที่ผลิต
ออกมาบางส่วน ซึ่งประสิทธิภาพของกระบวนการจะทำการพิจารณาที่สภาวะที่ให้ปริมาณไฮโดรเจนสุทธิมากที่สุด
หลังจากหักปริมาณที่ใช้ไปในการเผาไหม้แล้ว และในส่วนของการทดลองนั้นได้มุ่งเน้นศึกษาตัวนำพาออกซิเจนที่
เป็นเหล็กออกไซด์เนื่องจากมีปริมาณออกซิเจนเป็นองค์ประกอบที่สูง ซึ่งในการที่จะรวมตัวนำพาออกซิเจนกับตัว
ดูดซับแคลเซียมออกไซด์เข้าด้วยกันนั้นจะถูกจำกัดประสิทธิภาพจากแรงอันตรกิริยาระหว่างเหล็กและแคลเซียม
ทำให้ความน่าสนใจของตัวเร่งปฏิกิริยานี้ลดลง ดังนั้นในงานนี้จึงศึกษาผลกระทบของวิธีการเตรียมและปริมาณ
ของเหล็กที่มีผลต่อความว่องไวและเสถียรภาพทางความร้อนของตัวเร่งปฏิกิริยาหลายหน้าที่นี้ ซึ่งจากการทดลอง
พบว่าการเตรียมตัวเร่งปฏิกิริยาด้วยวิธีการฝังตัวของเหล็กที่ปริมาณที่ 5 เปอร์เซ็นต์โดยน้ำหนักจะให้ผลการทดลอง
ที่ดีที่สุด แต่อย่างไรก็ตามเมื่อทำการทดลองซ้ำหลายรอบก็ยังพบการลดลงของปริมาณแก๊สไฮโดรเจนที่ได้และการ
เสื่อมสภาพของตัวเร่งปฏิกิริยา ด้วยเหตุนี้เองจึงได้ทำการพัฒนาประสิทธิภาพของตัวเร่งปฏิกิริยาเพิ่มเติมโดยการ
สังเคราะห์จากสารตั้งต้นไฮโดรทัลไซต์และทำการรวมโลหะระหว่างเหล็กและนิกเกิล ซึ่งผลการทดลองที่ได้แสดง
ให้เห็นถึงความสามารถด้านเสถียรภาพทางความร้อนและการนำกลับมาใช้ซ้ำของตัวเร่งปฏิกิริยาโดยสามารถ
รักษาความสามารถในการเลือกเกิดของแก๊สไฮโดรเจนได้มากถึง 10 รอบ

สาขาวิชา   วิศวกรรมเคมี   ลายมือชื่อนิสิต ....

ปีการศึกษา   2562   ลายมือชื่อ อ.ที่ปรึกษาหลัก ....

5871403021 : MAJOR CHEMICAL ENGINEERING

KEYWORD: HYDROGEN PRODUCTION/ SORPTION ENHANCED CHEMICAL LOOPING REFORMING/ SECLR/ ETHANOL/ MULTIFUNCTIONAL CATALYST

Janenipa Saupsor :
SORPTION ENHANCED CHEMICAL LOOPING STEAM ETHANOL REFORMING FOR HYDROGEN PRODUCTION USING CALCIUM OXIDE/NICKEL OXIDE/IRON OXIDE MULTIFUNCTIONAL CATALYST. Advisor: Prof. Suttichai Assabumrungrat, Ph.D.

This research studied the hydrogen production via sorption enhanced chemical looping reforming process from ethanol both computationally and experimentally. In the computer simulation work, four hydrogen production processes including conventional ethanol steam reforming (ESR), sorption enhanced steam reforming (SESR), chemical looping reforming (CLR) and sorption enhanced chemical looping reforming (SECLR) were performed using NiO as the oxygen carrier and CaO as the CO_2 sorbent, and simulated on the basis of energy self-sufficiency, i.e. process energy requirement supplied by burning some of the produced hydrogen. The process performances in terms of hydrogen productivity, hydrogen purity, ethanol conversion, CO_2 capture ability and thermal efficiency were compared at their maximized net hydrogen. In the experimental studies, Fe-based oxygen carrier was selected due to its high oxygen content. In order to combine with modified CaO sorbent, the limited integration from Fe and Ca interactions makes them less attractive and reliable. The investigation of different combination method (sol-gel, mechanical mixing and impregnation) and iron contents (5, 10 and 15 wt %) of Fe_2O_3/CaO-Al_2O_3 multifunctional catalysts were demonstrated and compared their activity and stability. Higher performance was found for multifunctional catalyst combined by impregnation method with 5 wt % Fe loading. Nevertheless, the H_2 production was still inhibited and the deactivated catalyst was observed. Therefore, the catalyst was further developed to enhance its stability and regenerability for hydrogen production by utilization of hydrotalcite structure. Moreover, alloying Fe with Ni was also applied to improve the catalytic performance. This catalyst showed a stable behavior and maintained hydrogen selectivity over 10 repeated cycles.

Field of Study:	Chemical Engineering	Student's Signature	....
Academic Year:	2019	Advisor's Signature	....

ACKNOWLEDGEMENTS

TABLE OF CONTENTS

LIST OF TABLES

LIST OF FIGURES

CHAPTER I

INTRODUCTION

1.1   Rationale

The energy demand has been increasing for decades due to the world population growth, the development of industrialization and technological breakthrough. Nowadays, fossil fuels are the primary sources of energy which are non-renewable since they were formed by natural processes with long period of time, millions of years. Therefore, the energy consumption and energy resource availability are in reverse directions. Moreover, the combustion of fossil fuels such as coal, oil and natural gas releases carbon dioxide, a greenhouse gas, into the atmosphere leading to the global warming and climate changes which are presently our serious environmental concerns. As the fossil fuels are being depleted, the alternative fuels are currently of interest to replace fossil fuel and supplement for global energy demand [1,2].

Hydrogen is an attractive alternative fuel. It is a composition of many other fuels as all hydrocarbon fuels are molecular combinations between carbon and hydrogen atoms and has high heating value for its combustion. The combustion of hydrogen (Eq. 1.1) is known as clean energy because of emitting only steam without greenhouse gas [3].

$$\text{Combustion of hydrogen:} \quad 2H_2 + O_2 \leftrightarrow 2H_2O \quad \Delta H_r^0 = \text{-286 kJ/mol-}H_2 \quad (1.1)$$
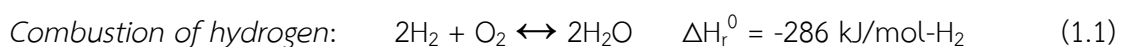
Hydrogen is widely used as a raw material in many industrial processes for example in production of fertilizer, petrochemical and upgrading of refined product and direct fuels in fuel cell applications. Hydrogen can be produced by various feedstocks such as natural gas (mainly methane), bio-oil and biomass [4-6]. The hydrogen generated from renewable energy sources like biomass is considered renewable. It therefore plays an important role in the sustainable energy system. Bioethanol is an interesting feedstock for hydrogen production due to less hazard, high energy density, high solubility in water, relatively safely of storage and transportation and low cost as well as it can be produced from a variety of biomass sources [7, 8].

There are several methods to produce hydrogen such as electrolysis, thermolysis, photo-catalysis, coal gasification and fossil fuels reforming [9, 10]. However, the ninety-five percentage of hydrogen produced in the United State is made by steam reforming process (SR) [11-13]. The steam reforming (Eq. 1.2) process which is the reaction between fuel and steam is considered the most extensively employed pathway to produce hydrogen or synthesis gas. The products from this process depend on several factors such as catalysts, reactors and operating condition which include temperature, pressure and steam to carbon ratio of feed stream. In the sequence, the water gas shift reaction (Eq. 1.3) converts carbon monoxide to produce more hydrogen.

Steam reforming: $Fuel + aH_2O \longrightarrow bCO_x + cH_2$ (1.2)

Water gas shift: $CO + H_2O \longrightarrow CO_2 + H_2$ (1.3)
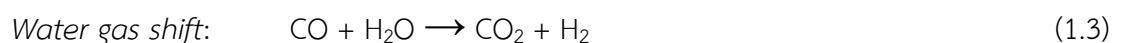
However, the conventional steam reforming process suffers from many disadvantages such as there are multiple steps including reforming step, water gas shift step (including high-temperature shift and low-temperature shift) and purification to purify hydrogen. It also requires severe operating conditions (up to $1000^{\circ}C$), consumes high amount of energy and releases the carbon dioxide gas [14, 15]. The sorption enhanced steam reforming (SESR) process combining steam reforming reaction with carbon dioxide separation by addition of carbon dioxide sorbent into the system has been proposed to improve the conventional steam reforming process. The *in situ* carbon dioxide capture drives the equilibrium of reforming reaction toward higher conversion based on Le Chatelier's principle resulting in high purity of hydrogen and can provide heat to endothermic reforming reaction as the sorbent's carbonation reaction is a strongly exothermic reaction [16-18]. Therefore, this process enables operation at lower temperature. Several carbon dioxide sorbents for high temperature have been extensively investigated. The desired properties of adsorbent are i) high carbon dioxide capacity and selectivity, ii) fast adsorption and regeneration kinetics, iii) high stability for resistance of sintering and iv) low cost. Calcium-based sorbents have the advantages of the requirements and are derived from natural resources [19, 20].

Another interesting hydrogen production technology is based on chemical looping reforming (CLR) concept. A solid oxygen carrier is included in the system for transferring the oxygen to fuel without directing contact between fuel and air which involve the steam reforming and partial oxidation reactions [21-23]. The selection of oxygen carrier is a significant task as each of oxygen carrier has a different redox system which directly affect process performance. The properties of suitable oxygen

carrier are i) high oxygen transport capacity, ii) high reactivity for reduction and oxidation reaction, iii) high stability and good attrition, iv) low cost and v) environmental friendly [24, 25]. Ni-based oxygen carriers are extensively studied as it exhibits very high reactivity with strong capacity for breaking the C–C bond in ethanol. Moreover, the significant advantage of using Ni-based OC is providing high energy from re-oxidation to counterbalance the endothermic steam reforming reaction [26-28]. Another interesting first row of transition metal oxides like Fe is considered as a good candidate because of its availability, low price, and non-toxicity. In addition, iron oxides possess multifunctional abilities for chemical looping and water splitting (WS) [29-31]. However, when unsupported Fe_2O_3 is used for CLR, its activity degrades rapidly after a few redox cycles, resulting it unsuitable for a long term cyclic operation.

The combination between sorption enhanced steam reforming (SESR) process and chemical looping reforming (CLR) concept becomes the intensified process called sorption enhanced chemical looping steam reforming (SECLR) process. In this process, it contains both of CO_2 adsorbent and oxygen carrier in a fuel reactor where partial oxidation of hydrocarbon by lattice oxygen from oxygen carrier, CO_2 sorption, water gas shift reaction and reforming reactions take place simultaneously for hydrogen production [32-34]. Thus, the sorption enhanced chemical looping steam reforming (SECLR) process is promising to efficient conversion of bioethanol to high purity of hydrogen and has potential to manage heat integration under self-sufficient condition as the re-oxidation of oxygen carrier and sorbent's carbonation in regeneration cycle are exothermic reactions and can provide heat for highly endothermic reaction [35, 36].

The materials (CO_2 sorbent and oxygen carriers) during multicyclic operation is a huge challenge in sorption enhanced chemical looping steam reforming process as it could be effectively regenerated and recycled. Using pure metal oxide in reduction/oxidation cycle reveal poor performance due to agglomeration and sintering [37, 38]. A multifunctional catalyst which combines the Ni or Fe based reforming catalyst and oxygen carrier as well as the calcium carbon dioxide sorbent into one particle is emerged to improve reactivity and recyclability [39, 40]. However, studies on the process simulation and suitable materials in the long-term performance of the oxygen carrier (reactivity and stability) of the complex sorption enhanced chemical looping reforming process from bioethanol for hydrogen production are lacked.

1.2   Objectives

The aim of this research is to design and develop suitable materials for the sorption enhanced chemical looping reforming process (SECLR) for hydrogen production from bioethanol.

1.3   Scope of works

The scope of works is divided into three parts as follows:

Part 1:   Model four processes including conventional ethanol steam reforming (ESR), sorption enhanced steam reforming (SESR), chemical looping reforming (CLR) and sorption enhanced chemical looping reforming process (SECLR) for hydrogen production from ethanol via ASPEN plus program using NiO and CaO as oxygen carrier and CO_2 sorbent, respectively.

Determine effects of important operating and design parameters (such as temperature, pressure, steam to ethanol molar ratio, solid circulation rate and solid split fraction) on their process performance including ethanol conversion, hydrogen purity, hydrogen productivity, CO_2 capacity and energy requirement.

Part 2: Combine Fe_2O_3 (oxygen carrier) and modified CaO with Al_2O_3 (CO_2 sorbent) by different methods including sol-gel, mechanical mixing and impregnation at different Fe contents (5, 10 and 15 wt %) and characterize their properties by several techniques of XRD, N_2 physisorption, SEM-EDX and DSC-TGA.

Test the multifunctional material performance on the sorption enhanced chemical looping reforming process (SECLR) of ethanol in a fixed bed reactor with the stability test in term of sorption capacity in SECLR and oxygen carrier in WS.

Part 3: Prepare the three types of catalysts including Fe-based oxygen carriers, Ni-based oxygen carriers and Fe/Ni-based oxygen carriers derived from Hydrotalcite-like precursors.

Utilize various characterization techniques in order to describe the relationship between catalytic structure and catalytic performance with respect to activity and stability for H_2 production in chemical looping reforming process of ethanol consisting of XRD, ICP-OES, N_2 physisorption, H_2-TPR and TEM techniques for the catalytic structures and properties, TPO, SEM

and Raman analysis for the coke formation and XPS and *in-situ* DRIFTS for the evolution of the catalyst during the experiments.

1.4   Organization of thesis

This dissertation consists of 8 chapters. Chapter I provides the rational, objectives and scope of the research. Chapter II gives the theoretical information of the processes for hydrogen production from the conventional process to the developed processes as well as the feedstock information of bioethanol. Chapter III describes the literature reviews divided into 2 topics of hydrogen production from experiment and simulation works. Chapter IV exhibits the research methodology including the simulation and design for process simulation and material preparation method and characterization used in this study. Chapter V presents the performance comparison of hydrogen production through four reforming processes: conventional ESR, SESR, CLR and SECLR with combustion of a fraction of hydrogen product for heat supply within the system in terms of net hydrogen productivity, hydrogen purity, ethanol conversion, CO_2 capture ability and thermal efficiency on the basis of self-sufficiency. Chapter VI investigates the combination of iron-based oxygen carrier and CaO-based sorbents into multifunctional material. The effects of preparation method and metal contents on phase formation were determined on their activity and stability over multiple cycles of operation. Chapter VII shows the results of hydrogen production from CLR process with high catalytic activity, stability and regenerability of bimetallic NiFe-based oxygen carrier. The conclusions of this study and recommendations are summarized in Chapter VIII.

CHAPTER II

THEORY

In this chapter, we give essential information about bioethanol and theory of hydrogen production involved the process of steam reforming (SR), sorption enhanced steam reforming (SESR), chemical looping reforming (CLR) and sorption enhanced chemical looping reforming (SECLR).

2.1   Bioethanol

Bioethanol is one of bio-fuels which are predominantly derive from biomass. The use of biomass as feedstock is beneficial because it is renewable, environmental-friendly (no net releases of CO_2) and economical for presence and the future. The bioethanol can be produced by several processes and feedstock depending on the landscape. The feedstocks for ethanol production are divided in three types [41]: (i) sucrose which are sugar cane, sugar beet and fruits (ii) starchy materials which are corn, wheat, rice, potatoes and barley (iii) lignocellulosic biomass which are wood, straw and grass. The global ethanol production has been increasing from 75 billion liters in 2007 to 159 billion liters in 2019 as shown in Figure 1.

Figure 2 illustrates the global ethanol fuel production by country. 56% of Global bioethanol was produced in the United States which mainly use starch from coarse grains (corn) as feedstock while 28% was Brazil using sugar cane and other countries were Europe, China and Canada, respectively. The most consumption of ethanol was also found in United States which is the majority of used ethanol for

blending with gasoline and the secondary is in Brazil, consistent with the production

capacity [42, 43].
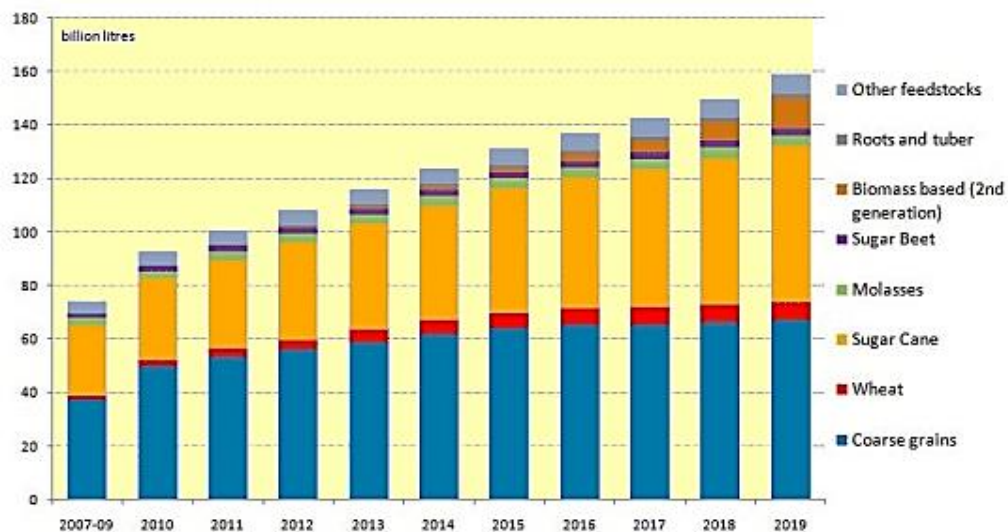
Figure 1 Global Bioethanol Production by feedstock (2007 - 2019)

Source: The Crop site [42]
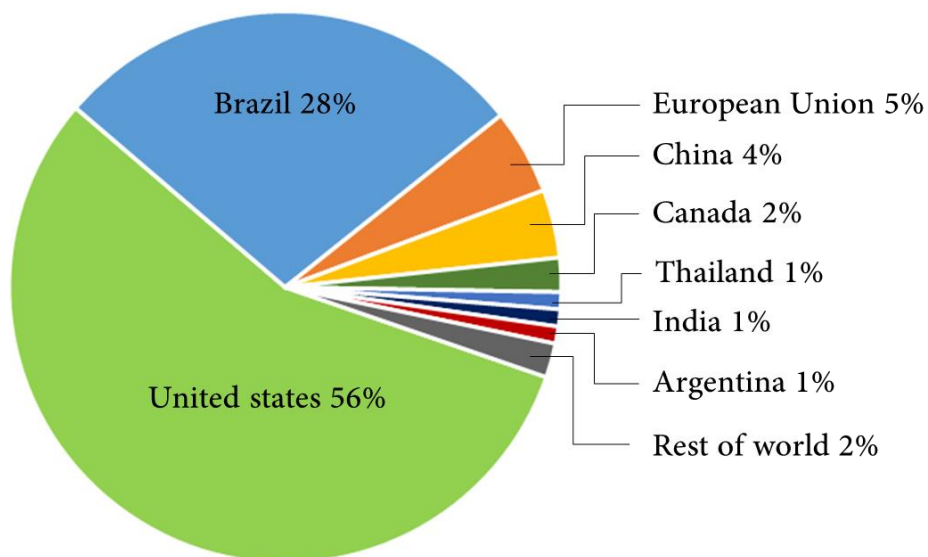
Figure 2 Global Bioethanol Production by country in 2018

Source: RFA analysis of public and private data sources [43]

The processes for bioethanol production from biomass depend on type of feedstock. Table 1 shows pathway to produce bioethanol with different raw materials and Figure 3 shows the flow chart from lignocellulosic biomass materials for the bioethanol production. The production of bioethanol from lignocellulosic material is more difficult than other feedstocks due to natural resistance of biomass. There are four major processes which compose of pretreatment, hydrolysis, fermentation and separation.

Table 1 Bio-ethanol pathways from different raw materials.

Raw material	Processing
Wood	Acid hydrolysis + fermentation
Wood	Enzymatic hydrolysis + fermentation
Straw	Acid hydrolysis + fermentation
Straw	Enzymatic hydrolysis + fermentation
Wheat	Malting + fermentation
Sugar cane	Fermentation
Sugar beet	Fermentation
Corn grain	Fermentation
Corn stalk	Acid hydrolysis + fermentation
Sweet sorghum	Fermentation
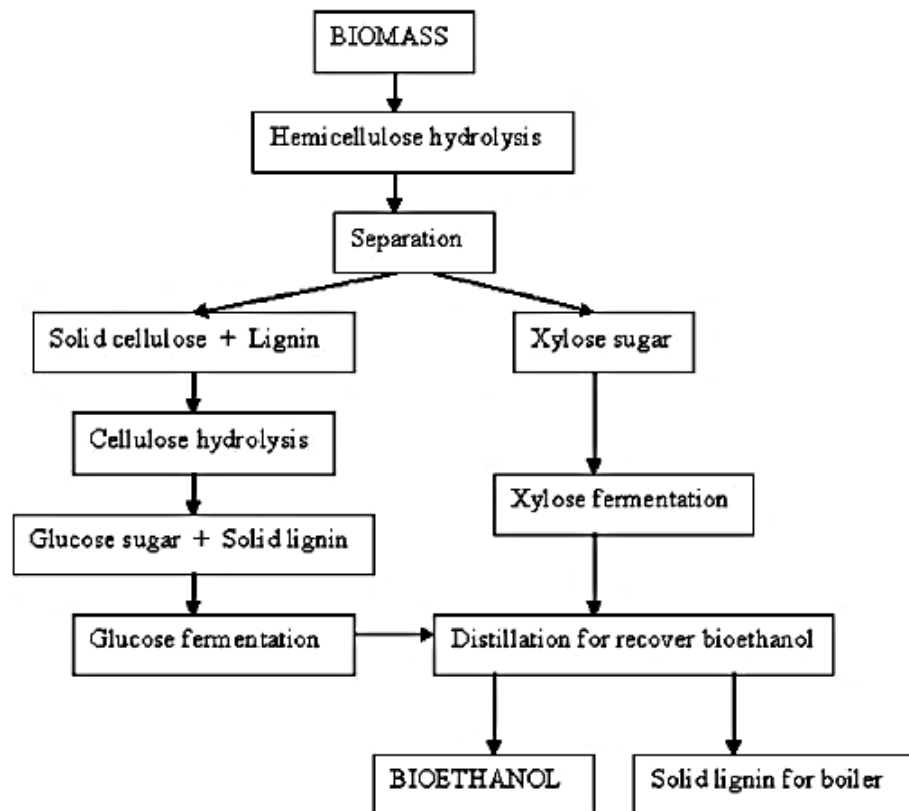
Figure 3 Flow chart for bio-ethanol production from lignocellulosic biomass materials [41]

2.2   Ethanol Steam Reforming (ESR)

Steam reforming is the most widely method for hydrogen production. At present, 95% of hydrogen are produced from natural gas, one of fossil fuel, which mainly compose of methane and the process is via steam methane reforming (SMR). From the concerning of fossil source depletion, bioethanol is an important candidate because it can be derived from biorenewable and environmentally friendly energy source. The ethanol steam reforming (ESR) is a complex process which involves the main reaction (2.1) and many possible side reactions, depending on catalyst and operating condition [44, 45].

Ethanol steam reforming

$$C_2H_5OH + 3H_2O \longrightarrow 2CO_2 + 6H_2 \tag{2.1}$$

Some of the reactions that can occur during hydrogen production are listed below.

Ethanol decomposition

$$C_2H_5OH \longrightarrow CO + CH_4 + H_2 \tag{2.2}$$

Ethanol dehydration

$$C_2H_5OH \longrightarrow C_2H_4 + H_2O \tag{2.3}$$

Ethanol dehydrogenation

$$C_2H_5OH \longrightarrow CH_3CHO + H_2 \tag{2.4}$$

Acetaldehyde decarbonylation

$$CH_3CHO \longrightarrow CH_4 + CO \tag{2.5}$$

Methane steam reforming

$$CH_4 + H_2O \longrightarrow CO_2 + 3H_2 \tag{2.6}$$

Dry reforming of methane

$$CH_4 + CO_2 \longrightarrow 2CO + 2H_2 \tag{2.7}$$

Methanation

$$CO + 3H_2 \longrightarrow CH_4 + H_2O \tag{2.8}$$

$$CO_2 + 4H_2 \longrightarrow CH_4 + 2H_2O \tag{2.9}$$
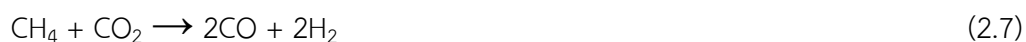
Carbon formation reaction

$$CH_4 \longrightarrow C + 2H_2 \tag{2.10}$$

$$2CO \longrightarrow C + CO_2 \tag{2.11}$$

The conventional ethanol steam reforming consists of three major units: steam reformer, water gas shift reactor, which include high-temperature shift (HTS) and low-temperature shift (LTS), and purification as shown in Figure 4 [46].
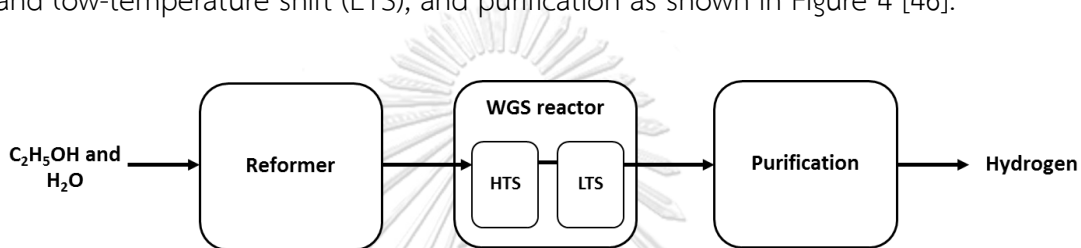
Figure 4 Schematic description of conventional ethanol steam reforming

Typically, in these processes, the ethanol is mixed with water at optimized steam/ethanol ratio and then preheated before feeding to a steam reformer. In the steam reformer, steam reforming reaction takes place for hydrogen production at high temperature (up to 1000°C) because this reaction is endothermic, so it needs external heat to keep constant operating temperature. The mixture is converted to gaseous product in the presence of catalyst. The outlet stream from the steam reformer goes to the water gas shift reactor for increasing hydrogen yield and eliminating poisonous carbon monoxide gas. Finally, the resulting stream is sent to a purification unit to separate hydrogen from the other compounds.

In fact, the steam reforming and water gas shift reaction do not occur separately as it uses the same reactant. Therefore, it is able to combine the steam reformer and water gas shift reactor which is called 'fuel reactor' (FR) as shown in Figure 5.
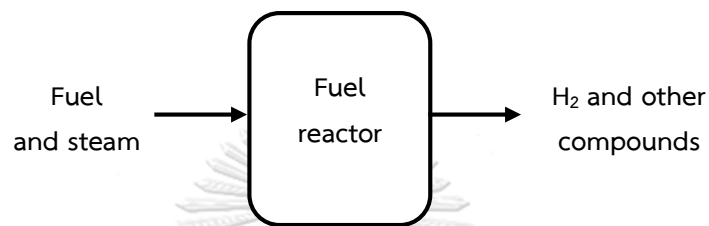
Figure 5 Schematic description of steam reforming

2.3   Sorption Enhanced Steam Reforming (SESR)

Because the conventional steam reforming process occurs with catalyst at high temperature, consists of several steps and releases the carbon dioxide gas into atmosphere, the sorption enhanced steam reforming (SESR) is emerged in this research area for development. The sorption enhanced steam reforming is performed in the presence of CO_2 sorbent, based on Le Chatelier's principle, to shift the reaction forward. This is not only eliminating disadvantages mentioned above, but also increasing hydrogen production rate and hydrogen purity because the equilibrium is shifted forward reaction to product side [47-49].

For the sorption enhanced steam reforming process, calcium oxide (CaO) is the most employed sorbent as it has high CO_2 sorption capacity. For this sorbent,

calcium oxide adsorbs CO_2 gas and after reaction, it forms the calcium carbonate ($CaCO_3$) according to following reaction.

Carbonation reaction of CaO

$$CaO + CO_2 \longrightarrow CaCO_3 \qquad (2.12)$$

In the sorption enhanced steam reforming process, there are two reactors as shown in Figure 6 including the fuel reactor (FR) and calcination reactor (CR). The first reactor is for the hydrogen production and the latter is for the regeneration of saturated CO_2 sorbent at high temperature to release CO_2 via the reverse of reaction (2.12).
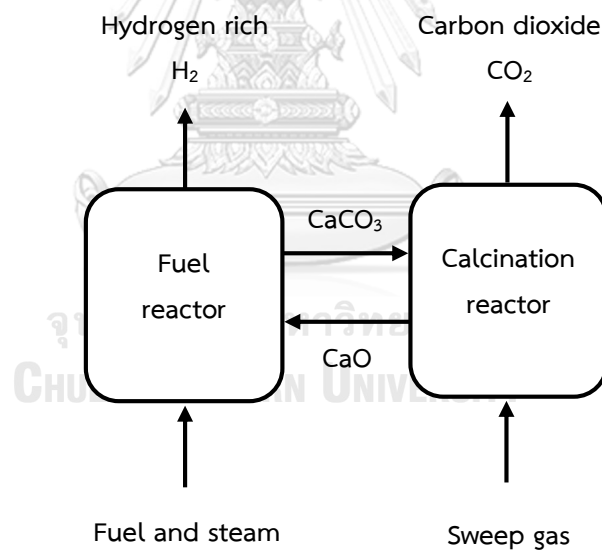
Figure 6 Schematic description of sorption enhanced steam reforming using CaO as CO_2 sorbent

2.4 Chemical Looping Reforming (CLR)

The principle of chemical looping reforming is similar to chemical looping combustion which involves oxidation of a fuel using oxygen from a solid oxygen carrier (OC) instead of oxygen from air; therefore, the direct contact between fuel and air is avoided [50-52]. However, in chemical looping reforming, air to fuel ratio is kept low to prevent fully oxidize of fuel because the desired product in this process is synthesis gas or hydrogen gas which is not heat. Hence, the chemical looping reforming is the process that desires partial oxidation of hydrocarbon fuel using oxygen from solid oxide which excludes cost and power for air separation unit. The process consists of two reactors including fuel reactor (FR) and air reactor (AR) as shown in Figure 7.
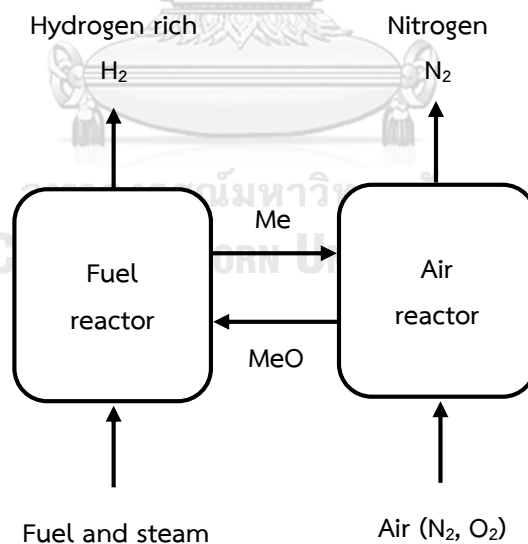
Figure 7 Schematic description of chemical looping reforming (Me = metal, MeO = metal oxide).

In two reactors of chemical looping steam reforming process of ethanol, there are more reactions taking place apart from the ethanol steam reforming (subsection 2.2) including a redox reaction, depending on type of oxygen carrier. For Ni-based oxygen carrier, the reactions are summarized below [53, 54]:

Fuel reactor:

Oxidation

$$C_2H_5OH + 6NiO \longrightarrow 6Ni + 2CO_2 + 3H_2O \tag{2.13}$$

$$CH_4 + 4NiO \longrightarrow 4Ni + CO_2 + 2H_2O \tag{2.14}$$

$$CO + NiO \longrightarrow Ni + CO_2 \tag{2.15}$$

$$H_2 + NiO \longrightarrow Ni + H_2O \tag{2.16}$$

Partial Oxidation

$$C_2H_5OH + NiO \longrightarrow Ni + 2CO + 3H_2 \tag{2.17}$$

$$CH_4 + NiO \longrightarrow Ni + CO + 2H_2 \tag{2.18}$$

Air reactor:

$$Ni + 1/2O_2 \longrightarrow NiO \tag{2.19}$$

For Fe-based oxygen carriers which have lower reactivity for breaking bond compared to Ni, the reactions taking place in fuel reactor and air reactor are listed below [55, 56]:

Fuel reactor:

Partial Oxidation

$$C_2H_5OH + 3Fe_2O_3 \longrightarrow 3H_2 + 2CO + 2Fe_3O_4 \qquad (2.20)$$

$$C_2H_5OH + Fe_2O_3 \longrightarrow 3H_2 + 2CO + 2FeO \qquad (2.21)$$

Reduction of iron oxide

$$3Fe_2O_3 + CO \longleftrightarrow 2Fe_3O_4 + CO_2 \qquad (2.22)$$

$$3Fe_2O_3 + H_2 \longleftrightarrow 2Fe_3O_4 + H_2O \qquad (2.23)$$

$$Fe_3O_4 + CO \longleftrightarrow 3FeO + CO_2 \qquad (2.24)$$

$$Fe_3O_4 + H_2 \longleftrightarrow 3FeO + H_2O \qquad (2.25)$$

$$FeO + CO \longleftrightarrow Fe + CO_2 \qquad (2.26)$$

$$FeO + H_2 \longleftrightarrow Fe + H_2O \qquad (2.27)$$
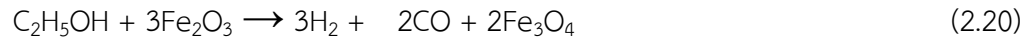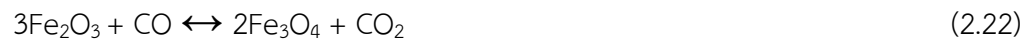
In the fuel reactor, the deep reduction products of iron oxide, FeO and Fe (as seen in Eqs. 2.21, 2.24-2.27) can be re-oxidized by reacting with steam to form Fe_3O_4 and pure H_2 (Eqs. 2.28 and 2.29) which is their advantage compared to other oxygen carriers, and the net reactions can be illustrated in Eq. 2.30 [57, 58]:

Steam oxidation

$$3FeO + H_2O \longleftrightarrow Fe_3O_4 + H_2 \qquad (2.28)$$

$$Fe + H_2O \longleftrightarrow FeO + H_2 \qquad (2.29)$$

Overall

$$3Fe + 4H_2O \longleftrightarrow Fe_3O_4 + 4H_2 \qquad (2.30)$$

Air reactor:

$$2Fe_3O_4 + 1/2O_2 \longleftrightarrow 3Fe_2O_3 \qquad (2.31)$$
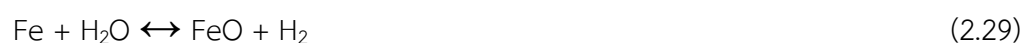
2.5   Sorption Enhanced Chemical Looping Reforming (SECLR)

The sorption enhanced chemical looping reforming (SECLR) process is a combination of sorption enhanced steam reforming (SESR) and chemical looping reforming (CLR) which is considered as upgrading of chemical looping reforming process by capturing CO_2 during hydrogen production with an additional reactor for regeneration CO_2 sorbent. Therefore, in this process, there are three reactors connected including fuel reactor (also called reforming reactor), calcination reactor and air reactor as shown in Figure 8. The reactions that occur in this process are presented in the previous subsection (2.2-2.4) [59, 60].
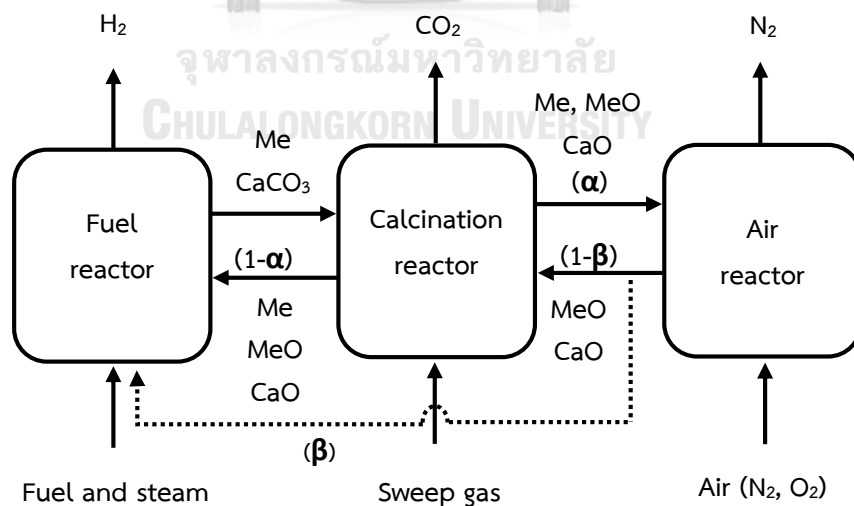
Figure 8 Schematic description of sorption enhanced chemical looping reforming using CaO as CO_2 sorbent (Me = metal, MeO = metal oxide).

To begin with, fuel and steam are fed into fuel reactor where fuel is firstly partially oxidized by solid particle of MeO (metal oxide) which is also fed at the same time to produce H_2 and CO. Then, catalytic steam reforming which is catalyzed by Me (metal) and water gas shift reaction occur. At this time, CaO captures CO_2 simultaneously to produce more H_2 and outlet stream also contains CH_4, CO_2, CO, C_2H_4 and CH_3CHO. After that, both reduced oxygen carrier and $CaCO_3$ are fed to the calcination reactor and the air reactor for regeneration and re-oxidation before coming back to the fuel reactor. The heat from highly exothermic reaction of re-oxidation of oxygen carrier in the air reactor can be provided to the calcination reactor and the reforming reactor leading to the heat balance in the system. Therefore, the sorption enhanced chemical looping reforming (SECLR) process has potential to operate under self-sufficient condition.

CHAPTER III

LITERATURE REVIEWS

As the energy demand continuously increases, research efforts have been focused on alternative fuels including hydrogen. The hydrogen production has been widely studied over the past decade. Hydrogen can be produced by primary energy source like fossil fuel (coal, oil and natural gas) and renewable resources such as wind, solar, tidal and biomass. Both industrially and academically for hydrogen production are used methane and methanol as feed stock in steam reforming process. However, from the energy source concerns, the ethanol steam reforming has drew much attention in the last few years due to its many advantages especially renewabilty from biomass. Currently, the sorption enhanced chemical looping steam reforming (SECLR) which is a combination between sorption enhanced steam reforming (SESR) and chemical looping reforming (CLR) process becomes more attractive for hydrogen production than conventional steam reforming. In this section, the development of method for hydrogen production for both experimental and simulation studies are reviewed.

3.1 A review of hydrogen production based on simulation studies

The simple model of the developed process of sorption enhanced chemical looping reforming was firstly performed by Rydén and Ramos (2012) [61] via ASPEN PLUS program which includes three connected fluidized bed reactors and uses NiO as an oxygen carrier and CaO as a solid CO_2 sorbent. Their schematic description of

the process model is shown in Figure 9 of which the blocks and streams are explained in Tables 2 and 3, respectively.
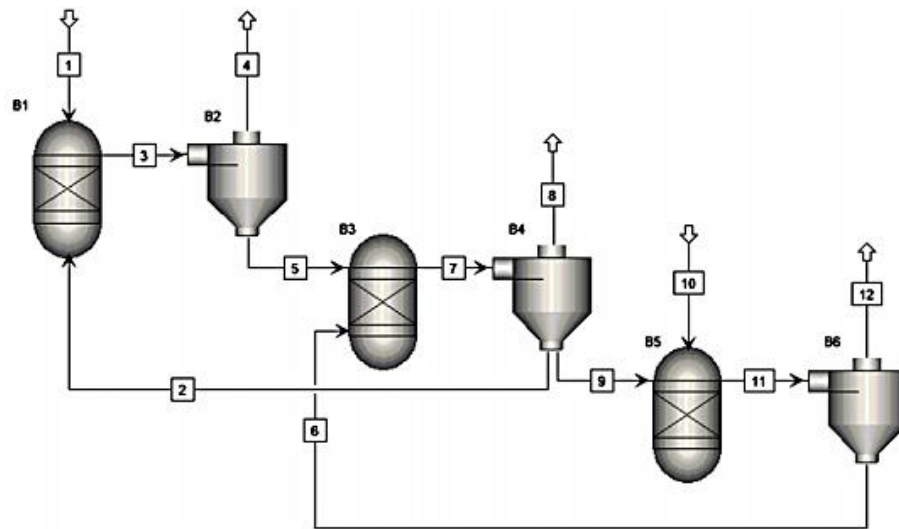
Figure 9 Schematic description of process model from Ryden and Ramos (2012) [61]

Table 2 Summary of block components for the thermodynamic model.

Block	Component
B1	Reformer reactor
B2	Cyclone
B3	Calcination reactor
B4	Cyclone
B5	Air reactor
B6	Cyclone

Table 3 Summary of product streams for the thermodynamic model

Stream	Function
1	Fuel (CH_4, H_2O)
4	Product (H_2, impurities)
8	Carbon dioxide (CO_2)
10	Air (O_2, N_2)
12	Oxygen depleted air (N_2)
2,3,5,6,7,9,11	Establish connections between blocks

The important part of sorption enhanced chemical looping reforming process is the reforming reactor which converts hydrocarbon to hydrogen. The results showed that at reformer temperature of 580 °C and pressure of 1 bar, the hydrogen purity is 98.7 vol% with CH_4 conversion 84.7% and CO_2 capacity 95%. Udomchoke et al. (2016) [62] also studied hydrogen production in the sorption enhanced chemical looping reforming process from biomass by simulating the model in ASPEN PLUS program. They further designed the process model taken from Rydén et al. [61] with modification of catalyst and sorbent regeneration which is represented in β shown in Figure 10.
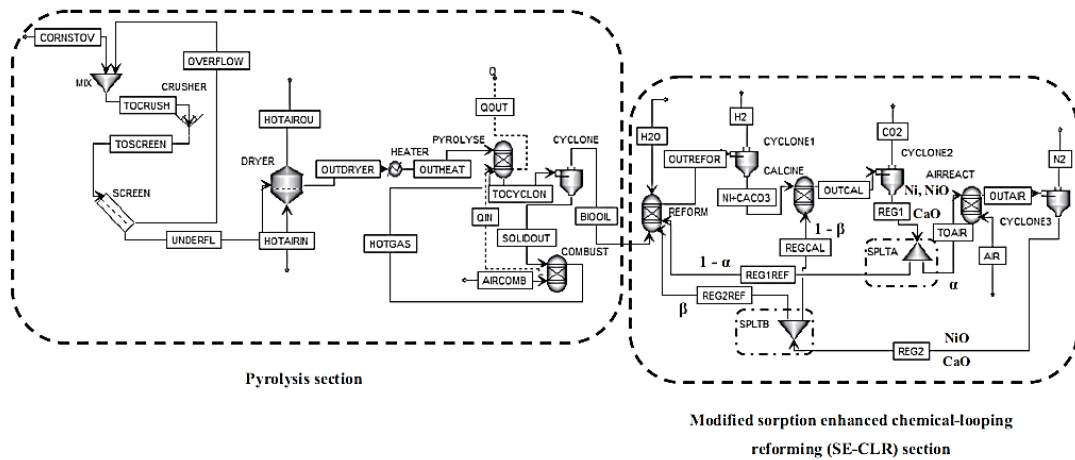
Figure 10 Process flow diagram of modified sorption enhance chemical-looping reforming from Udomchoke et al. (2016) [62]

For the hydrogen production section, the results showed that modified sorption enhanced chemical-looping reforming (SECLR) process can improve both hydrogen yield and purity. Moreover, they reported that the amount of solid circulation in the modified SE-CLR process is less than in the un-modified SECLR process at optimal conditions which imply that the modified SECLR process requires less energy than un-modified. Phuluanglue (2017) [63] also simulated the SECLR process focusing on the intensified SECLR process fed by methane. Their intensified process of sorption enhanced chemical-looping reforming (SECLR) for hydrogen production is to recycle a portion of solid NiO and CaO from air reactor (AR) to reforming reactor (RR) and to employ the outlet CO_2 as sweep gas at the calcination reactor (CR) under energy self-sufficient operation. The process flow diagram is shown as follow.
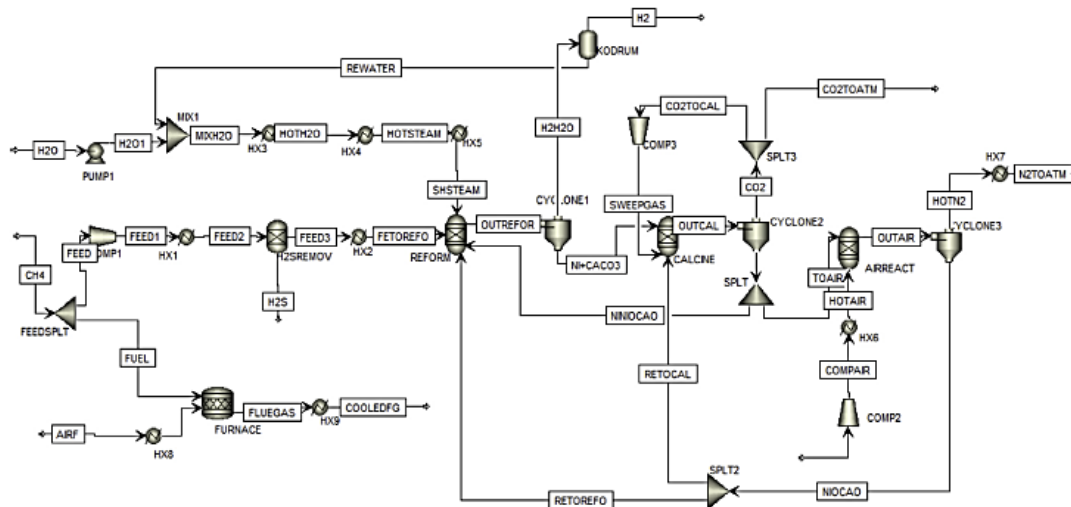
Figure 11 Process flow diagram of intensified sorption enhance chemical-looping reforming from Phuluanglue et al. (2017) [63]

The results indicated that the intensified SECLR under adiabatic operation with solid ratio from CR to AR of 0.945 and solid ratio from AR to RR of 0.008 showed the best performance with hydrogen productivity of 3.95 kmol/h, CH_4 conversion of 98% and H_2 purity of 98.37% at reformer's temperature 610°C and steam to carbon ratio equal to 4. Yahom et al. (2014) [64] simulated two chemical looping processes: one process being a conventional CLR process and the other being a sorption enhanced process. They found that at temperature of 800°C, a H_2O/CH_4 ratio of 3 and a NiO/CH_4 ratio of 1, the conventional CLR process yielded 2.5 mol of H_2 per mole of CH_4 and hydrogen purity of 75%. However, the process with CO_2 sorption obtained a hydrogen purity more than 90% and a yield within the range of 3 mol of H_2 per mole of CH_4. They also studied energy balance and carbon activity of both processes and the data revealed that with increasing steam and temperature, the energy balance becomes more positive approaching a limit value of zero and the activity of carbon formed decreases when using the steam to carbon ratio more than

1 of CLR process and for SECLR process, the thermodynamic is unfavorable to drive the formation of carbon under the studied conditions. Another design of schematic diagram of sorption enhanced chemical looping reforming process from methane is conducted by Antzara and co-worker (2015) [65] They studied a detailed thermodynamic analysis by sensitivity effect of different parameters using CaO and NiO as CO_2 sorbent and oxygen transfer material, respectively. The results of thermodynamic analysis indicate that the sorption enhanced processes have significant advantages compared to the conventional steam reforming as the presence of CaO sorbent in the reformer leads to higher methane conversion, hydrogen purity and yield at low temperatures (650°C). However, the chemical looping reforming concept is remarkable in minimizing thermal requirements of the process. The simulation flow diagram of sorption enhanced chemical looping steam
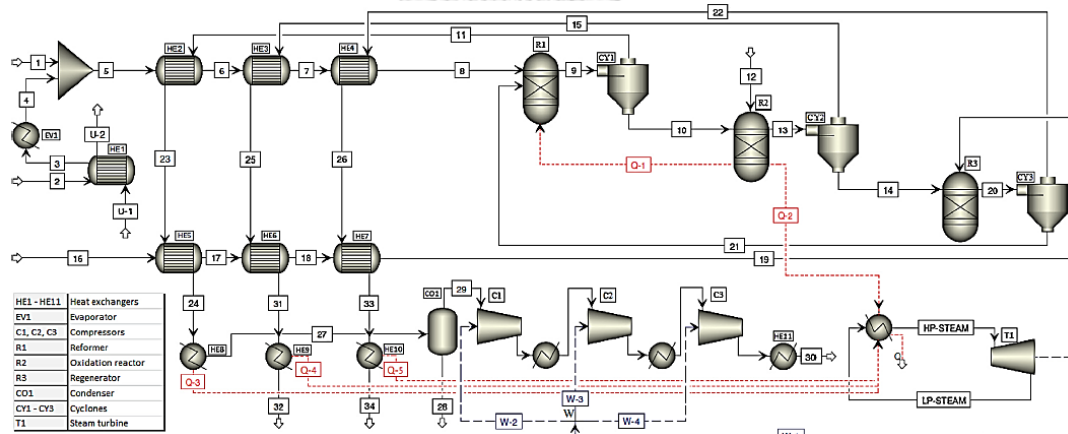
methane reforming is presented in Figure 12.

Figure 12 Process flow diagram of sorption enhance chemical-looping steam methane reforming from Antzara et al. (2015) [65]

3.2   A review of hydrogen production based on experiments

According to literatures, the chemical looping concept was first proposed by Lyon and Cole (2000) [66] in term of 'Unmixed combustion' which alternate between fuel and air passed through the oxygen transfer materials (OTM) in a single reactor. The oxidation reaction occurs over the oxygen transfer materials by fuel and is used to provide heat to endothermic reaction like steam reforming process. The reduced oxygen transfer material is regenerated via re-oxidation by air. In their experiment, they obtained high purity of hydrogen in the presence of CaO and also found that the process has self-sufficient operation without external heat output. The selection of oxygen transfer material or oxygen carriers (OCs) was carefully considered to employ in the system as it affects performance of hydrogen production. Kang et al. (2010) [67] demonstrated candidate OCs and support for chemical looping process. They selected based on several criteria of their physical and chemical properties such as melting point. Table 4 shows the melting temperatures of the candidate OCs and attributed to Ni, Co, Cr, Ce, W, Fe, Mn and their oxides that have desired melting point (>1400°C) of OCs.

Table 4 Melting temperatures of the candidate oxygen carriers and their metals

Metal Oxides and metals	Melting point (°C)
Ni/NiO	1455/1955
$Cu/Cu_2O/CuO$	1085/1235/1446
$Fe/FeO/Fe_{0.947}O/Fe_3O_4/Fe_2O_3$	1538/1377/1378/1597/1565
Cd/CdO	321/-
$Mn/MnO/Mn_3O_4/Mn_2O_3$	1246/1842/1562/1347
$Co/CoO/Co_3O_4$	1495/1830/-
$Sn/SnO/SnO_2$	232/1042/1630
$Ge/GeO/GeO_2$	938/-/1116
Zn/ZnO	420/1975
$Ce_2O_3/CeO_{1.72}/CeO_{1.83}/CeO_2$	2230/-/-/2400
$W/WO2/WO_{2.722}/WO_{2.96}/WO_3$	3407/1724/-/-/1472
$Mo/MoO_2/MoO_{2.75}/MoO_{2.889}/MoO_3$	2623/1927/1920/1512
$Nb/NbO/NbO_2/Nb_2O_5$	2477/1937/1902/1512
$Cr/CrO_2/Cr_2O_3$	1907/-/2330
$V/VO/VO_{1.24}/VO_2/V_2O_3/V_2O_5$	1910/1790/-/1545/2067/670
In/In_2O_3	156/1913
Ta/Ta_2O_5	3014/1785

In chemical looping reforming (CLR), OCs should not only have high melting temperatures but also perform some characteristics [68, 69]: (i) sufficient oxygen transport capacity (ii) high reactivity for reduction and oxidation reaction (iii) steam reforming and WGS reactivity to H_2 production (iv) physical strength (v) environmental

friendliness and low-cost. The heat capacity is one of important physical properties and has a relationship in term of thermal balance. The values of specific heat capacity of some substances are shown in Table 5.

Table 5 Specific heat capacity of some substance

Substance	Specific heat capacity (J/g °C)
Manganese	0.46
Iron	0.449
Nickel	0.44
Cobalt	0.435
Copper	0.385

Ni-based oxygen carriers are extensively studied both of experimental and simulation works. It shows very high reactivity and good stability at high temperature. García-Labiano et al. (2015) [70] presented the experimental results obtained in a continuously operating CLR unit (1 kWth) and used $NiO_{21}/\gamma Al_2O_3$ as oxygen carrier. The results showed that syngas composing of ≈61 vol. % H_2, ≈32 vol. % CO, ≈5 vol. % CO_2 and ≈2 vol. % CH_4 was obtained at auto-thermal conditions. They also studied effects of the main operating conditions such as oxygen-to-fuel molar ratio, temperature (850-950 $^\circ$C), and H_2O/EtOH molar ratio. They found that temperature in fuel reactor hardly affected the gas composition and increasing the amount of water injected slight increased concentration of H_2 and CO because the water enhancement of the steam reforming reactions catalyzed by Ni. Finally, they claimed the oxygen-to-fuel molar ratio is the main parameter in CLR process. Zafar et al.

(2005), Ryden et al. (2008) and Wang et al. (2016) investigated effect of support on hydrogen production over Ni based oxygen carrier. Zafar et al. [71] reported that the Fe, Mn, Ni and Cu-based oxygen carriers supported on $MgAl_2O_4$ showed higher reactivities than supported on SiO_2 oxygen carriers at high temperature. Ryden et al. [38] found that NiO on $MgAl_2O_4$ and αAl_2O_3 seems to have more stable on physical and chemical structure than on γAl_2O_3 which changes considerably during operation. Wang et al. [72] studied a group of Ni-based OCs with different support structure, including Ni/Al_2O_3, Ni/MMT, Ni/Al-MCM-41 and Ni/SBA-15 and showed that Ni/SBA-15 OCs with mesoporous structure exhibited most efficient confinement effect to accomplish small nickel particles and high dispersion which follow by Ni/Al-MCM-41, Ni/MMT and Ni/Al_2O_3, respectively.

Another interesting oxygen carrier which has high melting point and required properties is Fe-based material. Fe-based oxygen carrier offered low-cost and environmental-friendly more than Ni-based one. Although, oxygen carrier from Fe-based has low oxygen transport capacity, it is considered as an attractive characteristic in different oxidation state as Fe_2O_3 is reduced (FeO, Fe_3O_4 or Fe). Because of this reason, the researcher made an effort to utilize for hydrogen production. Wei et al. (2014) [73] evaluated the reactivity of Fe_2O_3/Al_2O_3 prepared by mechanical mixing method with a mass ratio of Fe_2O_3 to Al_2O_3 of 7/3 in CLR of methane process to produce H_2 at 850 °C. The authors found that H_2 productivity of 75% was obtained at the beginning of the reaction and declined dramatically after 15 minutes due to material sintering. Hafizi et al. (2015) [74] synthesized 15 wt% Fe_2O_3 oxygen carrier on alumina (Al_2O_3) support using different synthesis methods, including impregnation and co-precipitation, and tested for CLR of methane process.

Synthesis method significantly affected the carrier's performance. The Fe on alumina synthesized by impregnation method showed higher performance (79% H_2 yield) than the carrier synthesized by co-precipitation method (65% H_2 yield) at reforming temperature of 600 °C. The reduction of the oxygen carrier's performance was observed during operation due to the formation of $FeAl_2O_4$ spinel in Fe_2O_3/Al_2O_3 structure. Forutan and co-workers (2015) [75] studied performance of alumina supported Fe-based oxygen carriers compared to Mn, Co and Cu oxygen carriers for 4 cycles of oxidation and reduction in CLR process of methane. Four different OCs were synthesized by co-precipitation method containing 40 wt% of metal content. According to the experiments, the maximum H_2 purity was obtained about 72% at 850 °C for Fe_2O_3 oxygen carrier, while Mn-, Co- and Cu-based oxygen carrier provided 50, 54 and 68% of H_2 purity, respectively. Nevertheless, H_2 production was found to reduce over multiple cycles due to sintering effect. Yüzbasi et al. (2017) [76] prepared Fe_2O_3/Al_2O_3 oxygen carrier using a sol-gel technique with 80 wt% of iron content, in order to investigate the influence of the iron precursors (iron nitrate, iron chloride and iron acetylacetonate) on their activity for H_2 production via chemical looping. Using iron nitrate and iron acetylacetonate as the iron precursors resulted in materials with a high H_2 yield. While over 50% of H_2 yield was reduced in Fe_2O_3 synthesized from iron chloride precursor due to the presence of $FeAl_2O_4$ in freshly calcined material. The recently experimental demonstration of the combined iron oxide (Fe_2O_3) and alumina (Al_2O_3) with CaO sorbent was reported by Hafizi et al. (2016) [77] for H_2 production in SECLR process of methane and compared to CLR process. 22wt% of iron loaded on alumina was firstly synthesized via impregnation and method and combined with CaO using mechanical mixing. A H_2/CO molar ratio

of 36 in SECLR at 600 °C was obtained which is higher than a H_2/CO molar ratio of 12 in CLR. This is due to the removal of CO_2 by CaO, resulting in an improvement of H_2 production. However, lower H_2 yield in SECLR (75%) was observed compared to CLR (80%) because of the mass transfer resistance in the mixture of oxygen carrier-sorbent material in the reaction media.

As seen, although using Fe_2O_3 can offer high H_2 production due to its high oxygen content; however, its rapid deactivation during reduction/oxidation cycles and mass transfer resistance of the combined material are major drawbacks of the chemical looping process. Several strategies have been proposed to develop an iron-based oxygen carrier such as addition of secondary metals or alloying to enhance catalytic activity and stability, using basic support or doping with alkaline metal to minimize coke formation as well as preparation method. The alloying Fe with other metals such as Ce, Co and Ni has been widely investigated. Among of them, the Ni-Fe alloy has attracted particularly attention for reforming reactions of various hydrocarbons with steam or CO_2 due to theirs synergistic effects and Ni is a well-known metal site for its ability to rupture C-C bond in ESR reaction. The selection of support material is also an important issue. Currently, the promising support for the chemical looping process of Fe and/or Ni metals are Al_2O_3, MgO and $MgO-Al_2O_3$ [78, 79]. In order to improve the long-term performance (such as stability and regenerability), the use of calcined hydrotalcite-like catalysts has been found to obtain multimetallic mixed oxides which exhibit superior catalytic performance, provide good dispersion of the different components and gain strength for enhancing both hydrogen yields and catalyst stability. Wei et al. (2019) [80] synthesized Fe/Ni/Al oxygen carriers derived from layered double hydroxide (LDH) precursors to employ in

CLR process of biomass coupling with chemical looping hydrogen (CLH). They observed the maximum hydrogen purity ca. 90% at 900 $^{\circ}$C. In CLH stage, the highest hydrogen yield of 470.3 ml/g was obtained in a sample with Fe/Ni ratio of 4/1 which was higher than the sample consisting only Fe/Al oxides. Although Ni does not participate in water splitting reaction, it can supply catalytic active centers to promote the reaction of Fe and H_2O. Moreover, after the reaction, the agglomeration phenomena were occurred but the porous structure still reserved indicating that mixed metal oxygen carrier from LDH precursor is stable and suitable for CLR and CLH process.

As the CO_2 adsorbent (calcium oxide) deactivates when operating at high temperature, researchers have attempted to improve stability and activity. Lu et al. (2006, 2009) [81, 82] investigated performance of CaO by carbonation experiments at 600 °C under a CO_2 partial pressure of 0.3 bar using various precursors, including $Ca(NO_3)_2 \cdot 4H_2O$, $Ca(OH)_2$, $CaCO_3$, $Ca(CH_3COO)_2 \cdot H_2O$ and CaO. The adsorbent prepared from calcium acetate ($CaAc_2$-CaO) had the best performance for CO_2 adsorption with high BET surface area (20.2 m^2/g) and large pore volume (0.23 cm^3/g). For doping $CaAc_2$-CaO with SiO_2, the results had no better performance as the deactivation by sintering is not dominant. Then, they additionally studied refractory dopants with series of nanosorbents based on doped CaO (M/Ca which M = Si, Ti, Cr, Co, Zr, and Ce). The results showed that doped-CaO develop sorbent with better mechanical strength and Zr-doped indicated very high CO_2 capacity performance under multicyclic carbonation-decarbonation testing. The incorporation of inert support materials is immerged as an efficient technique for enhancing the stability of CaO-based sorbents, including aluminum oxide (Al_2O_3), magnesium oxide (MgO), zirconium

oxide (ZrO_2), titanium oxide (TiO_2), silica (SiO_2), yttrium oxide (Y_2O_3), etc [83-85]. Among them, the most investigated one is aluminum-containing material. Zhou et al. (2012) [86] synthesized CaO-based CO_2 sorbents derived from various calcium and aluminum precursors. The as-prepared sorbents consisted of active CaO and inert support materials of Al_2O_3, $Ca_{12}Al_{14}O_{33}$ or $Ca_9Al_6O_{18}$. The result found that the prepared CaO-based sorbents showed much higher CO_2 capture capability and stability over multiple carbonation/calcination cycles compared to pure CaO, which was attributed to the relatively high specific surface area of the sorbents, with better textural properties of pore size and volume, and the inert support material that can effectively prevent or delay sintering of CaO particles. Therefore, CaO-based sorbents has been identified as a suitable material for high-temperature CO_2 adsorption applications in sorption enhanced process. There are several experiments on Ni based and Fe based oxygen carrier with most of using modified CaO as CO_2 adsorbent for H_2 production which are summarized in Table 6.

Table 6 Summaries Ni based and Fe based material tested for hydrogen production in experiment

Process	Materials	Preparation method	Reactant	Material used (g)	Condition			H₂ selectivity (%)	Ref.
					Steam/Fuel ratio	Temp. (°C)			
ESR	10 wt%Ni/γ-Al₂O₃	impregnation	C₂H₅OH	0.1	3	500		90	[87]
	6 wt%Ni/Al₂O₃	sol-gel		0.5	6	400		71.7	[88]
	5 wt%Ni- 5 wt%Ca/Al₂O₃	impregnation	C₂H₅OH	0.15	3	650		57	[89]
	100 wt%Fe₂O₃	commercial oxide		11.3	3	500		60	[13]
	75 wt%Ni-Fe	coprecipitation		0.5	6	500		80	[90]
SESR	15 wt%Ni/CaO-Ca₉Al₆O₁₄	sol-gel	CH₄	4	2	650		87	[91]
	12.5 wt%Ni/CaO-Ca₁₂Al₁₄O₃₃	wet mixing	Biogas	2	3	600		90	[92]
	6 wt%Ni/CaO-Ca₁₂Al₁₄O₃₃	sol-mixing	C₂H₅OH	2	4	600		87	[93]
	5.9 wt%Ni/MgAl	impregnation		20	10	412		60	[47]
	10 wt%NiO/Al₂O₃	coprecipitation	C₂H₅OH	2	3	650		60	[94]
CLR	40 wt%NiO/Al₂O₃	wet impregnation	CH₄	2	3	650		80.5	[95]
	15 wt%Fe₂O₃/Al₂O₃	wet impregnation		2	1.5	825		65	[74]
	15 wt%Fe₂O₃-5 wt%Ca/Al2O3	co-impregnation		2	1.5	550		66	[96]
SECLR	29 wt%NiO/Al₂O₃ + CaO	mechanical mixing	C₂H₅OH	0.5	3	600		90%	[60]
	23 wt%Fe₂O₃/Al₂O₃ + CaO	impregnation	CH₄	2 g OC + 6 g sorbent	1.5	600		75%	[77]

CHAPTER IV

RESEARCH METHODOLOGY

This research is divided into two main sections; simulation and experimental sections. It is started with various processes designs of hydrogen production from bioethanol simulated using Aspen Plus program to select an appropriate technology and to determine optimal operating conditions. The data from simulation section is employed for further experimental study. The appropriate technology is applied to produce hydrogen with modification of materials in laboratory.

4.1   Simulation and design

4.1.1 Process simulation and description

Four processes for ethanol-derived hydrogen production: conventional ethanol steam reforming (ESR), sorption enhanced steam reforming (SESR), chemical looping reforming (CLR) and sorption enhanced chemical looping reforming (SECLR) were simulated in ASPEN Plus V9.0. All sorption enhanced processes (SESR and SECLR) use CaO as the CO_2 sorbent and all chemical looping processes (CLR and SECLR) use NiO as the oxygen carrier. For all processes, some of the produced hydrogen is diverted into combustion sections to generate heat for the processes. The selection of hydrogen as a fuel to burn instead of using ethanol enables possibility for complete carbon capture. The details of each process are described below.

1)   Conventional ESR

The simulation flow diagram of the conventional ESR is shown in Figure 13. Ethanol feed (ETOH) is preheated to a reforming temperature and then fed into a reformer (REFORMER) with steam (SHSTEAM) at a desirable steam to ethanol (S/E) ratio. The overall reaction of ESR for H_2 generation is shown in Eq. 2.1. However, the reaction may occur through various reaction pathways depending on operating conditions and catalyst. Ethanol may be consumed in side reactions: decomposition (Eq. 2.2), dehydration (Eq. 2.3) and dehydrogenation (Eq. 2.4). Methane formed as an intermediate can react with steam or carbon dioxide to form H_2 in Eqs. 2.6 and 2.7, respectively. Methanation reaction can also take place from other intermediates such as carbon monoxide (Eq. 2.8) and carbon dioxide (Eq. 2.9). Hydrogen may still be produced from carbon monoxide through the water gas shift reaction (Eq. 1.3). Lastly, carbon deposit may be generated from methane (Eq. 2.10) and carbon monoxide (Eq. 2.11).

The outlet from the reformer (OUTREFOR) is connected to the water gas shift reactors, which are composed of a high-temperature shift (HTS) reactor and a low-temperature shift (LTS) reactor, to convert undesired CO into hydrogen and improve hydrogen yield and purity. The HTS reactor normally operates at 350-450 °C for fast kinetics, while the LTS does at a more thermodynamically favorable temperature of 200-250 °C [97]. Therefore, the HTS and LTS in this work are operated at 400 and 200 °C, respectively, and at atmospheric pressure to lower CO partial pressure. The product stream from the LTS (OUTLTS) is then cooled and condensed to produce purified H_2 (H2PROD), which is split into two streams: one for net hydrogen production (H2NET) and the other (H2USED) for combustion in a furnace (FURNACE) with air (AIR2).
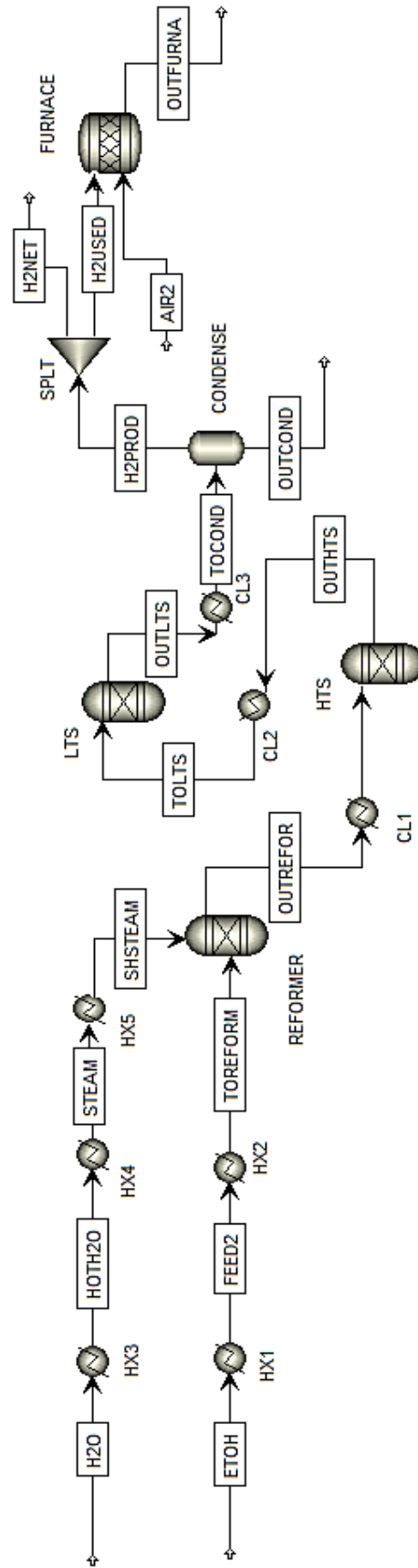
Figure 13 Process flow diagram of conventional ethanol steam reforming (ESR)

2)   SESR

Figure 14 shows the simulation flow diagram for the sorption enhanced steam reforming (SESR). Solid sorbent (CaO) is employed in the reformer to capture CO_2 through the carbonation reaction (Eq. 2.12), shifting forward the equilibrium of steam reforming and water gas shift reactions and increasing H_2 yield and purity. Moreover, the heat released from carbonation could satisfy the heat requirement of the endothermic steam reforming reaction. The exit stream from the reformer (OUTREFOR) containing gaseous products and saturated sorbent as $CaCO_3$ is fed to a cyclone (CYCLONE1) for gas/solid separation. The solid stream (TOCAL) enters the calcination reactor for regeneration to CaO through the reverse reaction of Eq. 2.12. CaO is fed back (RETOREFO) to the reformer with a solid split fraction of 0.9. The gaseous stream (H2H2O) is sent for water removal in SEP. The hydrogen produced (H2PROD) is split to for net hydrogen production and combustion in the same manner as ESR's.

Figure 14 Process flow diagram of sorption enhanced steam reforming (SESR)

3)   CLR

Figure 15 shows the simulation flow diagram of the chemical looping steam reforming in this work. The oxygen carrier in the reformer is reduced by fuel via partial oxidation and oxidation reactions in the reformer. The outlet stream containing reduced oxygen carrier is sent to a cyclone (CYCLONE1). The separated solid stream (TOAIR) is sent for re-oxidation in an air reactor followed by separation in a cyclone, from which the outlet stream composing of NiO (OUTCY2) is split: 90% to the reformer (RETOREFO) and 10% to back to the air reactor. Water is removed from the gaseous stream from the first cyclone (H2H2O). The dry hydrogen stream (H2PROD) is split for combustion and net hydrogen production (H2NET).
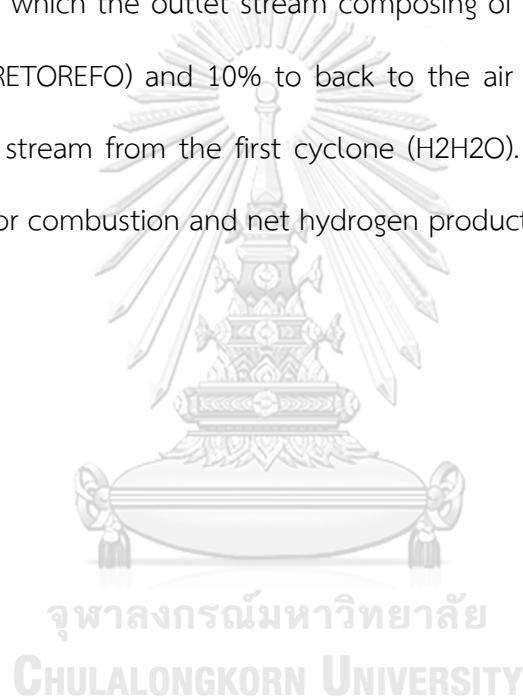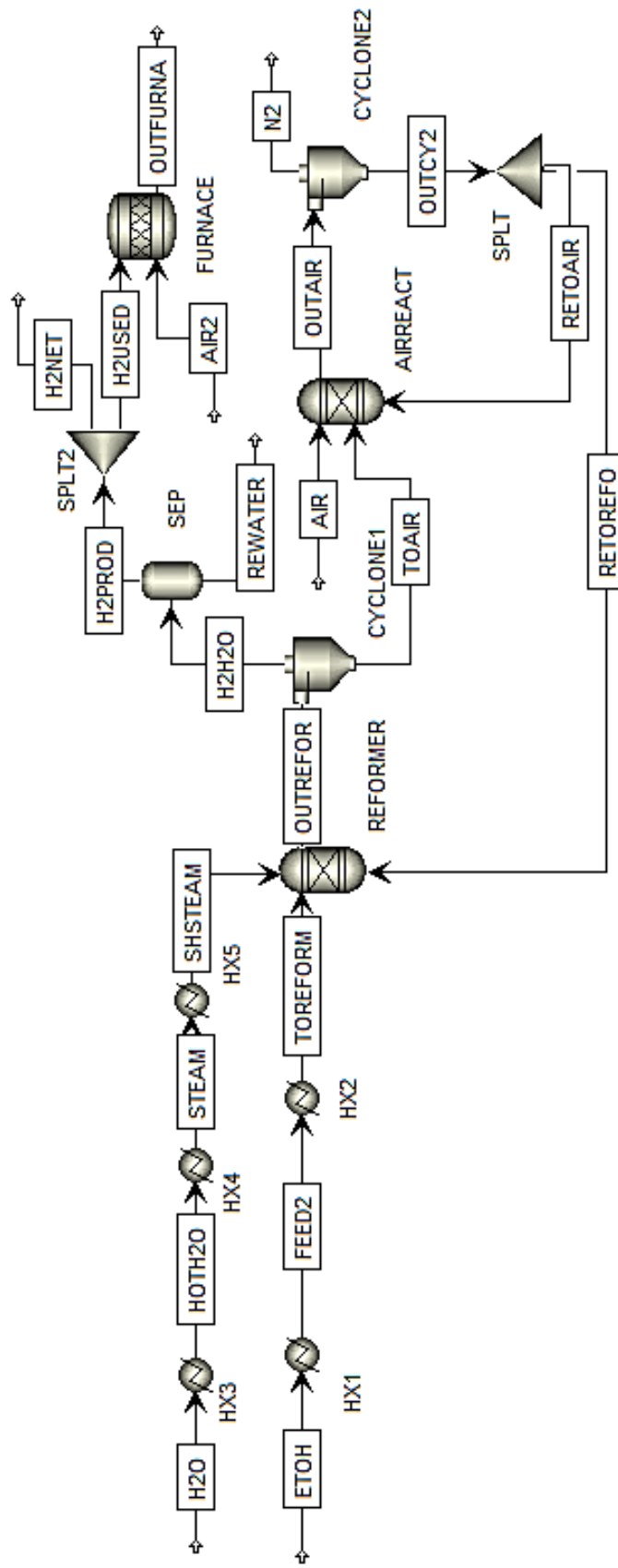
Figure 15 Process flow diagram of chemical looping reforming (CLR)

4)   SECLR

Figure 16 shows the sorption enhanced chemical looping reforming (SECLR) process. The reformer in this process contains both CO_2 adsorbent and oxygen carrier to conduct simultaneously CO_2 adsorption and partial/complete oxidation reactions. The product stream from the reforming reactor (OUTREFOR) is sent to a cyclone for gas-solid separation. The separated solid stream (NICACO3) is firstly fed to a calcination reactor to desorb CO_2 from $CaCO_3$. The effluent stream (OUTCAL) from this calcination reactor is separated into a solid stream and a gas stream in a cyclone (CYCLONE2). Then, CYCLONE2's outlet solid stream (OUTCY2) is split into two parts: one sent back to the reformer (NINIOCAO) and the other passed to an air reactor (TOAIR) to regenerate the oxygen carrier with air (HOTAIR). Due to the highly exothermic re-oxidation of the oxygen carrier, the temperature of the air reactor's product stream rises sharply. This stream is sent back to the calcination reactor (RETOCAL) and reformer (RETOREFO) to provide energy for the reforming reactions as proposed by Udomchoke et al. [62].

Figure 16 Process flow diagram of sorption enhanced chemical looping reforming (SECLR)

4.1.2   Simulation and performance evaluation

Basic equilibrium calculations were carried out in ASPEN Plus V9.0. SRK method was specified for the ESR process, and SOLIDS model with the default vapor model SIG replaced by ESSRK, which is also the default vapor model of the method SRK, was specified for the SESR, CLR and SECLR due to the presence of solid in the systems. RGIBBs units, whose calculations are based on minimizing the Gibbs free energy, were selected as reactor models and CYCLONE units were used for fluid/solid separation. The simulation was performed with the assumptions that (i) the production of components other than C_2H_5OH, H_2O, H_2, CO_2, CO, CH_4, C_2H_4, CH_3CHO, N_2 and O_2 does not occur, (ii) carbon deposition is negligible and (iii) the condition of inlet stream (ETOH and H2O) is at ambient temperature and pressure. The optimal operating conditions were determined by varying parameters in Table 7 until achieving the most effective value. Moreover, the effects of solid circulation, amount of energy requirement and hydrogen yield after the split to combustion were evaluated individually.

Table 7 Ranges of investigated parameters

Temperature	S/E	MeO/E*	α and β**
400, 500, 600 and 700 ℃	1-10	1, 5 and 10	0-1

*Metal, Me = Ca or Ni

**α and β are solid circulation; α is the solids flowing from calcination to air reactor and β is the solids recovered from air reactor to reformer.

***Other conditions are an atmospheric pressure, ethanol feed flow rate of 1 kmol/h, calcination and air reactor's temperature of 900℃.

Hydrogen productivity, ethanol conversion, hydrogen purity and CO_2 capture ability were calculated by the following equations.

$$\text{Hydrogen productivity (kmol/kmol)} = \frac{\dot{n}_{H_2 \text{ produced}}}{\dot{n}_{EtOH \text{ feed}}} \tag{4.1}$$

$$\text{Ethanol conversion (\%)} = \frac{(\dot{n}_{EtOH \text{ feed}} - \dot{n}_{EtOH \text{ out}})}{\dot{n}_{EtOH \text{ feed}}} \times 100 \tag{4.2}$$

$$\text{Hydrogen purity (\%)} = \frac{\dot{n}_{H_2 \text{ produced}}}{\dot{n}_{\text{gaseous product}}} \times 100 \tag{4.3}$$

CO_2 capture ability (%)

$$= \frac{2 \times \dot{n}_{EtOH \text{ feed}} - \dot{n}_{CH_4 \text{out}} - n_{CO \text{ out}} - \dot{n}_{CO_2 \text{out}} - 2 \times (\dot{n}_{EtOH \text{ out}} + \dot{n}_{C_2H_4 \text{out}} + \dot{n}_{CH_3CHO \text{ out}})}{2 \times \dot{n}_{EtOH \text{ feed}}} \times 100 \tag{4.4}$$

Another important parameter for the evaluation of process performance is the thermal efficiency (η), which is defined as energy output divided by energy input [98]. Combustion of hydrogen is also subtracted from the energy output. The schematic energy diagram is shown in Figure 17 and the definition of the thermal efficiency is in the following equation.

$$\text{Thermal efficiency, } \eta \text{ (\%)} = \frac{\dot{n}_{\text{Net } H_2} \times LHV_{H_2}(MJ/mol)}{\dot{n}_{EtOH} \times LHV_{EtOH}(MJ/mol)} \tag{4.5}$$

where $\dot{n}_i$ is the mole flow rate of species i, LHV_i is the lower heating value of species i.
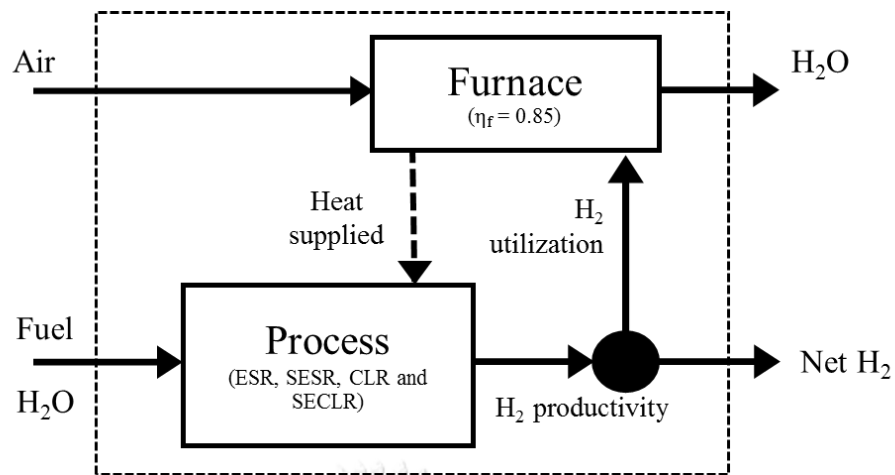
Figure 17 Schematic energy diagram of hydrogen production process with heat supplied by burning some of product stream

A significant process performance indicator in this work is the net hydrogen, which is the amount of hydrogen utilization for combustion subtracted from the amount of hydrogen productivity:

Net hydrogen (kmol/kmol) = Hydrogen productivity – Hydrogen utilization (4.6)

The amount of hydrogen utilization is the amount of hydrogen diverted for combustion with air to fulfill exactly the thermal requirement of each process. The stoichiometric combustion of hydrogen and oxygen is given by Eq. 1.1.

Hydrogen combustion

$$2H_2 + O_2 \longrightarrow 2H_2O \tag{1.1}$$

As this work used air for oxidation instead of oxygen, the nitrogen in air needed to be included for calculation and the hydrogen combustion thermal efficiency in furnace (η_f) was assumed to be 85% [99]. The thermal requirement of

each process was the summation of the heat duty of all units. Reformer, calcination reactor, air reactor and furnace were considered to be adiabatic and the energy requirement is equal to heat duty (Q) of the reactor. For air reactor, the generated heat comes from oxidation of nickel. Cyclone and separator are considered to be adiabatic and heat loss from heat exchangers is neglected.

4.2   Experiments

The experimental section of this research were divided into 2 parts.

Part1: The Fe_2O_3/CaO-Al_2O_3 multifunctional catalysts were synthesized with different preparation methods. The material preparations, characterization and catalytic activity for H_2 production test were described following.

Materials preparation:

Iron (III) nitrate nonahydrate ($Fe(NO_3)_3 \cdot 9H_2O$, 98% Ajax Finechem) and aluminum nitrate nonahydrate ($Al(NO_3)_3 \cdot 9H_2O$, 99% Ajax Finechem) were used as iron and aluminum precursors. Calcium acetate monohydrate ($Ca(CH_3COO)_2 \cdot H_2O$, 99%) purchased from HiMedia was used as calcium precursor. Citric acid ($C_6H_8O_7$, 99.5%), used for material synthesis via sol-gel method was purchased from Ajax Finechem. All chemicals were used as received. The Fe_2O_3/CaO-Al_2O_3 multifunctional catalysts were synthesized with different preparation methods as follows.

Sol-gel method

For, multifunctional catalyst, a mass ratio of calcium to alumina of 70:30 and normalized with 5 wt% of iron was maintained. The iron, calcium and aluminum precursors were mixed with de-ionized (DI) water and the resulting mixture was

hydrolyzed for 2 h at 80 °C under constant stirring. Citric acid was used to peptize the slurry as a metal-complex agent with a fixed molar ratio $M:H_2O:H^+$ (M= Fe^{3+}, Ca^{2+} and Al^{3+}) of 1:50:1.2 under refluxed for 6 h at 105 °C. After hydrolysis, the resulting gel was dried at 110 °C overnight and calcined at 850 °C for 2 h at a heating rate of 10 °C min^{-1}. In some preparations, the iron precursor was added after peptizing the slurry to study the effect of this procedure. In this work, the effect of iron adding step was therefore studied; the as-prepared catalysts with iron precursor addition before and after peptization were denoted by 5FeCaAl and 5Fe*CaAl, respectively.

Mechanical mixing method

The Fe_2O_3 over $CaO-Al_2O_3$ catalysts prepared by mechanical mixing was carried out according to the method described in the previous literature [100]. The modification of CaO sorbent was firstly prepared via sol-gel route. Calcium and aluminum precursors with a mass ratio of 70:30 were mixed in DI water. Citric acid of the same molar ratio used in the previous preparation was added into the solution. The resulting solution was heated and stirred under reflux at 80 °C for 7 h and then left for 18 h at ambient temperature. The obtained wet gel was dried at 110 °C for 12 h and then calcined at 850 °C for 2 h. The iron salt precursor and as-synthesized modified CaO powder were crushed together to obtain homogeneous powder with 5wt % of iron. This mixture was calcined at 500 °C for 2 h with a heating rate of 10 °C min^{-1}. The resulting mixture was sieved to obtain particle with a size fraction of 106 μm. The catalyst produced in this method were denoted by Mec5Fe/CaAl.

Impregnation method

To prepare Fe_2O_3 over $CaO-Al_2O_3$ catalysts by incipient wetness impregnation, an aqueous solution of the iron precursor with a predetermined concentration was added drop-wisely on the sorbent powder prepared in the same way as the mechanical mixing method. The resulting slurry was left at room temperature for 4 h, dried in an oven at 110 °C overnight and calcined at 500 °C for 2 h. The samples prepared by this method were denoted by ImpXFe/CaAl where X is the mass ratio of iron at 5, 10 and 15 wt%, respectively.

In addition, to investigate the performances of multifunctional catalysts and the effect of preparation method, 5 wt% iron supported by commercial Al_2O_3 was also prepared for comparison. The sample was denoted by 5Fe/Al.

Materials characterization:

All prepared catalysts were characterized by X-ray diffraction (XRD) (D8 Advance, Bruker) to identify the crystalline phases in a 2θ range of 10°-80° with a step size of 0.04° and a scan speed of 0.5 s/step. The specific surface area, pore volume and pore size were measured by nitrogen adsorption/desorption with a Micromeritics Chemisorp 2750 and calculated based on BET and BJH models. The external morphology and elemental contents of the catalysts were determined by a scanning electron microscope (SEM), Hitachi S-3400 N, coupled with energy dispersive X-ray spectrometer (EDX), AMETEK EDAX, APOLLO X. Carbon formation on spent catalyst after reaction test and thermal information were examined by differential scanning calorimetry and thermo gravimetric analysis (DSC-TGA) with TA Instruments' SDT Q 600 analyzer in a temperature range of 25 to 1000 °C in air at a heating rate of 10 °C min^{-1}.

Hydrogen production:

Hydrogen production was performed in a quartz fixed-bed reactor of 15 mm inner diameter and 500 mm length. The reactor was installed in a vertical furnace as shown in Figure 18. Two grams of prepared multifunctional catalyst sandwiched between two lumps of quartz wool were placed in the reactor. The temperature of the catalytic bed was monitored and controlled through a thermocouple positioned in the center of the reactor. The inlet gas composition and flow rate were controlled by mass flow controllers. The particles were exposed to alternating reducing and oxidizing atmosphere. Before performing each experiment, the sample was pretreated at 850 °C for 30 min under N_2 flow (30 ml min^{-1}) to eliminate moisture content. Table 8 shows a summary of the sequential stages operating conditions in the SECLR process. H_2 production activity of the multifunctional catalysts were performed at 600 °C with a steam to ethanol ratio (*S/E*) of 4 under nitrogen atmosphere and a total flow rate of 50 ml min^{-1}. The duration of SECLR step was lasted for 180 min. Then, the reactor was purged by N_2 to remove gaseous products in the previous step. In oxidation step, the steam oxidation was optional and only made for stability test of iron-based oxygen carrier by further feeding H_2O for 60 min. After that, the air was introduced to re-oxidize the metal for 60 min at a flow rate of 30 ml min^{-1}. Finally, the furnace was heated to 850 °C for CO_2 sorbent regeneration under N_2 atmosphere for 60 min at a flow rate of 30 ml min^{-1}. The product gas compositions were analyzed by gas chromatography (GC-8A SHIMADZU) with two detectors: flame ionization detector (FID) for ethanol and high-density components and thermal conductivity detector (TCD) equipped with two columns: Molecular sieve5A and PoraPLOT Q for H_2, CO, CH_4 and CO_2. Breakthrough model was applied

to demonstrate composition profile of substances at outlet stream as a function of time.
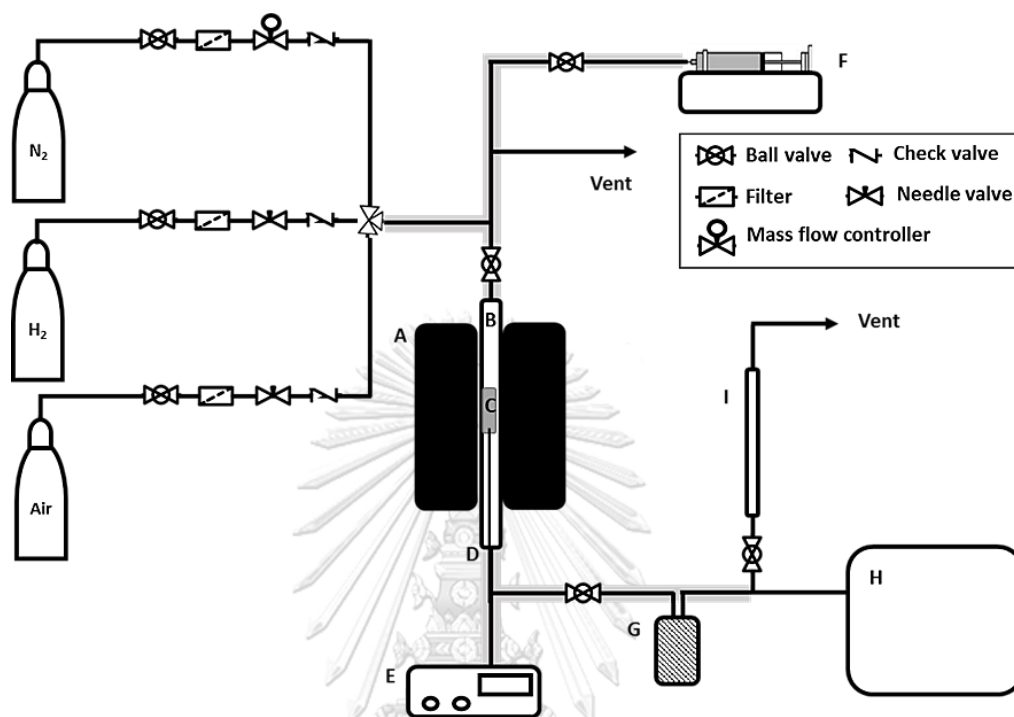
Figure 18 Schematic diagram of the experimental setup: (A) Heater; (B) Quartz reactor, ID =15 mm, length = 500 mm; (C) Catalytic bed; (D) Thermocouple; (E) Temperature controller; (F) Syringe pump; (G) Water trap; (H) Gas chromatograph; (I) Bubble flow meter.

Table 8 Operating conditions for each step of the SECLR process of ethanol in one cycle.

Step	Feed	Total flow rate (ml min^{-1})	Temperature (°C)	Duration (min)
(1) SECLR	C_2H_5OH and H_2O^a	20	600	180
	N_2	30		
(2) Purging	N_2	50	600	30
(3) Oxidation	H_2O^b	0.05	500	60
	Air	30	600	60
(4) Heating	N_2	50	850	30
(5) Calcination	N_2	30	850	60

^{a} Steam to ethanol ratio (S/E) = 4

^{b} Additional test for stability from water splitting (WS) reaction

Part2: The catalysts including Fe-MgAl, Ni-MgAl and Ni-Fe/MgAl were derived from hydrotalcite-like compounds. The material preparations, characterization and catalytic activity for H_2 production test were described as follows.

Materials preparation:

The Fe-Ni-Mg-Al HTcls precursors were synthesized through the co-precipitation method at a constant pH and room temperature. A nitrate solution of 1 M containing $Fe(NO_3)_3 \cdot 9H_2O$, $Ni(NO_3)_2 \cdot 6H_2O$, $Mg(NO_3)_2 \cdot 6H_2O$ and $Al(NO_3)_3 \cdot 9H_2O$ was added slowly to a 0.2 M Na_2CO_3 solution under stirring at room temperature. The pH value of the solution was adjusted with a 2 M NaOH and maintained at a pH of 10 ± 0.5. The molar ratio of divalent metals (Ni^{2+} and Mg^{2+}) to trivalent metals (Fe^{3+} and Al^{3+}) was fixed at 2 and the molar ratio of Fe/Ni for bimetallic oxygen carrier catalyst was 0.2 with the weight fraction of Ni+Fe at 10 wt %. The resulting suspension was

kept at room temperature for 24 h. The precipitates were filtered, and washed with deionized water and dried at 110 °C overnight. The dried precursors were ground to fine powders and then calcined at 800 °C for 5 h using a heating rate of 5 °C min^{-1}. The obtained materials were pressed and sieved to particles with 40-60 mesh size. The bi-functional oxygen carrier catalyst derived from Fe-Ni-Mg-Al hydrotalcite-like compounds are denoted as FeNi-MgAl.

For comparisons, two oxygen carrier catalysts derived from Fe-Mg-Al and Ni-Mg-Al hydrotalcite-like compounds were also prepared by co-precipitation method with the same procedure and amount of metal loading (10wt %), and denoted as Fe-MgAl and Ni-MgAl, respectively.

Materials characterization:

The X-ray diffraction (XRD) spectrums were performed on a Rigaku D/max-2500 diffractometer equipped with Cu K$_\alpha$ radiation (λ = 1.54056 Å) to identify crystalline phases in the catalysts. The data were collected in the 2θ range of 5-90° with a scan speed of 10° min^{-1} and a step of 0.02°. The Scherrer equation (Eq. 4.8) was applied to estimate average particle size (d$_{hkl}$):

$$d_{hkl} = \frac{k \cdot \lambda}{\beta_{hkl} \cos(\theta)} \tag{4.8}$$

where λ is the X-ray wavelength, β_{hkl} is the full-width at half-maximum in radian and θ is the Bragg's diffraction angle.

Inductively coupled plasma optical emission spectroscopy (ICP-OES) was employed to determine the elemental chemical analysis of calcined catalyst, using VISTA-MPX, Varian. Before each analysis, the samples were dissolved in the aqueous

solution and the concentrations of measured elements were close to the standard solutions.

Nitrogen (N_2) physisorption was conducted at 77 K by using a Micromeritics TristarII 3020 analyzer to measure textual properties. Prior to the experiment, the samples were degassed at 300 °C for 3 h. The surface area and pore properties were calculated by the Brunauer-Emmett-Teller (BET) and Barrett-Joyner-Halenda (BJH) method, respectively.

The surface morphologies of some of the fresh or spent catalysts were characterized by a scanning electron microscope (SEM) (Hitachi, Model S-4800, 5 kV) and a transmission electron microscopy (TEM) (JEM-2100F, 200 kV). For the TEM analysis, the samples were dispersed in anhydrous ethanol by using ultra-sonication and then suspended on an ultrathin Cu grid-supported carbon foil.

Temperature-programmed reduction (TPR), desorption (TPD), and oxidation (TPO) measurements were performed in chemisorption analyzer (Micromeritics AutoChem II 2920). H_2-TPR was employed to analyze the reduction behavior. Ca. 80 mg of samples obtained by calcination of the hydrotalcite precursors were loaded in the U-quartz microreactor, dehydrated at 300 °C for 1 h under Ar stream, and cooled to 80 °C in the same atmosphere. The analysis was carried out in a mixture of 10 vol % H_2 in Ar (30 ml min^{-1}), ramping the temperature from 80 °C to 900 °C at 10 °C min^{-1}. The CO_2-TPD was characterized to analyze the basic property on the surface of the catalysts. The same amount of samples were pretreated with 10% H_2 in Ar at 300 °C for 1 h then cooled down. The inlet gas was switched to CO_2 stream (50 ml min^{-1}) until CO_2 adsorption was saturated. The sample was heated to 900 °C at a heating rate of 10 °C min^{-1} for CO_2 desorption. The O_2-TPO experiments were performed to

investigate the coking characteristics of the used samples under a gas flow of 10 vol % O_2 in He at the flow rate of 30 ml min^{-1}. The consumption of each gas was monitored continuously with TCD gas chromatograph.

Coke characterization was analyzed by Raman spectroscopy in a Renishaw inVia reflex Raman spectrometer using an excitation wavelength of 532 nm, performing the analysis in several areas of the used sample for increased reproducibility.

The alternate pulse experiment was conducted on the same chemisorption analyzer (Micromeritics Autochem II 2920) connected with a Hiden QIC-20 mass spectrometer (MS) to understand the mechanism on bimetallic catalyst by sequential pulse of C_2H_5OH-H_2O vapor and CO_2. The calcined sample was heated at 300 °C for 30 min under Ar gas flow. Then, the temperature was increased to 500 °C followed by 10 pulses of C_2H_5OH-H_2O vapor (C_2H_5OH/H_2O = 3, 3 min $pulse^{-1}$ and 0.5 ml $pulse^{-1}$). After that, temperature was further increased to 800°C and the previous gas was removed by purging with 10 pulse of Ar. Finally, 10 pulses of CO_2 gas (3 min $pulse^{-1}$ and 0.5 ml $pulse^{-1}$) was subsequently introduced into quartz reactor and the sample was collected at different amount of CO_2 pulses (1, 5 and 10 pulses). The products from each period were detected by the online MS.

X-ray photoelectron spectroscopy (XPS) analysis was performed on a Perkin-Elmer PHI 1600 ESCA system with an Al K_α X-ray source (E = 1486.6 eV) to determine the surface chemical state changed of samples in different conditions from alternate pulse experiment.

In situ diffuse reflectance infrared Fourier transform spectroscopy (DRIFTS) of a fuel feed step on CLR by ethanol were carried out on a Thermo Scientific Nicolet

IS50 spectrometer, equipped with a Harrick Scientific diffuse reflection accessory, a mercury-cadmium-telluride (MCT) detector, and a Hiden QIC-20 mass spectrometer. Samples were first pretreated at 300 °C under 40 ml min^{-1} argon for 30 min and cooled down to 220 °C to collect a background spectrum. The liquid mixture of ethanol and water (*S/E* = 3) was bubble into the reaction cell by Ar stream (15 ml min^{-1}). The gaseous products were monitored by transmission infrared spectrometry and detected by MS.

Hydrogen production:

Catalytic performance for H_2 production on CLR from ethanol were carried out at atmospheric pressure in a fixed-bed reactor (900 mm length, 18 mm internal diameter) with alternating fuel and air feeding steps. Typically, the bi-functional catalyst (1 g, 40–60 mesh) was diluted with SiO_2 in the mass ratio of 1:2, and then loaded into a stainless steel tube reactor supported by quartz wool at constant temperature zone. The temperature of the reaction zone was monitored by a thermocouple and maintained by a tube furnace. Prior to each test, the oxygen carrier was oxidized by air (100 ml min^{-1}, 21 vol% O_2 and 79 vol% N_2) at 800 °C for 30 min, and then the air was shifted to pure N_2 (100 ml min^{-1}) for 10 min. A cycle consisted of fuel feed step for H_2 production and air feed step for re-oxidation of OC. In fuel feed step, a liquid mixture of ethanol and water (0.1 ml min^{-1}, C_2H_5OH/H_2O molar ratio of 1:3, weight hourly space velocity (WHSV) of 6000 h^{-1}) was fed to the reactor using a HPLC pump (P230, Elite, China) which was vaporized at 180 °C into gaseous reactants. The product components from reactor (ethanol, H_2, CO, CO_2 and CH_4) were detected and analyzed online by the gas chromatograph (Agilent Micro GC 490) with interval of 2 min and mass spectrometer. For the subsequence of air feed

step, N_2 was entered to purge the reactor, followed by an air (100 ml min^{-1}, 30 min) at 800 ℃ for complete oxidation of oxygen carrier.

CHAPTER V

Performance comparison among different multifunctional reactors operated under energy self-sufficiency for sustainable hydrogen production from ethanol

This study presents the results of hydrogen production from renewable ethanol through four reforming processes: conventional ESR, SESR, CLR and SECLR with combustion of a fraction of hydrogen product for heat supply within the system. The performances in terms of net hydrogen productivity, hydrogen purity, ethanol conversion, CO_2 capture ability and thermal efficiency of these processes from simulation on the basis of self-sufficiency with net hydrogen production maximized were compared.

5.1 Validation

The simulation was first validated for the SECLR of methane using NiO as oxygen carrier and CaO as CO_2 sorbent under the same condition employed by Rydén and Ramos [61]: a reforming pressure of 1 bar, a H_2O/CH_4 of 2, a NiO/CH_4 of 1 and a CaO/CH_4 of 1. The validation results of SECLR simulation are shown in Table 9 comparing hydrogen productivity, methane conversion, hydrogen purity and CO_2 capture ability from our process with those from Rydén and Ramos [61]. Our results show good agreement with deviations of hydrogen productivity, methane conversion, hydrogen purity and CO_2 capture ability from the reference by only 1.25%, -0.37%, -

0.32% and 0.34%, respectively. Therefore, this simulation model was deemed reliable for further investigation.

Table 9 Simulated validation results from this study and results of reference by Rydén and Ramos [61] for equivalent SECLR process under the same condition.

Simulation	Value	Reference	Simulation deviation (%)
H_2 productivity (kmol/kmol)	2.846	2.811	1.25
CH_4 conversion (%)	96.64	97.0	-0.37
H_2 purity (%)	98.38	98.7	-0.32
CO_2 capture ability (%)	95.33	95.0	0.34

5.2 Base case calculation

The base case simulation of an SECLR was performed at an ethanol feed flow rate of 1 kmol/h, reforming temperature of 600°C, pressure of 1 bar, a *S/E* ratio of 4, a calcium oxide to ethanol ratio (*CaO/E*) ratio of 4, and a nickel oxide to ethanol (*NiO/E*) ratio of 1 with amount of solid split fraction of 0.95 for **α** and 0.05 for **β** following Ref. [62]. The performance of the process under these base case conditions is shown in Table 10. Hydrogen productivity of 4.1 kmol/kmol was observed with 77% purity and complete ethanol conversion. The CO_2 capture ability is quite low because the amount of adsorbent is not enough for CO_2 adsorption and the fractions of solid circulation (**α** and **β**) are not appropriate.

The energy requirement of SECLR at the base case was approximately 0.07 MW, which is mainly the requirement from the endothermic reverse reaction of Eq. 2.12 to regenerate $CaCO_3$ in the calcination reactor. This energy demand is supplied

by combustion of a portion of the produced hydrogen. The theoretical combustion of hydrogen requires 2 moles of hydrogen and 1 mole of oxygen for complete combustion. The number of moles of air per mole of oxygen for combustion is given by Eq. 5.1.

$$\text{Number of moles of air} = \frac{\text{Mole } O_2}{0.21} \tag{5.1}$$

The stoichiometric air/fuel (*A/F*) ratio for combustion of hydrogen with air is given by Eq. 5.2.

$$A/F = \left(\frac{\text{moles of air}}{\text{moles of hydrogen}}\right) \tag{5.2}$$

In practice, 10% excess of air must be fed to a furnace for complete combustion [101]. Therefore, the number of moles of air and the *A/F* ratio are 5.2 and 2.6, respectively. The amount of hydrogen in air that can be used as a fuel ranges from 4 to 75% which causes hydrogen to be combustible, meaning that hydrogen's flammability range is very wide in the air. The hydrogen to air mixture in these calculations is 27.6% which is close to the stoichiometric hydrogen combustion that is considered as an optimal condition [35]. With a furnace's thermal efficiency of 85%, the SECLR process requires 35% of hydrogen productivity to fulfill the energy requirement of 0.07 MW, producing a net hydrogen of 2.65 kmol/kmol and having an overall thermal efficiency of 51%.

Table 10 Process performance of SECLR for hydrogen production from ethanol at base case condition.

Parameter	Value
Ethanol feed rate (kmol/h)	1
S/E ratio (-)	4
Temperature of reformer (°C)	600
Temperature of calcination reactor (°C)	900
Temperature of air reactor (°C)	900
Pressure (bar)	1
CaO/E ratio (-)	4
NiO/E ratio (-)	1
Solid fraction of CR to AR, α (-)	0.95
Solid fraction of AR to RR, β (-)	0.05
H_2 productivity (kmol/kmol)	4.1
Ethanol conversion (%)	100
H_2 purity (%)	77
CO_2 capture ability (%)	39
Energy requirement (MW)	0.07
Hydrogen utilization (%)	35
Net hydrogen (kmol/kmol)	2.65
Thermal efficiency (%)	51

5.3 Determination optimal conditions for maximum net hydrogen production

The energy requirement and hydrogen yield are important factors for identifying the optimal process for hydrogen production. They depend on a number of operating conditions such as reactor temperature, pressure and flow rate. Therefore, the determination of the optimal condition with maximum net hydrogen on each process is required in performance comparison among different processes.

For conventional ESR process, the reforming temperature and *S/E* ratio are the two main factors influencing hydrogen yield and energy demand. Figure 19 illustrates the effects of reforming temperature and *S/E* ratio on hydrogen productivity, net hydrogen and energy requirement. Increasing reforming temperature results in higher hydrogen productivity because steam reforming is endothermic and therefore is thermodynamically favorable at high temperatures. Increasing the *S/E* ratio also increases the hydrogen productivity because the main reaction (Eq. 2.1) is shifted toward the products. However, operating at a high temperature and a high *S/E* ratio requires a large amount of energy. Therefore, more hydrogen was diverted to furnace for combustion. This leads to a lower value of net hydrogen. In the range in our study, net hydrogen becomes zero as the *S/E* ratio is increased to 2 and 7 at the reforming temperatures of 400 and 500 °C, respectively. This indicates that all hydrogen produced was sent to the furnace. Beyond these conditions the process even requires energy from external sources. The highest net hydrogen from the conventional ESR process was obtained at the temperature of 700 °C and the *S/E* ratio of 3. The hydrogen productivity, net hydrogen and purity of hydrogen at these conditions are 5.6 kmol/kmol, 3.2 kmol/kmol and 73.5%, respectively, with an energy requirement of 0.15 MW.

Figure 19 Top: Effects of reforming temperature on energy requirements of ESR. Bottom: Effect of steam to ethanol ratio on hydrogen productivity (solid lines) and net hydrogen (dashed lines)

In addition to the reforming temperature and *S/E* ratio, the amount of solid used in the system also has a significant impact on the process performance. The sorption enhanced processes with *in situ* CO_2 separation has CaO as a solid sorbent circulated in the system. Figure 20 indicates the effect of the calcium oxide to ethanol ratio (*CaO/E*) on hydrogen productivity (kmol/kmol), net hydrogen (kmol/kmol) and energy requirement (MW) at various reforming temperatures and *S/E* ratios. The reforming temperature in sorption enhanced processes with CaO as the sorbent is limited to 700 °C, beyond which CO_2 adsorption by CaO is not favorable.

The simulation results showed that at *CaO/E* ratios of 1 to 5, the hydrogen productivity increases with the *CaO/E* ratio because the immediate capture of CO_2

shifts the equilibrium of reactions Eqs. 2.1 and 1.3 toward the products. The amount of net hydrogen also increases even though energy requirements are higher due to the heat from CO_2 adsorption of CaO (Eq. 2.12) can be supplied during the steam reforming and other side reactions occurred in the reformer. At *CaO/E* ratios larger than 5, the performance (hydrogen productivity, net hydrogen and energy requirements) remain constant, suggesting that the amounts of CO_2 sorbent became excessive.

In terms of energy requirement, when the reformer is operated at low temperatures, most of the energy demand arises from the calcination reactor as calcination needs more energy to heat the outlet stream from the reformer (TOCAL). On the other hand, when the reformer is operated at high temperatures, the main energy requirement is from the steam reforming reactions in the reformer. The highest net hydrogen was observed at the temperature of 500 °C, *S/E* ratio of 5 and *CaO/E* ratio of 5. The productivity, net hydrogen and purity of hydrogen at these optimal operating conditions were 5.7 kmol/kmol, 3.5 kmol/kmol and 98.5 %, respectively, with an energy requirement of 0.14 MW.

It is noteworthy that if only the hydrogen productivity is considered, the optimal conditions of SESR will be found at the temperature of 500 °C and *S/E* ratio of 10. A large energy requirement and low net hydrogen are observed at these conditions as shown in Figures 20(b) and (c). Therefore, the energy requirement is important and directly affects the return and cost of the production.
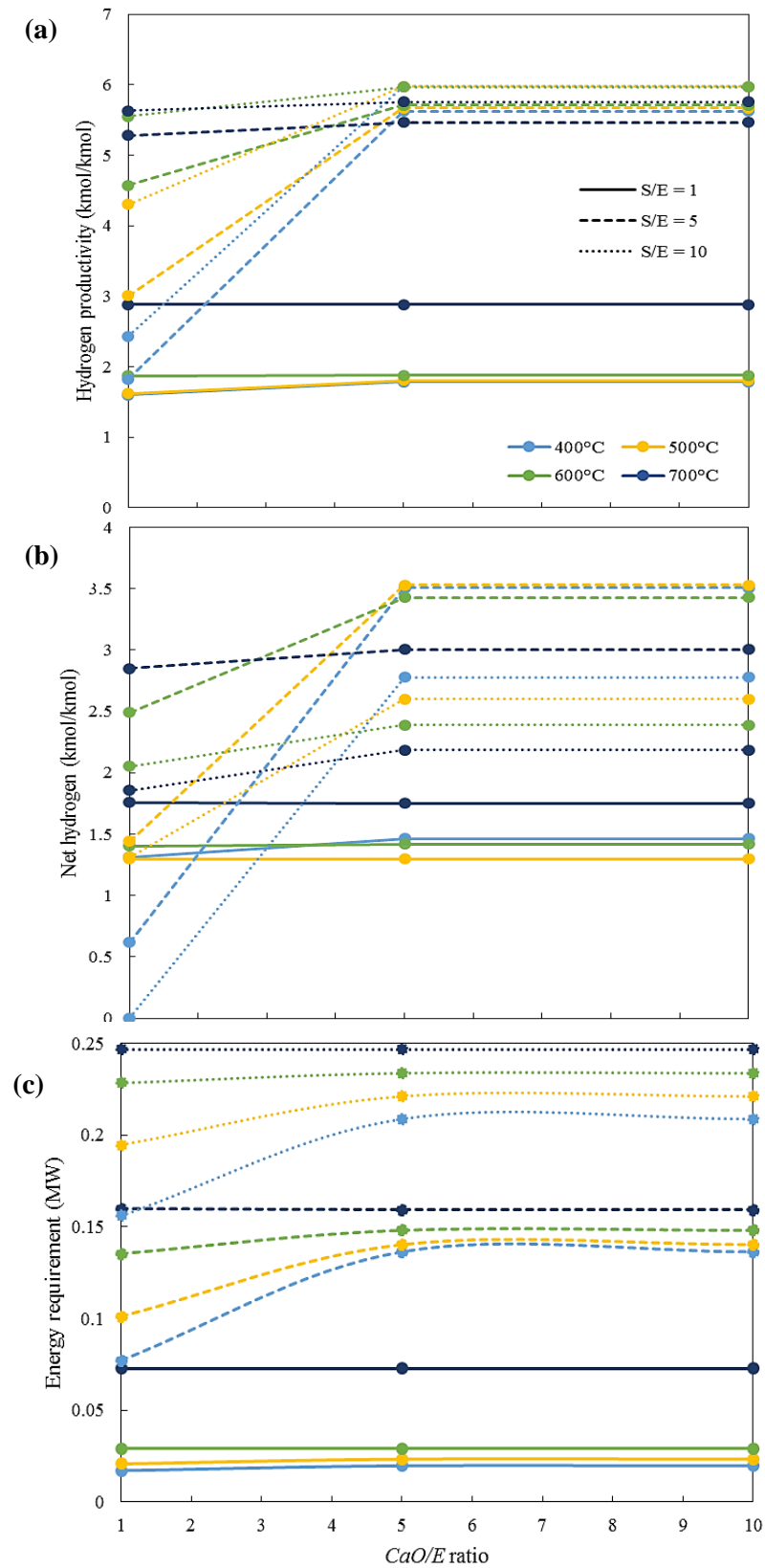
Figure 20 Effects of CaO/E ratio, steam to ethanol ratio and reforming temperature on hydrogen productivity (a), net hydrogen (b) and energy requirement (c) of SESR process

The CLR process also has a solid oxygen carrier NiO circulated in the system. Figure 21 shows the effects of nickel oxide to ethanol ratio (*NiO/E*) on hydrogen productivity (kmol/kmol), net hydrogen (kmol/kmol) and energy requirement (MW) at various parameters (Table 7). Increasing *NiO/E* ratio from 1 to 5 decreases the hydrogen productivity slightly as a portion of ethanol was oxidized to undesired CO_2 and CO according to Eqs. 2.13-2.18. This results in lower purity of hydrogen compared with the sorption enhanced process. Nevertheless, the negative effect of *NiO/E* ratio on the hydrogen production is significantly weaker than the positive effect of the sorbent due to the NiO reduction is firstly occurred and fast reaction, which is unlikely with CaO, implied that the CO_2 concentration has a huge impact on process performance. At low *NiO/E* ratios, high temperatures and *S/E* ratios, a higher hydrogen productivity and energy requirement are observed as the steam reforming reactions become dominant leading to low amount of net hydrogen. Nevertheless, the net hydrogen increases when the *NiO/E* ratio increases as heat is recovered from oxygen carrier regeneration, especially with the negligible negative effect of *NiO/E* ratio beyond 5. Reforming temperature of 700 °C, *S/E* ratio of 10 and *NiO/E* ratio of 1 offered the highest hydrogen productivity but not the highest net hydrogen. The latter was observed at temperature of 700 °C, *S/E* ratio of 5 and *NiO/E* ratio of 5. The productivity, net hydrogen and purity of hydrogen at these conditions are 4.3 kmol/kmol, 2.7 kmol/kmol and 68%, respectively, with energy requirement of 0.1 MW.
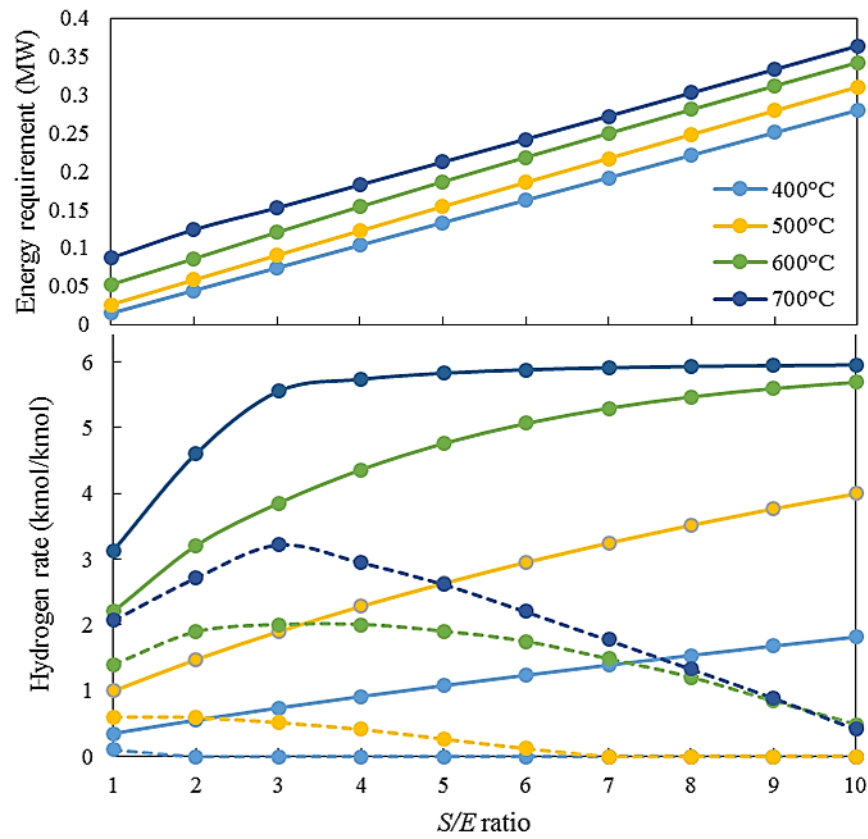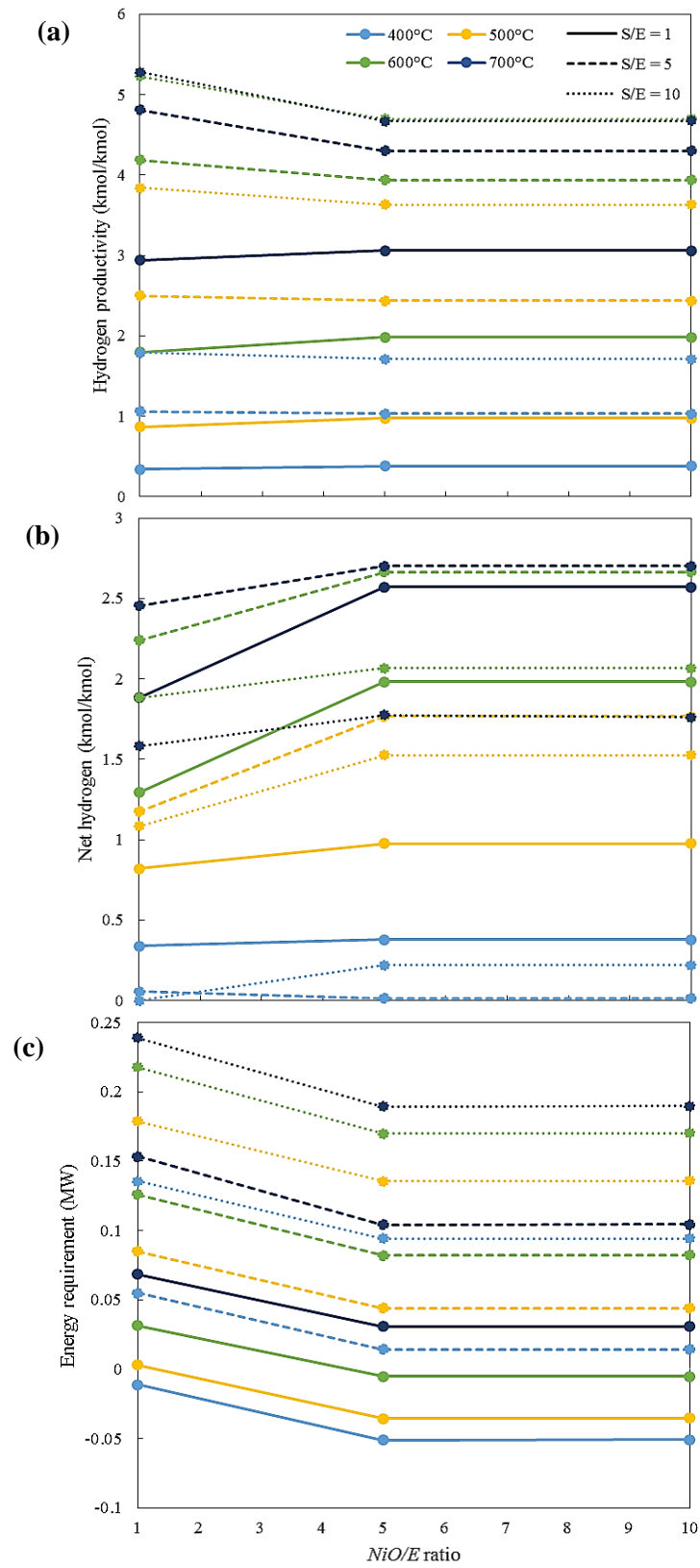
Figure 21 Effects of NiO/E ratio, steam to ethanol ratio and reforming temperatures on hydrogen productivity (a), net hydrogen (b) and energy requirement (c) of CLR process

As the SECLR process was designed with the recirculating solids from calcination reactor to reformer (1-α) followed by Rydén and Ramos [61] and solids from air reactor directly to the reformer (β) according to Udomchoke et al. [62]. The advantages of splitting the fraction of NiO and CaO directly to the reformer are higher conversion rate and hydrogen productivity as the temperature in reformer and CO_2 adsorption rate increase. The effect of solid recirculation controlled by splitter was investigated in term of solid split fraction. Our result of the effect of solid split fraction is shown in Figure 22 which confirms the result of Udomchoke et al. in the higher hydrogen productivity and purity compared without recirculating solids (α=1 and β=0). The hydrogen productivity and purity reach to the maximum at α=0.6 and β=0.1. Moreover, there was no effect when splitting solid from calcination to the reformer more than this fraction (α < 0.6).
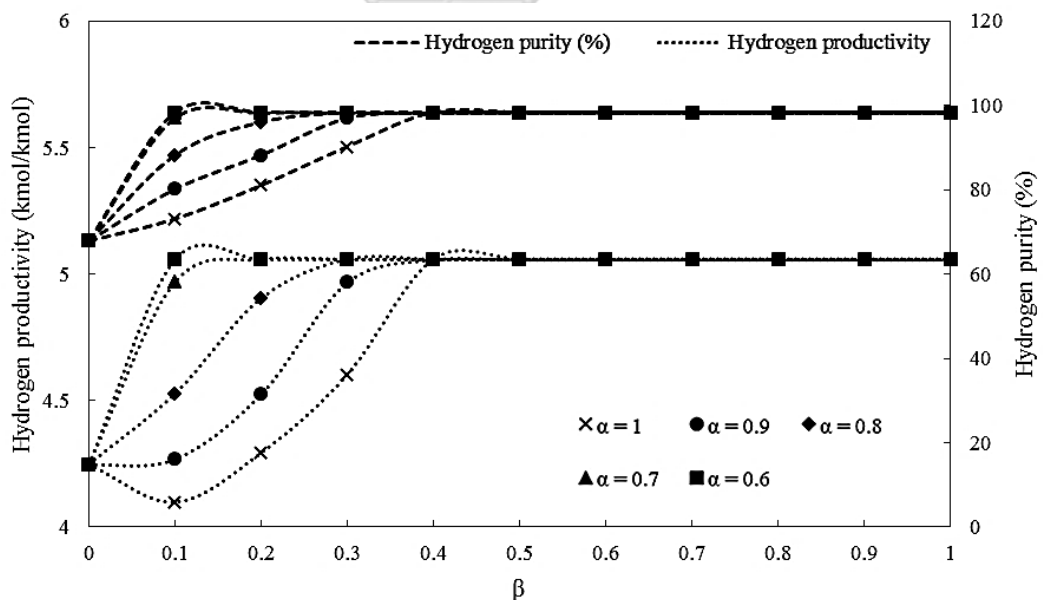
Figure 22 Effects of α and β on hydrogen productivity and purity of SECLR process at CaO/E = 5 and NiO/E = 5

Figure 23 illustrates the hydrogen productivity, net hydrogen and energy requirement of SECLR process as a function of reforming temperature and *S/E* ratio with solid split fractions of **α** and **β** equal to 0.6 and 0.1, respectively. As would be expected, the hydrogen productivity increases with increasing of *S/E* ratio and reforming temperature. The lower hydrogen productivity was observed when operating at temperature 700 °C because of the reduction in adsorption capacity of CaO and exothermic carbonation reaction (Eq. 2.12). For the net hydrogen and energy requirement, the SECLR process relatively consumes lower amount of energy compared to other processes leading to higher net hydrogen. From the figure, it can be seen that the hydrogen productivity at 500 and 600 °C is similar; however, the energy consumption at 600°C is higher. Therefore, the optimal operating condition of SECLR process with the highest net hydrogen was observed at temperature of 500 °C and *S/E* ratio of 5. At this condition, the productivity, net hydrogen, purity of hydrogen and energy requirement are 5.1 kmol/kmol, 4.4 kmol/kmol, 99% and 0.03 MW, respectively.
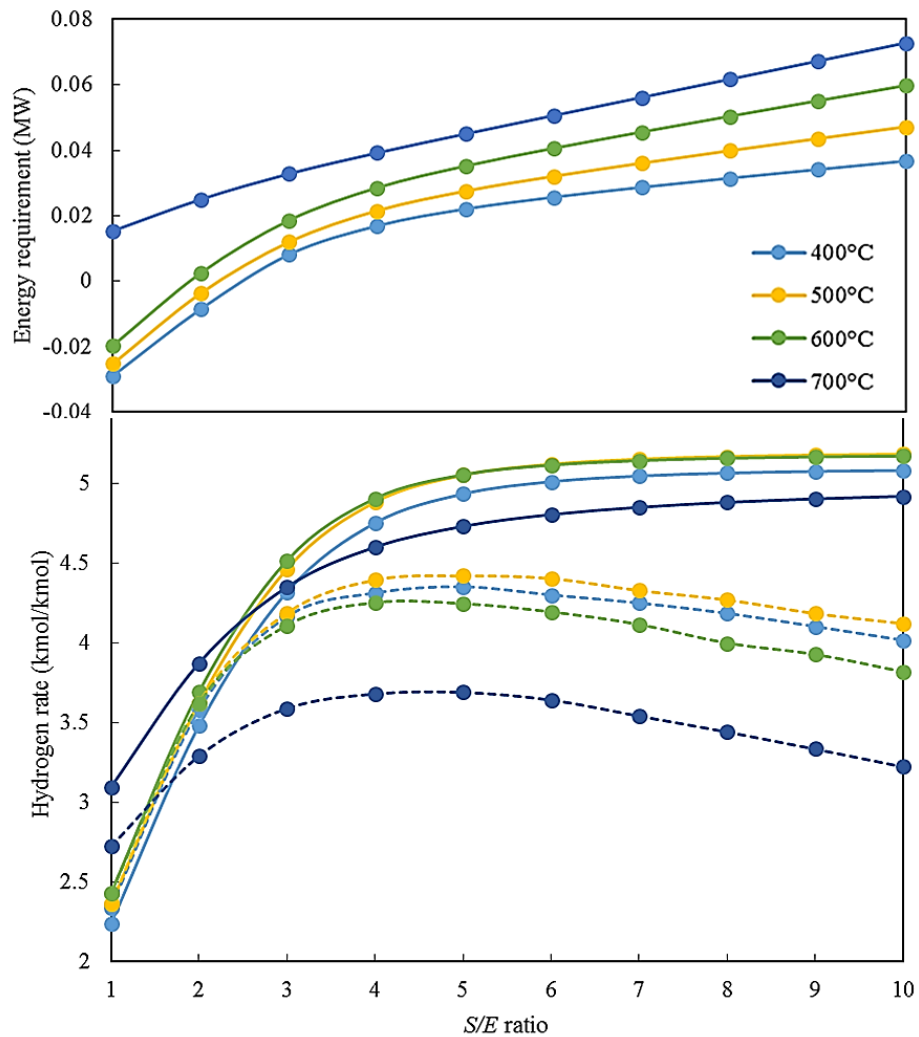
Figure 23 Top: Effects of reforming temperature on energy requirements of SECLR. Bottom: Effect of steam to ethanol ratio on hydrogen productivity (solid lines) and net hydrogen (dashed lines) at CaO/E = 5, NiO/E = 5, α=0.6 and β=0.1

5.4 Performance comparison for hydrogen production from different processes

The performance of hydrogen production processes including conventional ESR, SESR, CLR and SECLR from ethanol at their optimal conditions is shown in Table 11. The results clearly observed the complete of ethanol conversion under all studied conditions. The conventional ESR process offered hydrogen productivity of

5.6 kmol/kmol with 73.5% purity and most of energy consumption up to 0.15 MW. This process required 42% of hydrogen productivity to combust in furnace for sufficient supply in the system which is given net hydrogen only 3.2 kmol/kmol as it involves several steps, including reformer, two shift reactors and purification unit, and more severe operating condition (up to 700 °C) than the sorption enhanced processes. The conventional ESR has a similar tendency with CLR process, as high hydrogen was produced at high temperature where steam reforming reaction was dominant. Therefore, the optimal condition of these processes are rather similar. As the optimal condition of CLR requires higher steam, it leads to lower CH_4 and higher CO_2 concentration in outlet stream resulting in low purity.

Hydrogen can be produced from CLR process at approximately 4.3 kmol/kmol with 68% purity and the process requires 37.2% of hydrogen productivity for combustion to fulfill with energy demand of 0.1 MW and finally remains net hydrogen of 2.7 kmol/kmol. The CLR process obviously consumes lower amount of hydrogen to burn and supply in the system as it has significant advantage in heat providing which is heat from re-oxidation in the air reactor can provide to the reformer by solid oxygen carrier. The thermal efficiency of conventional ESR and CLR processes are 62% and 52%, respectively. Even though the conventional ESR does not provide energy to the system, this process produces a good yield and results in higher thermal efficiency.

In sorption enhanced processes, both of SESR and SECLR were obtained the same optimal operating condition from simulation results in the previous section. The SESR was found to produce hydrogen approximately 5.7 kmol/kmol with energy requirement of 0.14 MW. This process required 37.8% of hydrogen productivity in the

combustion section which remains net hydrogen 3.5 kmol/kmol. The acquired energy provided to the calcination reactor and the reformer as reverse Eq. 2.12 is highly endothermic and only heat from CO_2 adsorption by CaO disable enough supply in the system. The SECLR slightly produced hydrogen less than SESR which is 5.1 kmol/kmol. However, it consumed the lowest amount of energy of 0.03 MW and required only 12.5% of hydrogen productivity in combustion section as the re-oxidation of oxygen carrier and sorbent's carbonation in the regeneration cycle are exothermic reactions and can provide heat for highly endothermic reaction in the reformer and the calcination reactor. Therefore, the highest net hydrogen was obtained from SECLR which is equal to 4.4 kmol/kmol. Moreover, providing heat from solid in the system leads to sorption enhanced processes enable to operate at a lower temperature with high purity of hydrogen. The CO_2 capture ability of both processes are over 95% resulting in high purity of hydrogen which is 98.5% for SESR and 99% for SECLR. As expected, the thermal efficiency of SECLR is up to 85% which is higher than SESR process (68%) as it provides better performance in heat management in the system. For the lower thermal efficiency of ESR, CLR and SESR, these processes would be accounted for cost of heat addition. Therefore, SECLR process reveals several advantages to produce highest net hydrogen with high purity and low energy requirement.

Table 11 Performance comparison of different hydrogen production processes including conventional ESR, SESR, CLR and SECLR at optimal condition.

Parameter	ESR	SESR	CLR	SECLR
Ethanol feed rate (kmol/h)	1	1	1	1
S/E ratio (-)	3	5	5	5
Temperature of reformer (°C)	700	500	700	500
CaO/E ratio (-)	-	5	-	5
NiO/E ratio (-)	-	-	5	5
H_2 productivity (kmol/kmol)	5.6	5.7	4.3	5.1
Ethanol conversion (%)	100	100	100	100
H_2 purity (%)	73.5	98.5	68	99
CO_2 capture ability (%)	-	95.8	-	98
Energy requirement (MW)	0.15	0.14	0.1	0.03
Hydrogen utilization (%)	42	37.8	37.2	12.5
Net hydrogen (kmol/kmol)	3.2	3.5	2.7	4.4
Thermal efficiency (%)	62	68	52	85

CHAPTER VI

Fe_2O_3/CaO-Al_2O_3 multifunctional catalyst for hydrogen production by sorption enhanced chemical looping reforming of ethanol

This work focuses on developing multifunctional catalysts, which combine a metal-based reforming catalyst and an oxygen carrier as well as a carbon dioxide sorbent, to facilitate mass transfer and improve catalytic activity and recyclability applied for the SECLR process of ethanol. The combination of iron-based oxygen carrier and CaO-based sorbents into multifunctional material is the most important issue as phase formation on catalytic surface affects the oxygen transfer capacity of iron oxides and adsorption capacity of calcium oxide. Material preparation as well as metal oxide content are found to strongly affect phase composition of the material and H_2 production. In this study, the use of Fe_2O_3 as oxygen carrier combined with CaO-Al_2O_3 sorbent in the SECLR of ethanol process for H_2 production was proposed. The effect of preparation method on phase formation of Fe-based multifunctional catalysts was investigated on their activity and stability over multiple cycles of operation.

6.1 Fresh catalyst characterization

The diffractograms of fresh Fe-based multifunctional catalysts prepared by different methods are shown in Figure 24. The samples synthesized by the sol-gel route, 5FeCaAl and 5Fe*CaAl, showed the formation of $Ca_2Fe_2O_5$ phase at diffraction peaks of 2θ = 24, 26.8, 29.2, 33, 36.6, 41.2, 43.4 and 59.9° (JCPDS 47-1744), $FeAl_2O_4$

spinel at 2θ = 31 ° (JCPDS 34-0192), $Ca_9Al_6O_{18}$ at 2θ = 47.7 ° (JCPDS 32-0150) and CaO at 2θ = 32.3, 37.3, 53.9, 64.2 and 67.4° (JCPDS 48-1467). Changing steps of iron precursor addition after acid peptization (5Fe*CaAl), the sol-gel method still promoted the formation of the $Ca_2Fe_2O_5$ mixed phase but the decreased intensity of this phase was observed, indicating relatively lower content of $Ca_2Fe_2O_5$. However, other phases in this sample also had a lower peak intensity than the conventional sol-gel method (5FeCaAl) because the duration for phase transformation was decreased. The XRD pattern of the sample prepared by mechanical mixing (Mec5Fe/CaAl) showed the diffraction peaks attributed to Fe_2O_3 at 2θ = 23.2, 32.9, 35.6 and 47.3° (JCPDS 39-0238), CaO at 2θ = 32.1, 37.2, 53.8, 64.1 and 67.2°, and $Ca_2Fe_2O_5$ at 2θ = 26.8, 32.9, 43 and 59.9°. The Fe_2O_3 phase with the lowest $Ca_2Fe_2O_5$ peak intensity was clearly observed only from sample prepared by mechanical mixing method. This implied that heating iron precursor in solid state could release water and nitrate molecule quickly, decreasing the formation of $Ca_2Fe_2O_5$ or other phases. For the catalysts prepared by impregnation method, the formation of $Ca_2Fe_2O_5$ phase at 2θ = 33.1, 36.6 and 55.2° was found regardless of Fe content due to strong interactions between the iron phase and the calcium sorbent. The inert $Ca_{12}Al_{14}O_{33}$ phase from modified CaO also presented at diffraction peaks of 2θ = 18, 27.8, 29.7, 36.6, 41.1, 46.7 and 57.2° (JCPDS 48-1882) and its intensity decreased with increasing iron contents from 5 to 15 wt % later distribution of $Ca_2Fe_2O_5$ phase over catalyst surfaces. However, the represented peaks of Fe_2O_3 phase observed at 2θ = 35.5 and 47.3° could be detected when the catalyst prepared with Fe contents of 10 and 15 wt %. This might be due to the positioning of iron oxide inside the material. Therefore, the XRD results showed that the catalyst preparation using iron precursor

in a solid state could suppress the formation of $Ca_2Fe_2O_5$, leading to a higher content of Fe_2O_3, but destroyed the inert $Ca_{12}Al_{14}O_{33}$ phase in sorbent's structure. In contrast to the mechanical mixing method, impregnation method allowed the existence of $Ca_{12}Al_{14}O_{33}$ phase in the sorbent while the sol-gel method promotes the stronger interactions between the iron phase and the sorbent.
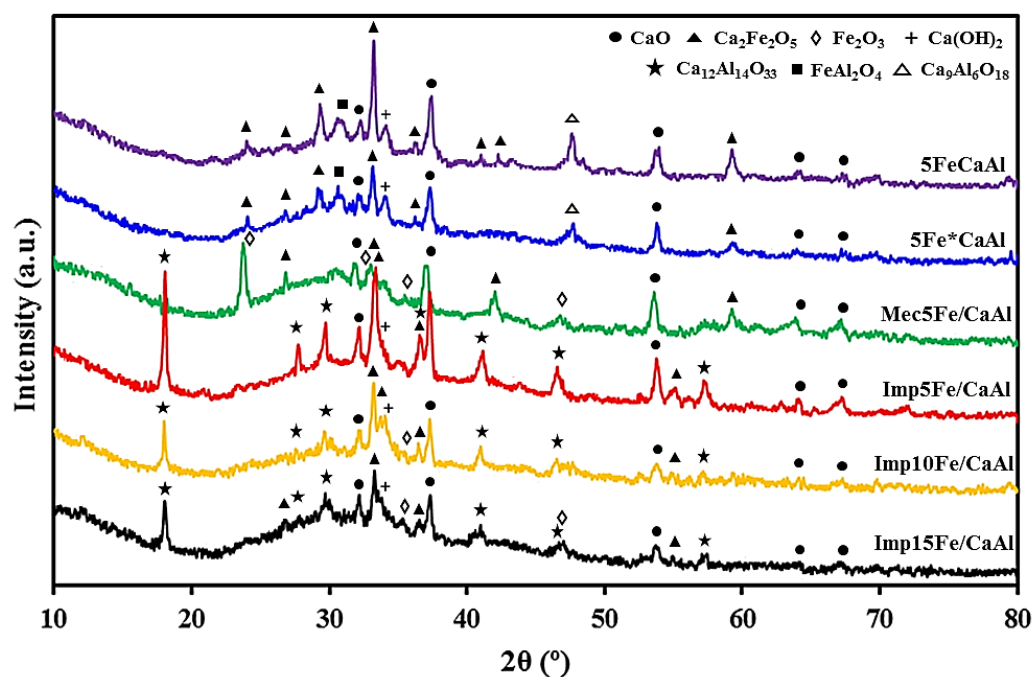
Figure 24 XRD patterns of the $Fe_2O_3/CaO-Al_2O_3$ multifunctional catalysts prepared through different synthesis methods (sol-gel, mechanical mixing and impregnation) with different iron contents (5, 10 and 15 wt %).

Table 12 Crystallites size, surface area, pore volume and average pore size of Fe-based multifunctional materials.

Multifunctional catalysts	Preparation method	Crystallite size (nm)[a]				Specific surface area (m² g⁻¹)[b]	Pore volume (cm³ g⁻¹)[b]	Average pore size (nm)[b]
		CaO	$Ca_2Fe_2O_5$	$Ca_{12}Al_{14}O_{33}$	Fe_2O_3			
5FeCaAl	Sol-gel	41	57	-	-	8.7	0.035	14.9
5Fe*CaAl		30	44	-	-	11.7	0.06	17.6
Mec5Fe/CaAl	Mechanical mixing	32	27	-	38	5.7	0.03	21.8
Imp5Fe/CaAl		47	38	63	-	18.3	0.08	18.2
Imp10Fe/CaAl	Impregnation	54	48	79	-	7.9	0.022	10.4
Imp15Fe/CaAl		58	52	87	-	7.9	0.025	11.6

[a] Obtained from XRD analysis.

[b] Obtained from N_2 physisorption

The crystallite size of CaO, $Ca_2Fe_2O_5$, $Ca_{12}Al_{14}O_{33}$ and Fe_2O_3 of all samples calculated based on Scherrer's equation are shown in Table 12. The CaO and $Ca_2Fe_2O_5$ crystallite sizes of 5FeCaAl sample synthesized by sol-gel method were 41 and 57 nm whereas the CaO and $Ca_2Fe_2O_5$ crystallite sizes of 5Fe*CaAl were 30 and 44 nm. Adding iron precursor after acid peptization (5Fe*CaAl) made the crystallization period shorter than mixing precursors together at the beginning (5FeCaAl) leading to the lowering of ordered material structure, hence the crystallite size decreased [102]. By mechanical mixing, the CaO crystallites of Mec5Fe/CaAl also had a small size of 32 nm with the Fe_2O_3 crystallite size of 38 nm. Furthermore, the smallest of $Ca_2Fe_2O_5$ crystallite size of 27 nm was found in this sample. For impregnation route, the CaO, $Ca_2Fe_2O_5$ and $Ca_{12}Al_{14}O_{33}$ crystallite size of Imp5Fe/CaAl were 47, 38 and 63 nm, respectively. The crystallite size of each phase grew gradually with increasing Fe content. It should be noted that the sample with 5 wt % loading of Fe provided better dispersion since smaller crystallite sizes were obtained. The presence of $Ca_{12}Al_{14}O_{33}$ in the samples prepared by impregnation method gave higher crystallite size of CaO as shown in Figure 26. Thus, the materials prepared by modified sol-gel and mechanical mixing methods presented higher dispersion with smaller CaO crystallite size when compared with the sol-gel and impregnation methods. However, with 5 wt% Fe loading, the sol-gel method preferred to form $Ca_2Fe_2O_5$ during the topological transformation of calcium and iron precursors as it provided the largest $Ca_2Fe_2O_5$ crystallite size.

The specific surface area, pore volume and pore size diameter analyzed from N_2 adsorption/desorption isotherm are also listed in Table 12. The synthesis routes had an effect on textural properties of multifunctional materials. The Imp5Fe/CaAl sample possessed the highest specific surface area and pore volume of 18.3 m^2 g^{-1} and 0.08 cm^3 g^{-1}, respectively. Nevertheless, no significant change was observed when the iron content increased from 10 to 15 wt %. For the samples prepared by sol-gel method, adding the iron precursor after peptization (5Fe*CaAl) offered higher specific surface area, pore volume and pore size than adding the iron before peptization (5FeCaAl). This is possibly due to the absence of iron precursor in hydrolysis which increased calcium and aluminum precursors' breakdown into interatomic bond to interact with, e.g., Ca-O, Ca-Al and Al-O, originated of porous $CaO-Ca_9Al_6O_{18}$. The catalysts synthesized by mechanical mixing (Mec5Fe/CaAl) had a small surface area of 5.7 m^2 g^{-1} with a pore volume of only 0.03 cm^3 g^{-1}. This indicates the influence of the state of the precursors. The precursors interacting in solution resulted in the hydration of CaO, forming $Ca(OH)_2$, which could increase the pore volume [103].
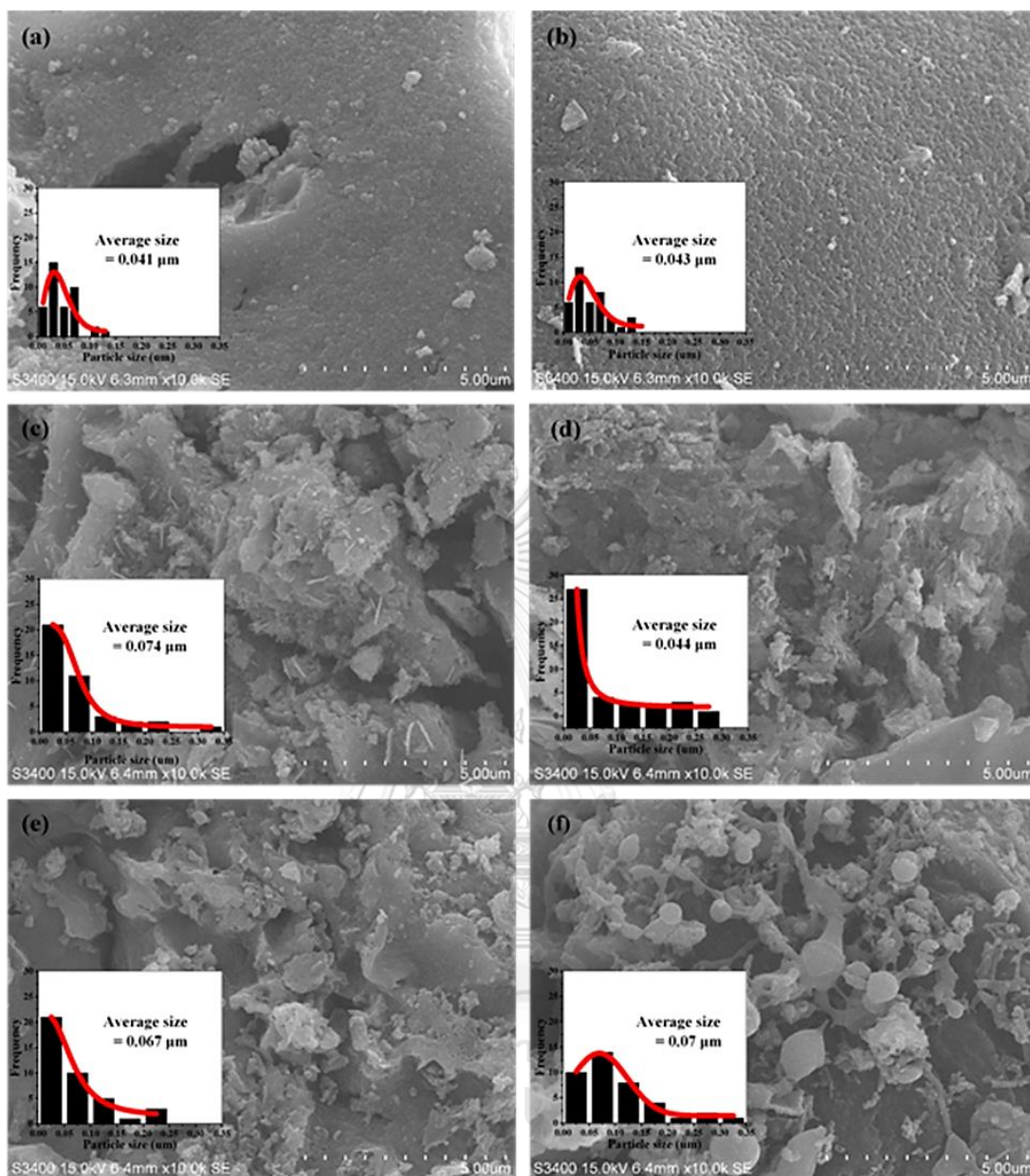
Figure 25 SEM micrographs and particle size distribution curve of the freshly prepared
Fe_2O_3/CaO-Al_2O_3 multifunctional catalysts: (a) 5FeCaAl, (b) 5Fe*CaAl, (c) Mec5Fe/CaAl, (d)
Imp5Fe/CaAl, (e) Imp10Fe/CaAl and (f) Imp15Fe/CaAl.

Figure 25 illustrates morphology and particle size distribution of Fe-based/CaO-Al$_2$O$_3$ multifunctional materials pictured by SEM. The samples synthesized via sol-gel formed homogeneous phase. The 5Fe*CaAl (Figure 25(b)) had more uniform surface than 5FeCaAl (Figure 25(a)). On the other hand, the samples prepared by mechanical mixing and impregnation were composed of heterogeneous particles of blades and irregular shapes (Figures 25(c)-(f)). From the particle size distribution graphs, it is obviously observed that the particle size of the sample obtained by solid state reaction was larger than those obtained by sol-gel method. The particle size of the samples prepared sol-gel route were in the range 0.01-0.14 μm and the average size was 0.042 μm. The mechanical mixing route showed the largest average particle size of 0.074 μm and the particle size was broadened in 0.01-0.35 μm. The average particle size of the samples synthesized by the impregnation route was found to depend on the amount of Fe loading. The Imp5Fe/CaAl exhibited the lowest average size of 0.043 μm compared to the Imp10Fe/CaAl (0.067 μm) and the Imp15Fe/CaAl (0.07 μm) with the distribution range of 0.01-0.35 μm. The difference in size could be due to the presence of different amounts of aggregates on catalytic surface.
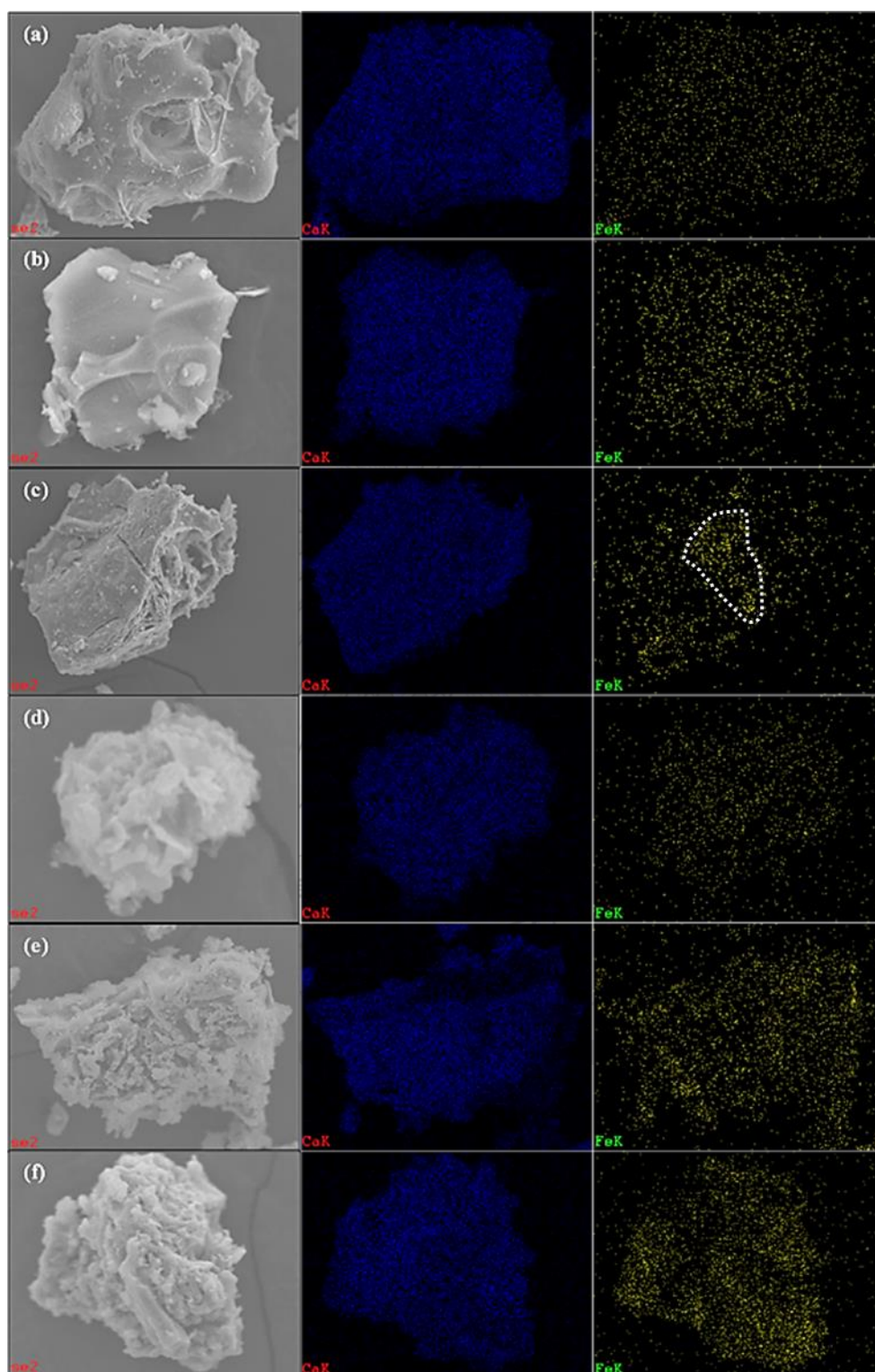
Figure 26 SEM-EDX of calcium and iron composition in freshly prepared Fe_2O_3/CaO-Al_2O_3 multifunctional catalysts: (a) 5FeCaAl, (b) 5Fe*CaAl, (c) Mec5Fe/CaAl, (d) Imp5Fe/CaAl, (e) Imp10Fe/CaAl and (f) Imp15Fe/CaAl.

The distribution of calcium and iron on Fe-based multifunctional catalysts were analyzed by SEM-EDX as shown in Figure 26. The elemental Ca map indicated that all samples had uniform dispersion of calcium. For the Fe, the samples containing 5 wt% Fe showed well dispersed on the surface for both synthesized from sol-gel (Figures 26(a) and (b)) and impregnation methods (Figure 26(d)) while that prepared by the mechanical mixing route showed partial densification as indicated within the dashed line in Figure 26(c). With increasing %Fe loading, Imp10Fe/CaAl and Imp15Fe/CaAl, Fe rich on the surface of $CaO-Al_2O_3$ sorbent caused the amount of irregular structures increased according to SEM images. Furthermore, an increase in EDX signal intensity of Fe at 15 wt% Fe loading in Figure 26(f) also suggested particle agglomeration. The elemental compositions and contents of each catalyst from EDX analysis were summarized in Table 13. The $Fe_2O_3/CaO-Al_2O_3$ catalysts contain amount of Fe, Ca, Al and O elements comparable to pre-calculation value, indicating the success of the synthesis.

Table 13 Energy dispersive X-ray analysis (EDX) of Fe-based multifunctional catalysts.

Element (wt%)	5FeCaAl	5Fe*CaAl	Mec5Fe/CaAl	Imp5Fe/CaAl	Imp10Fe/CaAl	Imp15Fe/CaAl
Fe	5.21	4.82	5.96	5.47	10.76	15.04
Ca	37.65	36.61	40.75	37.4	34.36	30.32
Al	13.15	18.93	17.35	16.45	21.36	14.68
O	43.99	39.63	35.94	40.69	33.52	39.96

6.2 H$_2$ production

The developed catalysts were tested their performances on H$_2$ production via SECLR process of ethanol as shown by breakthrough curve of gaseous products obtained from fuel reactor presented in Figure 27.
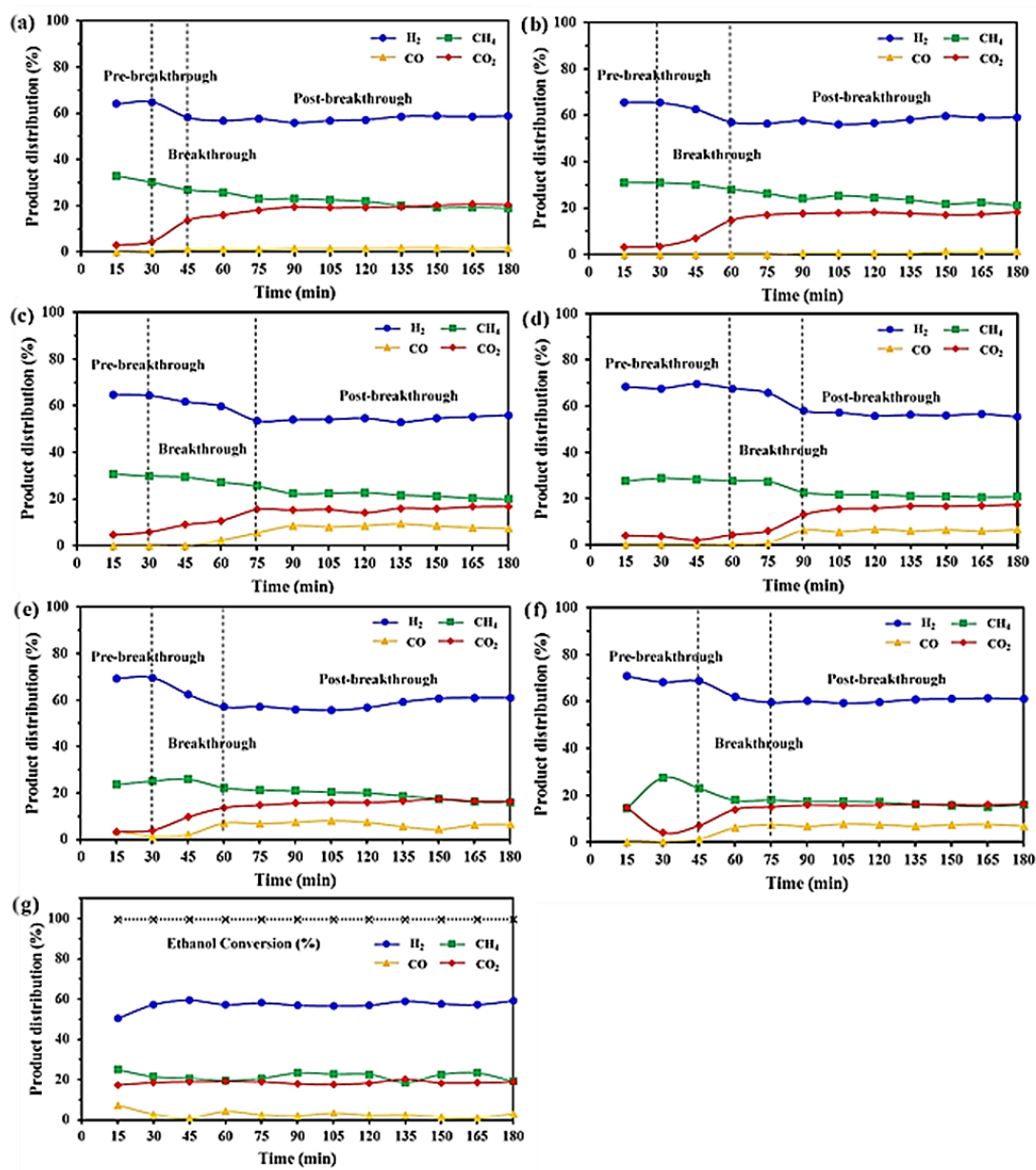
Figure 27 Product distribution (%) from the SECLR process of ethanol; (a) 5FeCaAl, (b) 5Fe*CaAl, (c) Mec5Fe/CaAl, (d) Imp5Fe/CaAl , (e) Imp10Fe/CaAl, (f) Imp15Fe/CaAl and (g) 5Fe/Al

The 5Fe/Al sample was selected as based catalyst to investigate the effect of adding CaO for sorption enhanced H_2 production. The results in Figure 27(g) showed that ethanol conversion of 99.6% could be obtained with the production of 57.7% H_2 purity. Lower H_2 production of 51% observed in the first 30 min was due to a portion of ethanol was oxidized with iron oxide and yielded CO (Eqs. 2.20 and 2.21). In case of applying multifunctional catalyst to the process, the composition profiles of gaseous products could be divided into three sections: pre-breakthrough, breakthrough and post-breakthrough as shown in Figures 27(a)-(f). Greater H_2 production observed in the pre-breakthrough period showed the effect of adding CaO as CO_2 adsorbent as the value was over its equilibrium production shown in the post-breakthrough period. Catalysts prepared by the sol-gel method (Figures 27(a) and (b)) demonstrated a similar H_2 purity of about 65% in the pre-breakthrough period for 30 min for either the Fe precursor was added before (5FeCaAl) or after peptization (5Fe*CaAl). The maximum H_2 production and the lowest CO_2 concentration were obtained in the pre-breakthrough period, as CaO sorbent immediately absorbed the produced CO_2 from the reaction, promoting WGS reaction and thus high conversion of CO. When a significant portion of the CaO sorbent absorbed CO_2 and formed $CaCO_3$ (Eq. 2.12), H_2 concentration at the outlet gradually decreased, while the CO_2, CO and CH_4 concentration increased. This period is called breakthrough period. In this period, the 5Fe*CaAl sample showed a longer breakthrough period of 30 min while that of the 5FeCaAl sample was only 15 min. This is plausibly because the former possessed higher surface area and pore volume as shown in Table 12. Once the CaO sorbent was saturated, the concentration of H_2, CO_2, CO and CH_4 reached steady state values in the post-breakthrough period. The

act of iron as active metal promoted the breaking of the C-H bonds, leading to lower CH_4 selectivity and increasing selectivity of CO_2 at the same time [104]. The H_2 purity in the post-breakthrough period of both samples prepared by sol-gel route was 58%.

For the catalyst synthesized by mechanical mixing, Mec5Fe/CaAl, (Figure 27(c)), pre-breakthrough period of 30 min with 64.8 % H_2 purity was obtained. The longest breakthrough period of 45 min was observed with this catalyst. This could be explained by the presence of the lowest amount of Ca_2Fe_2O5 phase, which could block pores of the CaO sorbent, as shown in XRD result of fresh catalyst depleted in Figure 23. Furthermore, this catalyst possessed the highest average pore size (Table 12) as the larger pore size was less susceptible to pore blockage [105]. At the post-breakthrough period, 55% H_2 purity was observed in this catalyst.

The catalysts prepared by impregnation (Figures 27(d), (e) and (f)) offered the highest H_2 purities of 70% in the pre-breakthrough period regardless of Fe content. In addition, it was found the shorter breakthrough time of 30 and 45 min for the Imp10Fe/CaAl and the Imp15Fe/CaAl catalysts, compared to the Imp5Fe/CaAl. This is possibly due to faster CaO deactivation as more defect in catalytic structure of both Imp10Fe/CaAl and Imp15Fe/CaAl catalysts, i.e. higher crystallite sizes and poorer textural properties (Table 12), were found. The longest pre-breakthrough period of 60 min was obtained with the Imp5Fe/CaAl as shown in Figure 27(d), indicating higher stability of CaO and CO_2 capture capacity because the presence of both $Ca_{12}Al_{14}O_{33}$ inert support and $Ca_2Fe_2O_5$ phase could prevent the sintering of CaO, increasing diffusion resistance of CO_2 through the $CaCO_3$ layer.
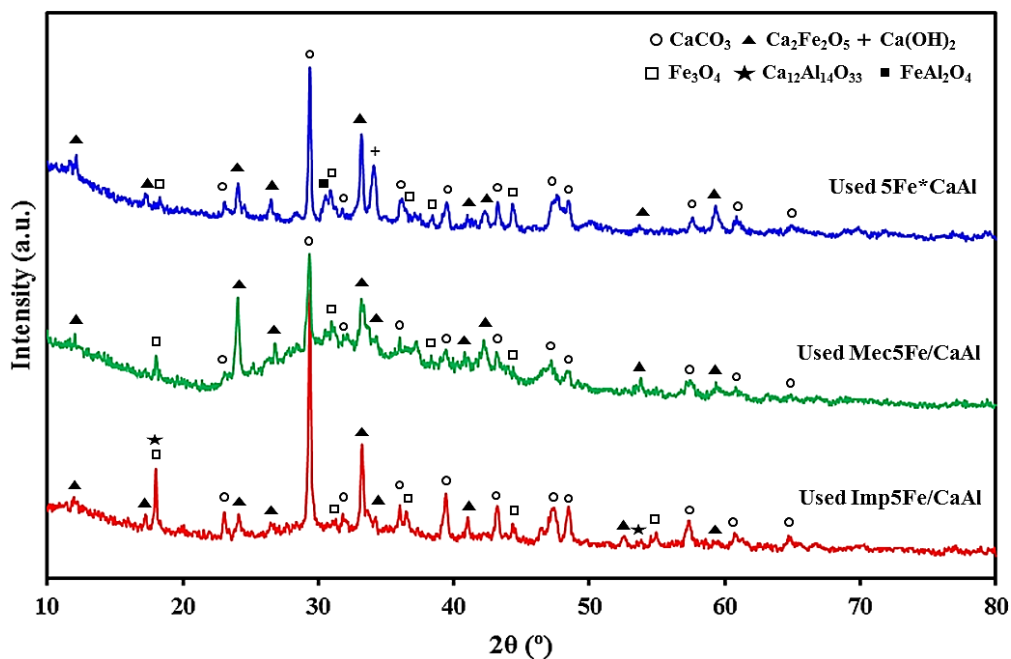
Figure 28 XRD patterns of the used $Fe_2O_3/CaO-Al_2O_3$ multifunctional catalysts prepared with different synthesis methods (sol-gel, mechanical mixing and impregnation) of 5 wt % iron content after H_2 production.

Figure 28 shows the XRD patterns of the used Imp5Fe/CaAl materials after 1 cycle running, compared with other preparation methods containing 5 wt% iron. As seen, the impregnation route exhibited the highest $CaCO_3$ peak intensity implying the largest amount of CO_2 sorption capacity with the presence of $Ca_{12}Al_{14}O_{33}$ inert support and $Ca_2Fe_2O_5$ phase. Furthermore, remaining the same peaks of $Ca_2Fe_2O_5$ phase was observed after the reaction. This suggested that the presence of $Ca_{12}Al_{14}O_{33}$ phase in this material could stabilize $Ca_2Fe_2O_5$ plausibly because of strong intercomponent interactions and the high temperatures of fusion of the two phases [106]. As the sol-gel and mechanical mixing methods showed lower breakthrough time of 30 min, this suggested the rapid deactivation by agglomeration during the test leading to lower CO_2 sorption capacity which confirmed by the lower intensity of

$CaCO_3$ peak. Moreover, the loss of $Ca_{12}Al_{14}O_{33}$ inert support phase and very small amount of $Ca_2Fe_2O_5$ in Mec5Fe/CaAl caused lower catalytic performance and more deactivation as shown by broadening line of XRD pattern. In addition, the minor peaks of Fe_3O_4 were observed in all used multifunctional catalysts and confirmed the presence of Fe_2O_3 in the material before the reactions which was completely transformed during the catalytic test. Noted that peaks of intermediate FeO and Fe^0 phases were always absent after the reactions. For the result in post-breakthrough period, 58% of H_2 purity were obtained in Imp5Fe/CaAl and Imp10Fe/CaAl catalysts. While, Imp15Fe/CaAl provided 60% of H_2 purity due to the largest content of iron active site. It was observed that similar H_2 purity in this period of the samples with 5 wt % Fe content prepared by the sol-gel and impregnation was found. Whereas, the lowest amount of 55% was observed in Mec5Fe/CaAl catalyst. This is attributed to the loss of surface Fe active sites by particle agglomeration confirmed by SEM-EDX result of the used catalysts which was shown in Figure 29. From SEM images and element Fe distribution, it was found that particle agglomeration and strongly Fe densification were observed with the used catalyst prepared by the mechanical mixing method (Figures 29(c) and (d)). While the material synthesized by the sol-gel and impregnation routes showed only partial sintering and the dispersion of element Fe were almost consistent with the fresh catalyst. Moreover, it is worth noting that sol-gel method is beneficial for WGS reaction as the lowest CO concentration was obtained at any time as shown in Figures 27(a) and (b). This is correlated with the uniform surface of the catalyst prepared from sol-gel route to facilitate the easier gas diffusion, which could be observed in the SEM images depicted in Figs. 4 and 8 [107].
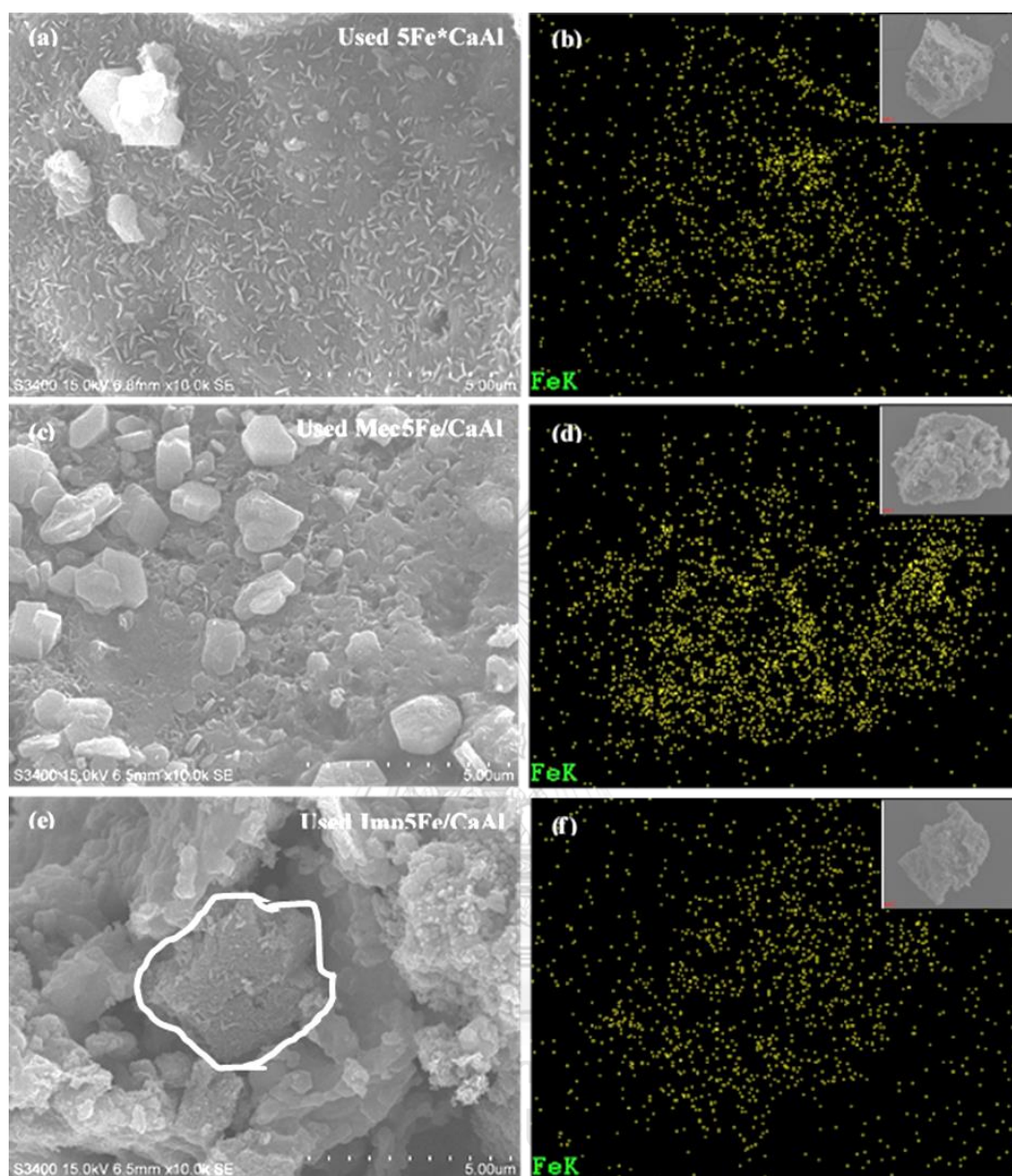
Figure 29 SEM micrograph (right) with elemental Fe map from EDX (left) of the used Fe_2O_3/CaO-Al_2O_3 multifunctional catalysts after reaction test: (a),(b) 5Fe*CaAl, (c),(d) Mec5Fe/CaAl and (e),(f) Imp5Fe/CaAl (after 1 cycle)

Furthermore, the lowest CO concentration of 5Fe*CaAl sample results in the smallest amount of carbon deposition compared to the other methods which was characterized by DSC-TGA techniques after reaction test.
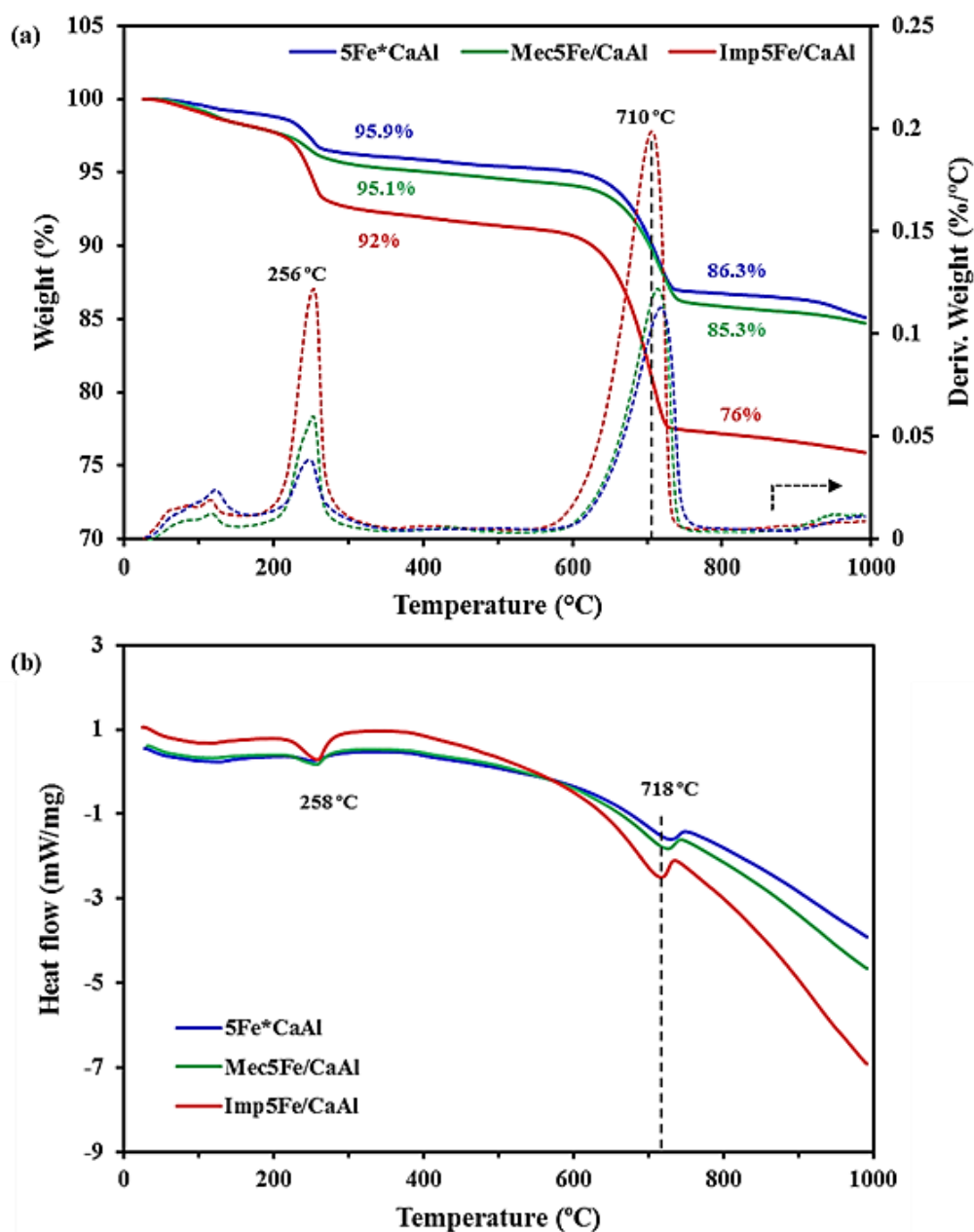
Figure 30 (a) TGA and (b) DSC profiles of the used Fe_2O_3/CaO-Al_2O_3 multifunctional catalysts after H_2 production in air.

As exhibited in Figure 30(a), the first period of mass loss in TGA curve was from 60 °C and reached a maximum mass loss around 108 °C, resulting from the elimination of physically absorbed water. The second period of mass loss started decreasing from 200 °C and reached unchanged at 350 °C due to easily oxidized amorphous carbon originated from CO disproportionation or Boudouard reaction (Eq. 2.11), consistent with peak of DTG centered at 256 °C [108]. In this period, the smallest amount of weight loss 4.1% for used 5Fe*CaAl catalyst was obtained. While the amount of weight loss 4.9% was observed for used Mec5Fe/CaAl, which was quite low when compared to weight loss of 8% for used Imp5Fe/CaAl catalysts indicating less coke deposition on catalytic surface. This is also resulted from reduction of the iron surface to catalyze the CO disproportionation reaction leading to a decrease in the rate of carbon formation [109]. From the DSC results of used catalysts shown in Figure 30(b), according to Nogueria *et al.* (2014) [110], the peak at 220 to 350 °C was attributed to the oxidation of carbonaceous species with low ordered structure like amorphous carbon type, which was clearly observed in Imp5Fe/CaAl centered at 258 °C. The small carbon formation amount of 5Fe*CaAl and Mec5Fe/CaAl makes the heat release at different temperature ranges difficult to be distinguished, so the thermal information could not be observed in their DSC profiles.

Then, the last mass loss was observed between 600 to 800 °C which was assigned to the decomposition of $CaCO_3$ to CaO relating to the CO_2 sorption capacity [93]. In this temperature range, the maximum weight loss of 16% observed with the used Imp5Fe/CaAl compared with 9.6 and 9.8% of 5Fe*CaAl and Mec5Fe/CaAl, respectively. This result confirmed the largest CO_2 capture capacity of Imp5Fe/CaAl

which is evidenced for the longest breakthrough time as shown in Figure 27(d). It should be noted that no mass gain was observed since the iron loading (5 wt %) was relatively low. Additionally, the mass loss in this period was coincided with the peaks of DTG and DSC curves at the temperature region of 700-750 °C which observed the shifted towards highest temperature for 5Fe*CaAl sample prepared by sol-gel method implying the most difficult for CO_2 removal. While Imp5Fe/CaAl catalyst provided the easiest to be eliminated CO_2. Therefore, 5 weight percent loading of Fe on CaO-Al_2O_3 sorbent synthesized with impregnation method was the best conditions for combination of iron-based oxygen carrier and calcium-alumina based sorbent intended for SECLR of ethanol.

6.3 Reusability of multifunctional catalyst

We studied next the capability of spent iron-based oxygen carrier after reaction test in fuel reactor to be oxidized by reacting with steam (Eqs 2.28-2.30) and followed by oxygen (Eq. 2.31). The further steam oxidation of reduced iron is not only evaluate the stability of oxygen carrier, but it also more produce high-purity H_2 from water splitting (WS) reaction. It was found that the H_2 gas evolved over iron-based oxygen carrier under studied condition at temperature of 500°C and steam flow rate of 0.05 ml min^{-1} lasted for 60 min as shown in Figure 31.
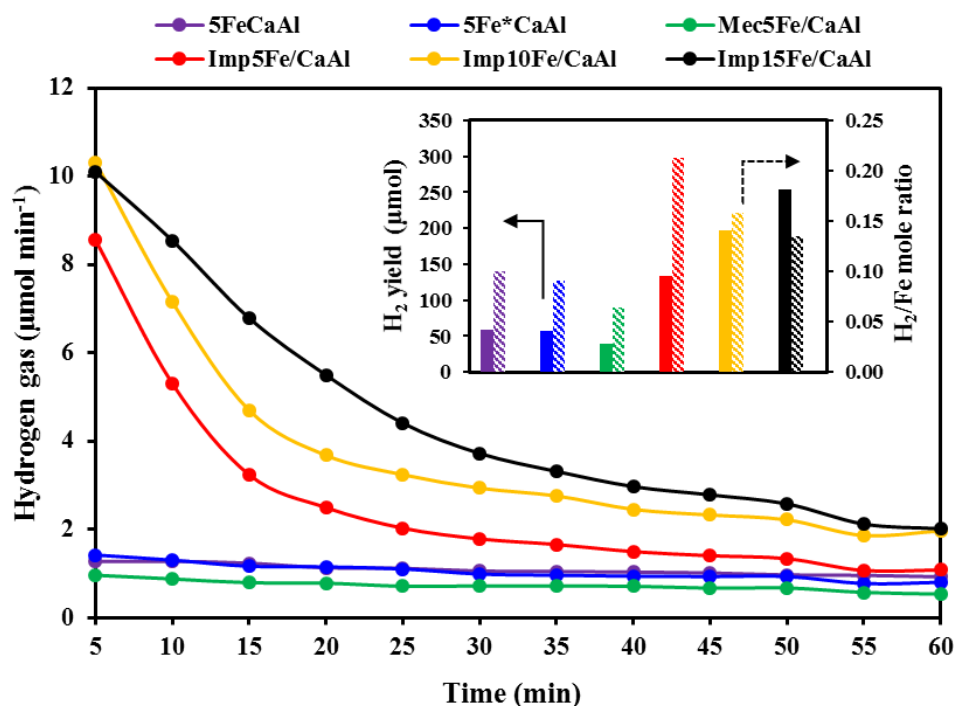
Figure 31 Evolution of H_2 from water splitting (WS) after SECLR of the used $Fe_2O_3/CaO-Al_2O_3$ multifunctional catalysts prepared through different routes.

This indicated that the catalyst was not complete redox reaction in fuel reactor and further reduction of FeO and/or Fe was observed resulting in the H_2 production. Moreover, the catalysts prepared through different methods yielded significantly different hydrogen productivity and iron content greatly affected the hydrogen amount in the steam oxidation. The samples prepared by impregnation method showed higher activity for water splitting confirming the retarding catalyst sintering by the presence of $Ca_{12}Al_{14}O_{33}$ and $Ca_2Fe_2O_5$ phase. The H_2 yield from WS was determined by following equation and shown in the insert map in Figure 31.

$$H_2 \text{ yield (μmol)} = \int_0^t \left(\dot{n}_{out} \times C_{H_2} \right) dt \tag{6.1}$$

where $\dot{n}_{out}$ and C_{H2} are the mole flow rate and concentration of H_2.

As expected, it is also evident that the H_2 yield increased along with the iron content, which is a result of oxidation reaction. The highest H_2 yield of 254 μmol was

obtained from Imp15Fe/CaAl. However, the H_2 yield of all prepared catalysts still produced and maintained after running period of 60 min indicating that it takes a longer time for the complete oxidation by steam which is not similar to the bare Fe^0 as reported in previous literature [55]. This is implied that the properties of supported Fe^0 was different resulting in the better catalytic stability. To evaluate the oxygen carrier's performance, the stoichiometry ratio of generated H_2 to mole of Fe in oxygen carrier was calculated and compared with the result using pure Fe_2O_3 as oxygen carrier which was reduced with H_2 before steam oxidation reaction based on the work from Zhu et al [111]. According to the calculation, the stoichiometry ratio of H_2 and mole of Fe in their work was about 1.04:1 which is consistent with the theoretical ratio of 1:1 in Eq. 2.28 suggesting that this equation is the main reaction for the water splitting process. It can be seen that this value did not reach 1.33:1 of the overall reaction (Eq. 2.30) indicating the partial Fe^0 from reduction step could be re-oxidized to its oxidation state (Fe_3O_4) by steam. In this work, the maximum ratio of generated H_2 and mole of Fe as also shown in the insert map of Figure 31 was 0.21:1 for the used Imp5Fe/CaAl catalyst with 5 wt % of Fe content which is more difficult to re-oxidize. This performance showed reasonable and acceptable activities for water splitting into H_2 with other phases' formation from strong Fe-Ca interactions. Although the Imp15Fe/CaAl obtained the highest H_2 yield, the particle agglomeration as evidenced in Figure 29 caused the efficiency as H_2/Fe mole ratio lower than it should be.

From all the results, the Imp5Fe/CaAl catalyst offered the most favorable performance 70% of H_2 purity and a breakthrough time of 60 min with an appreciable amount of H_2 produced in the steam oxidation. Therefore, the

Imp5Fe/CaAl was chosen for stability test over 5 cycles by performing SECLR for H_2 production at reaction temperature of 600 °C and S/E of 4 and following steam oxidation for oxygen carrier's performance at temperature of 500 °C.
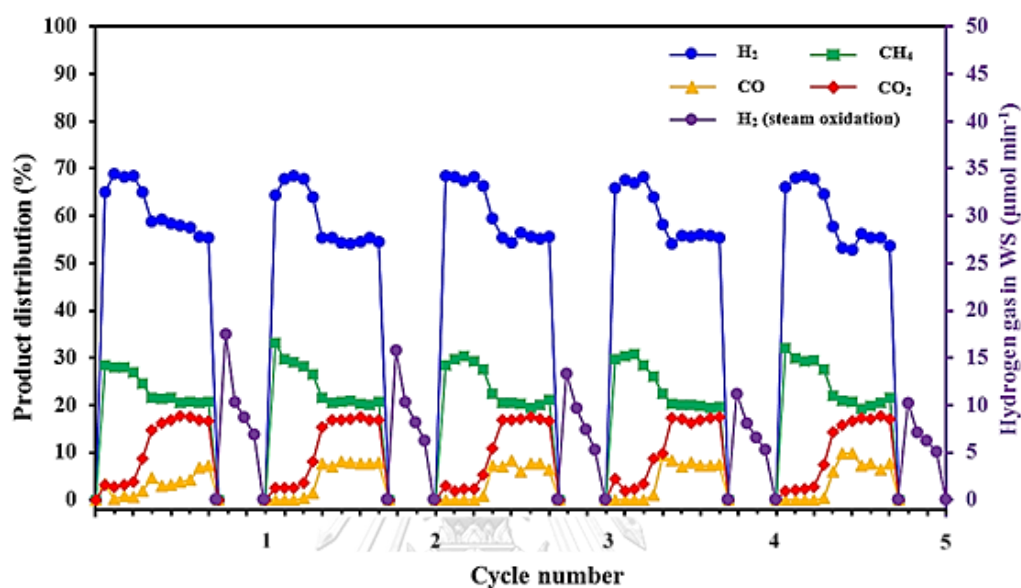
Figure 32 The stability of Imp5Fe/CaAl catalyst in SECLR from ethanol for H_2 production and in WS from steam oxidation for oxygen carrier evaluation from 5 consecutive cycles.

Figure 32 demonstrates that H_2 purity from SECLR could be maintained at ca. 70% in the pre-breakthrough period in the first 3 cycles. This could be attributed to the most stable sorption capacities of $CaO-Al_2O_3$ combined by impregnation method which presented in this multifunctional catalyst. Moreover, this catalyst also sustained a relatively stable yield of H_2 in WS test with ratio of generated H_2 to one mole of Fe in the range of 0.19-0.21 for the first 3 cycles indicating the stable oxygen carrier's performance. A slight reduction of H_2 production was observed in the subsequent 4th and 5th cycles of 66% and 67% for H_2 purity in SECLR and 0.15 and 0.14 for H_2/Fe mole ratio in WS. The latter should be ascribed to partial sintering

during the phase transformation ($Fe_2O_3 \rightarrow FeO/Fe^0 \leftrightarrow Fe_3O_4$) as higher peak intensity

of Fe_3O_4 phase in XRD pattern of after stability test was observed as shown in Figure

33, and the peak intensity of $Ca_2Fe_2O_5$ phases also slightly increased with the

formation of other phases from strong interaction between Fe-Ca. However, the

hydrogen amount drop for WS test in this work was 25% which is lower than the

result from Zhu *et al* [111] that dropped by 60%. This suggested that the presence

of other phases penetrating on CaO surface enhanced the stability of active iron.
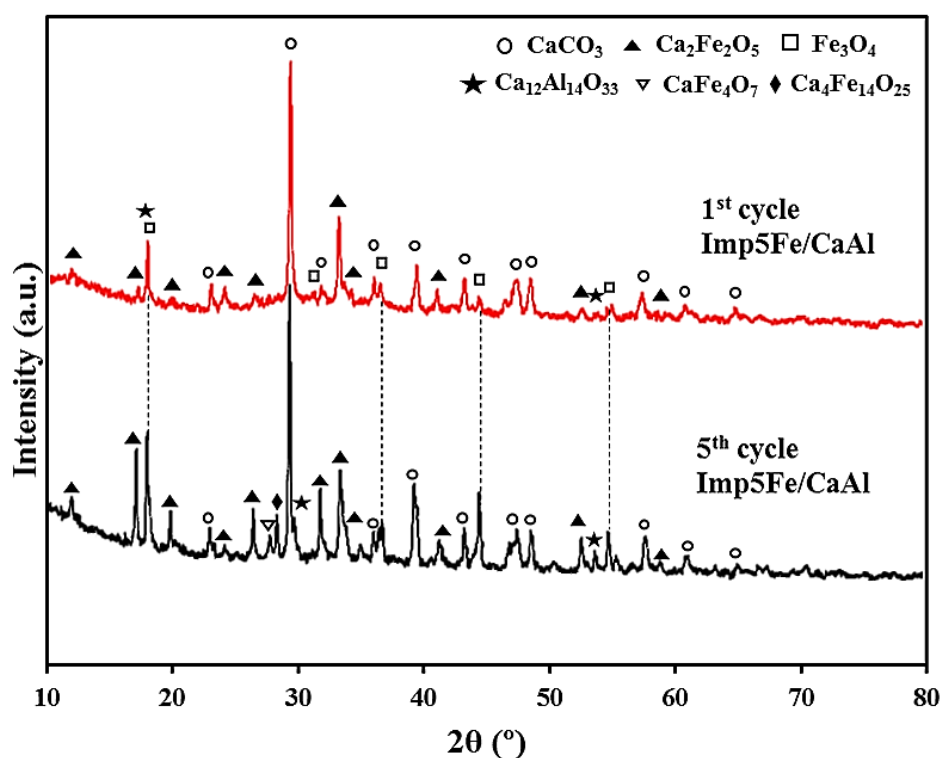
Nevertheless, this sample showed stable activity both for sorption capacity in SECLR

and oxygen carrier in WS over 5 oxidation-reduction cycles on stream.

Figure 33 XRD patterns of the used Imp5Fe/CaAl catalyst after 1st and 5th cycle.

CHAPTER VII

Activity and carbon resistance of NiFe-MgAl bifunctional catalyst derived from

Hydrotalcite-like precursors in chemical looping reforming of ethanol for

hydrogen production

As in the previous chapter, activity of the catalyst was found to be limited by the formation of $Ca_2Fe_2O_5$ phase due to the strong interactions between iron and calcium as higher its content was obtained after reaction test for H_2 production in multi-cyclic operation. The modification with other metal oxides like MgO was applied to improve the catalytic performance. Another promising approach to enhance the catalytic performance is the utilization of hydrotalcite-like compounds (HTlcs) as precursors for mixed oxide catalysts. Therefore, in this present work, the bi-functional catalysts of NiFe-MgAl were prepared from a hydrotalcite-structured precursor and tested for the H_2 production from chemical looping reforming of ethanol. Various analysis techniques are determined to find the relationship between catalytic structure and performance with respect to activity and stability. In addition, the influence of the bimetallic NiFe-MgAl for catalytic regenerability and understanding the role of Fe for the coke resistance were studied.

7.1 Catalytic performance in CLR

Figures 34(a)-(c) depict the product selectivity of CLR over three samples of HT-derived OCs under different temperatures of 400, 500, 600 and 700°C with *S/E* at a stoichiometry of 3. The duration of each temperature for conditions test in fuel

feed step was 30 min. The results found that ethanol was completely converted under all studied conditions. The highest purity of H_2 in all prepared catalysts was obtained at reaction temperature of 500°C. At this condition, the Fe-MgAl (Figure 34(a)) had a H_2 purity of 66.5% which is lower than the other two catalysts that have Ni sites. The NiFe-MgAl and Ni-MgAl (Figures 34(b) and (c)) indicated a similar H_2 purity of about 80 %. It demonstrates that the introduction of nickel improves the purity of hydrogen. This is due to the relatively stronger ability to break C-C and C-H bonds. When operated at low temperature 400°C, it shows an unsuitable condition of lower concentration of H_2 as steam reforming (Eq. 2.1) is an endothermic reaction which prefers high temperature. While at higher reaction temperatures of 600 and 700°C, it yields more byproducts especially CO as water gas shift (Eq. 1.3) is an exothermic reaction. Therefore, the optimum condition over all prepared HT-derived OCs for H_2 production in CLR process was at 500°C.

Moreover, the experiment at the optimum condition was further conducted by performing a longer period of time in fuel feed step approximately 14 h in order to investigate the stability of the catalyst. The H_2 concentration as a function of the time on stream (TOS) at 500 °C for Fe-MgAl, NiFe-MgAl and Ni-MgAl is shown in Figure 34(d). The values of H_2 concentration of the monometallic Ni-MgAl (black) and bimetallic NiFe-MgAl (red) catalysts show similar trend— H_2 purity rapidly increased at first and gradually decreased at a later time, indicating the presence of sintering and deactivation. As can be seen from the figure, after TOS exceeds 11 h, the H_2 purity of Ni-MgAl decreased more than NiFe-MgAl. This was plausibly due to the different coke deposition on catalytic surface which will be further explained the detail about this below. For the monometallic Fe-MgAl catalyst which represents in

blue color, the H_2 purity shows stable behavior during the stability test. This is implying that the presence of Fe can resist the carbon formation. Herein, the bimetallic of Ni-Fe catalyst not only improves the purity for H_2 production but also modifies the catalytic stability.
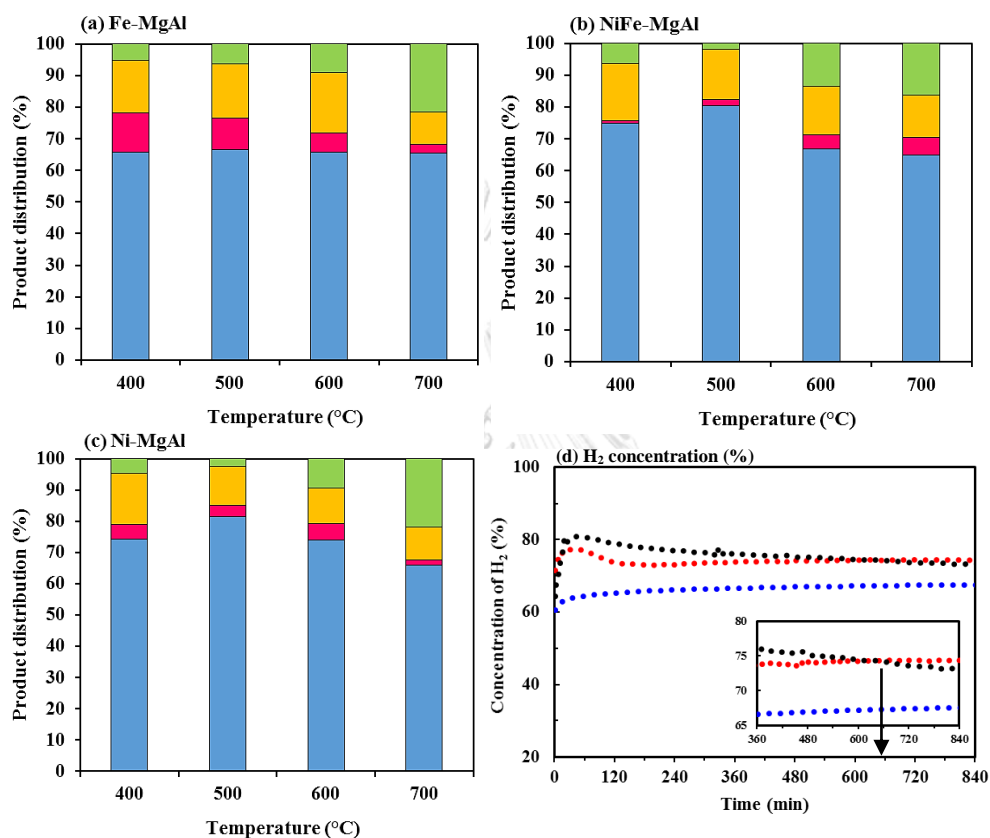
Figure 34 Product distribution (%) as a function of temperature for CLR process of the prepared oxygen carriers of (a) Fe-MgAl, (b) NiFe-MgAl and (c) Ni-MgAl and concentration of H_2 (%) as a function of reaction time (d) at 500 °C: S_{H2} (blue), S_{CH4} (pink), S_{CO2} (yellow), and S_{CO} (green).

7.2 Characterization of the bi-functional catalyst from hydrotalcite-like compounds

To find the relationship between structure and activity, the catalysts were analyzed by various characterization techniques. Figure 35 shows the XRD patterns of the as-synthesized precursors, calcined and used sample of Fe-MgAl, NiFe-MgAl, and Ni-MgAl. The layer spacing values of (003) and (110) reflections for dried precursors

and crystallite size based on (220) reflection for calcined and used catalyst calculated by Scherrer equation are summarized in Table 14.

From Figure 35(a) of the as-synthesized precursors, all XRD patterns showed the characteristic reflection peaks of $Mg_6Al_2CO_3(OH)_{16}\cdot 4H_2O$ hydrotalcite (JCPDS 41-1428) at 2θ = 11.27°, 22.7°, 34.36°, 38.94°, 46.36°, 60.02° and 61.52° which are attributed to (003), (006), (012), (015), (018), (110) and (113) planes, respectively. The d-spacing of the (003) reflection corresponds to the thickness of a brucite-like sheet and one interlayer. The d(003) values of Fe-MgAl precursor in Table 14 was well in line with 0.784 nm for the Mg_3Al-CO_3 hydrotalcite. While the other two catalysts modified with Ni were found the lower values. This is possibly due to the formation of other phases in the precursors as other sharp peaks apart from hydrotalcite were observed. On the other hand, the d-spacing of the (110) reflection is the average metal ion-metal ion distance inside the brucite-like sheet which depends on the ionic radius. For the Fe-MgAl precursor, the d(110) was calculated to be 0.1548 nm which is slightly higher than 0.1540 nm for the Mg_3Al-CO_3 hydrotalcite. This is due to the replacement of a part of Al^{3+} with larger Fe^{3+} cation in the hydrotalcite structure (0.064 nm for Fe^{3+} and 0.054 nm for Al^{3+} in octahedral coordination). For catalyst with Ni addition, the d(110) are smaller than 0.1540 nm indicating the incorporation of Ni^{2+} cations to form Ni-Fe-Mg-Al HTlcs because ionic radius of Ni^{2+} is smaller than Mg^{2+} (0.069 nm for Ni^{2+} and 0.072 nm for Mg^{2+} in octahedral coordination).

The XRD patterns of the samples after calcination at 800 °C are shown in Figure 35(b). The diffraction peaks of hydrotalcite completely disappeared and the structure transformed into a periclase [Mg(Ni,Fe)-O]-type structure (JCPDS 45-0946) at 2θ = 36.94°, 42.92°, 62.30°, 74.69° and 78.63° with a mixture of spinel phase. The

(220) reflection of the periclase structure is observed at $d_{Calcined}$-spacings in the range of 0.1326-0.1488 nm which was smaller than the values for MgO (d = 0.1489 nm) due to the presence of smaller cations into the periclase structure. After the reaction test in CLR for H_2 production, the XRD pattern of used catalyst in Figure 35(c) demonstrates the reflections of a periclase structure. For the monometallic catalysts of Fe-MgAl and Ni-MgAl, the diffraction peak of metal particles were detected. For the bimetallic catalyst of a NiFe-MgAl, the XRD pattern exhibits a formation of Ni-Fe alloys. To examine the dispersion and morphology of the Ni-Fe alloy, TEM was employed and it was confirmed that the Ni-Fe alloys were well dispersed and the particle sizes were in the range of 0.018-0.027 μm as shown in Figure 35(d).
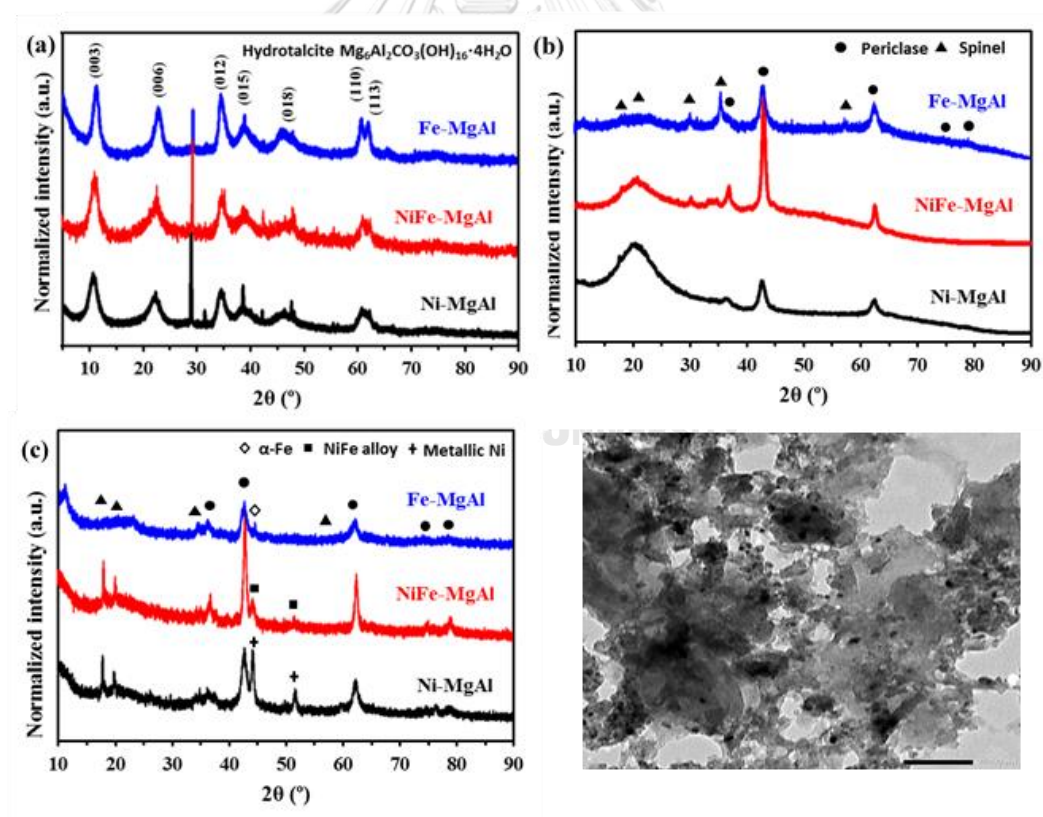
Figure 35 XRD patterns of the samples (a) as-synthesized, (b) after calcination (c) after reaction; TEM image of the used NiFe-MgAl sample (d) after activity test.

Table 14 Summary of XRD analyses for the as-synthesized, calcined and used catalysts.

Catalyst	d spacing (nm)		Crystallite size of calcined catalysts (nm)	Crystallite size of used catalysts (nm)
	d(003)	d(110)		
Fe-MgAl	0.7804	0.1549	0.1488	0.1547
NiFe-MgAl	0.7460	0.1536	0.1485	0.1537
Ni-MgAl	0.7258	0.1534	0.1326	0.1548

The compositions measured by ICP-OES are given in Table 15. The result of metal loading of calcined samples ranges from 9.2 to 9.4 wt %, which indicates that the metal is well loaded. The results of specific surface areas and pore volumes analyzed from the N_2 adsorption/desorption are also presented in Table 15. Higher surface area was obtained in the calcined hydrotalcites sample. The four precursors of Ni-Fe-Mg-Al in bimetallic catalyst prepared by co-precipitation method provide lower surface area than monometallic catalyst. This might be caused by more cations for substitution in the brucite-like layers leading to the decreasing of BET surface area and pore volume. Moreover, the N_2 adsorption/desorption isotherms for all the samples displayed type IV isotherms with hysteresis loops typically for the ordered mesoporous. As expected, the BET surface area and pore volume of used catalysts were decreased after reaction test due to the general sintering of agglomeration and carbon formation.

Table 15 Physicochemical property of the catalysts prepared from Hydrotalcite-like precursors

Catalyst	Metal loading (%)	BET surface area (m² g⁻¹)			Pore volume (cm³ g⁻¹)			Total desorbed CO$_2$ (mmol g⁻¹)
		HTlc	Calcined	Used	HTlc	Calcined	Used	
Fe-MgAl	9.2	28	63.3	58.5	0.07	0.16	0.09	0.233
NiFe-MgAl	9.3	21.4	33.8	29.9	0.05	0.07	0.05	0.155
Ni-MgAl	9.4	27.7	69.9	62	0.03	0.16	0.09	0.066

Temperature programmed reduction (TPR) measurements were performed for all calcined samples and Figure 36 summarizes the results. Two reduction peaks were observed for the Fe-MgAl sample. The first broad peak can be divided to the transformation of Fe_2O_3 to Fe_3O_4 at ca. 484 °C and further reduction of Fe_3O_4 to FeO intermediate at a starting temperature of 500 °C with the maximum reduction peak at ca. 556 °C [111]. The last reduction peak at ca. 726 °C was associated with the reduction to metallic Fe. The TPR profile of the NiFe-MgAl catalyst exhibited the main reduction peak at ca. 885 °C which shifted to higher temperatures due to the strong interaction of the components inside the Mg(Ni, Fe, Al)O structure. For Ni-MgAl, the TPR showed a profile of the reduction of NiO to metallic Ni in the periclase structure with a main peak at ca. 748 °C. Also a small peak can be observed at ca. 557 °C which could be attributed to reduction of NiO weakly interacting with support on the surface.
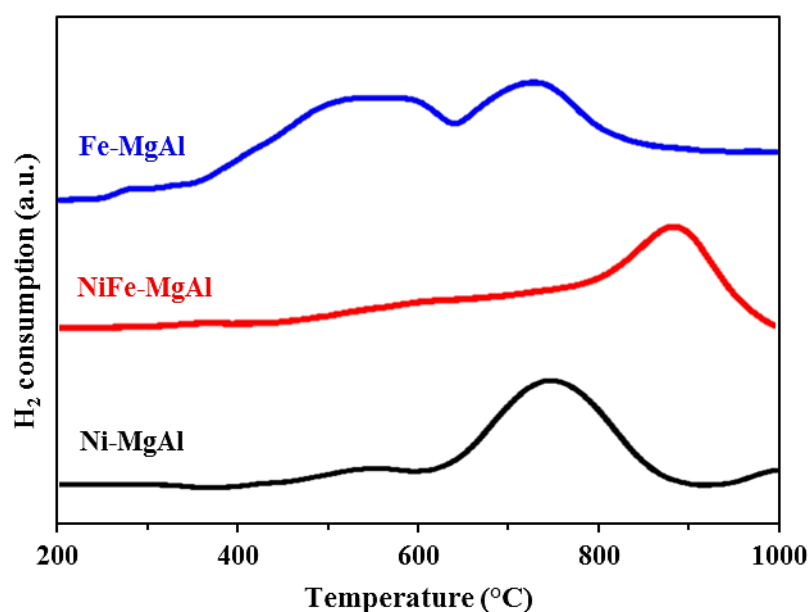
Figure 36 Temperature-programmed reduction profiles of the calcined samples

The origin of catalyst deactivation by coke deposition was also taken into account due to its importance for process efficiency especially in long-term performance. Coke deposition on the catalysts after stability test was characterized by performing O_2-TPO. Further structural information concerning the carbon deposited was obtained by scanning electron microscopy and Raman spectroscopy analyses of the spent catalysts.

Figure 37 gives the TPO profiles of used catalysts after carbon deposition. Different amounts of CO_2 are released during the TPO process, indicating the formation of different type of coke. The TPO results of the monometallic Fe-MgAl show a single peak around 415 °C corresponding to the amorphous coke (temperature <450 °C). This type of coke is identified to encapsulate on active metal sites and have a great impact on deactivation as it is able to condense and form the graphitic structure which can detect CO_2 peak at high temperature (∼700 °C). The TPO profiles of the bimetallic NiFe-MgAl composes of two peaks which the second peak around 593 °C is attributed to the filamentous coke (>550 °C). This type of coke is structured in fibres and does not directly block the active metal sites resulting in this catalyst to be more stable (Figure 34(d)). While the monometallic Ni-MgAl reveals three peaks in TPO profile with the third peak of coke in more condensed and graphitic structure. This type of coke may be a blockage of active metal sites that causes severe deactivation which confirms the decreasing in catalytic stability after TOS exceeds 11 h. The CO_2-TPD results was also listed in Table 15 to measure the basicity of catalysts as higher basicity can suppress the coke formation. The Ni-MgAl showed the lowest total amount of desorbed CO_2 verifying the lower coke resistance compared to Fe-MgAl and NiFe-MgAl.
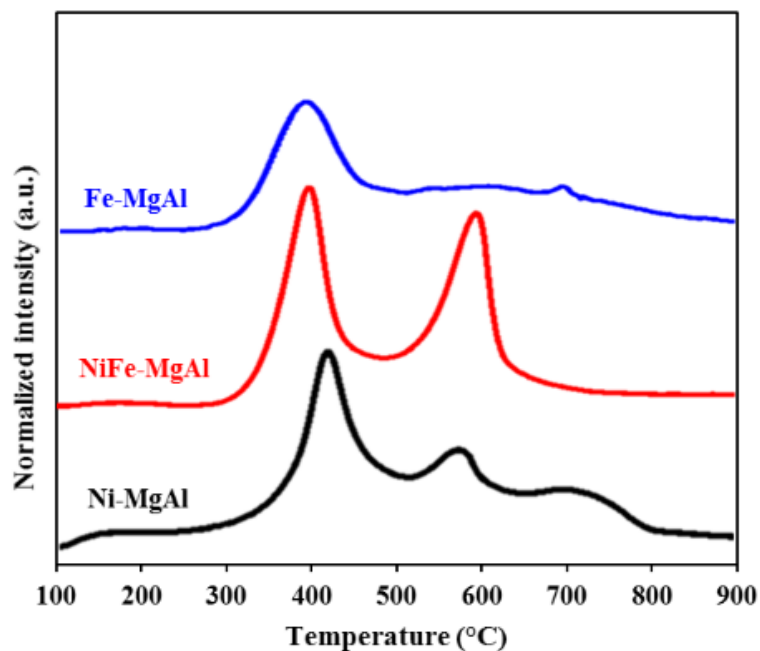
Figure 37 TPO profile of the different catalyst used for 14 h

The morphology of NiFe-MgAl sample before and after reactions was investigated by SEM, as illustrated in Figure 38. It can be significantly observed that the external morphology of catalyst changed after reaction at 500 °C. The fresh oxide catalyst in Figure 38(a) shows an irregularly granular structure and the particle size is mainly distributed in 0.01-0.16 μm with an average size of 0.03 μm. After reaction for 14 h, some particles were agglomerated into the large size and the deposited carbon is observed on the catalytic surface in Figure 38(b) which is identified as filamentous carbon, corresponding to the TPO results.
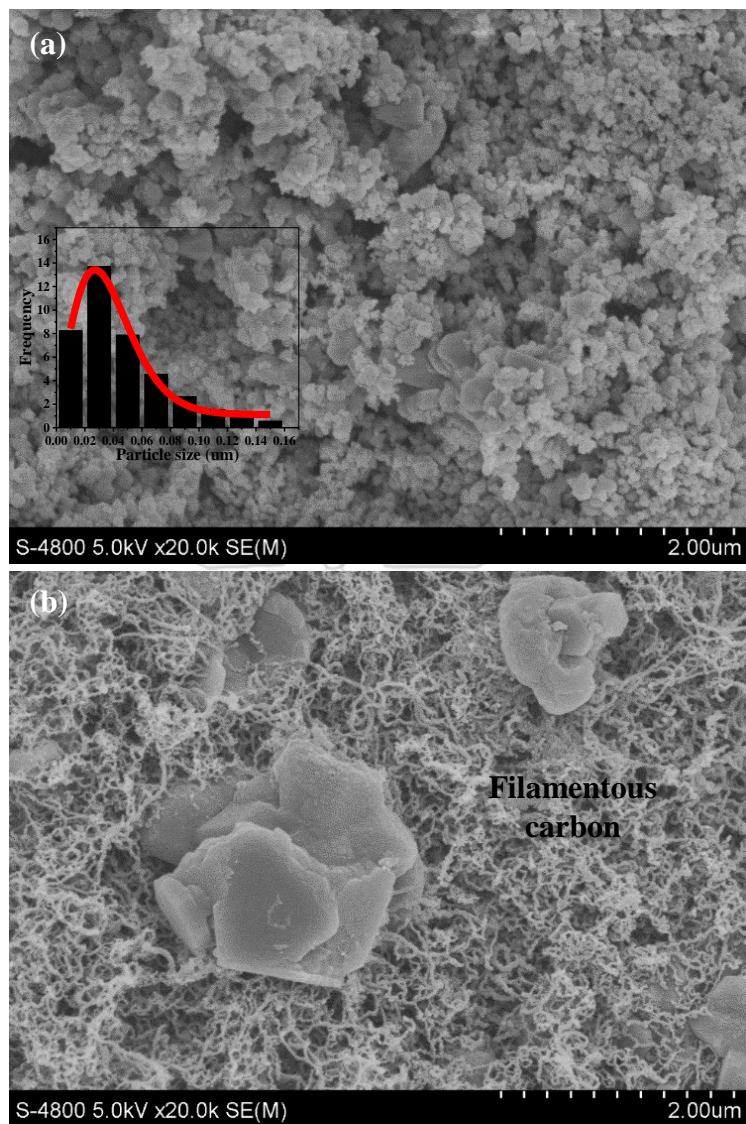
Figure 38 SEM Images of bimetallic NiFe-MgAl catalyst, (a) fresh and (b) after 500°C reaction

The Raman spectroscopy is a suitable technique for studying nature and characteristics of carbon deposits. Figure 39(a) shows the Raman spectra of used samples in the range of 1000-1800 cm^{-1} which are fitted into four characteristic bands. Generally, two intense bands of D and G bands are displayed at 1350 cm^{-1} and 1580 cm^{-1}, respectively. The D band is attributed to structural imperfections of graphite that indicates the presence of amorphous carbon and multilayer carbon

tubes. Another two bands located at ～1200 ℃ and 1550 ℃ are the components of D band. The first band is associated to bond vibrations in disordered graphitic layers which appears when the materials is very poor organization. The latter is also corresponded to amorphous coke due to bond vibrations near the edges in highly disordered graphitic layers [112]. The wide and large peak of D band was obtained in all samples indicating the predomination of disordered structures like amorphous carbon and filamentous carbon. The relative intensity of D to G band (I_D/I_G) can be used to describe the degree of crystallinity of deposited carbon on the catalysts. Figure 39(b) shows that the higher I_D/I_G ratio obtained in the Fe-based bifunctional catalyst (Fe-MgAl and NiFe-MgAl) which suggests a lower degree of coke crystal structures leading to the decreasing of oxidation temperature for carbon removal.
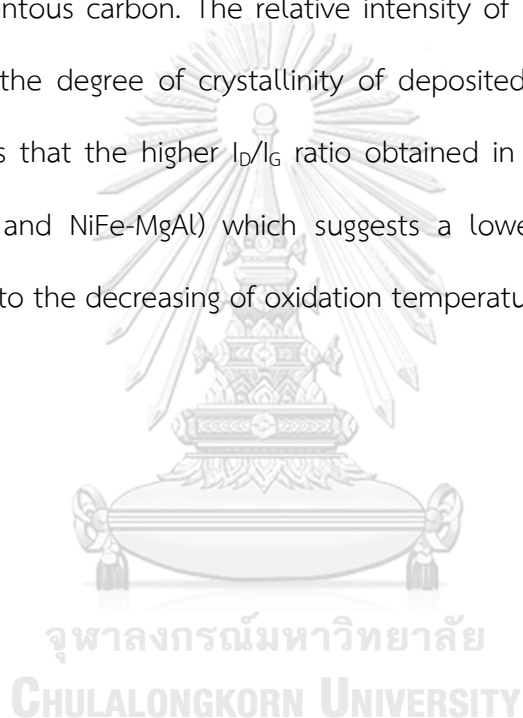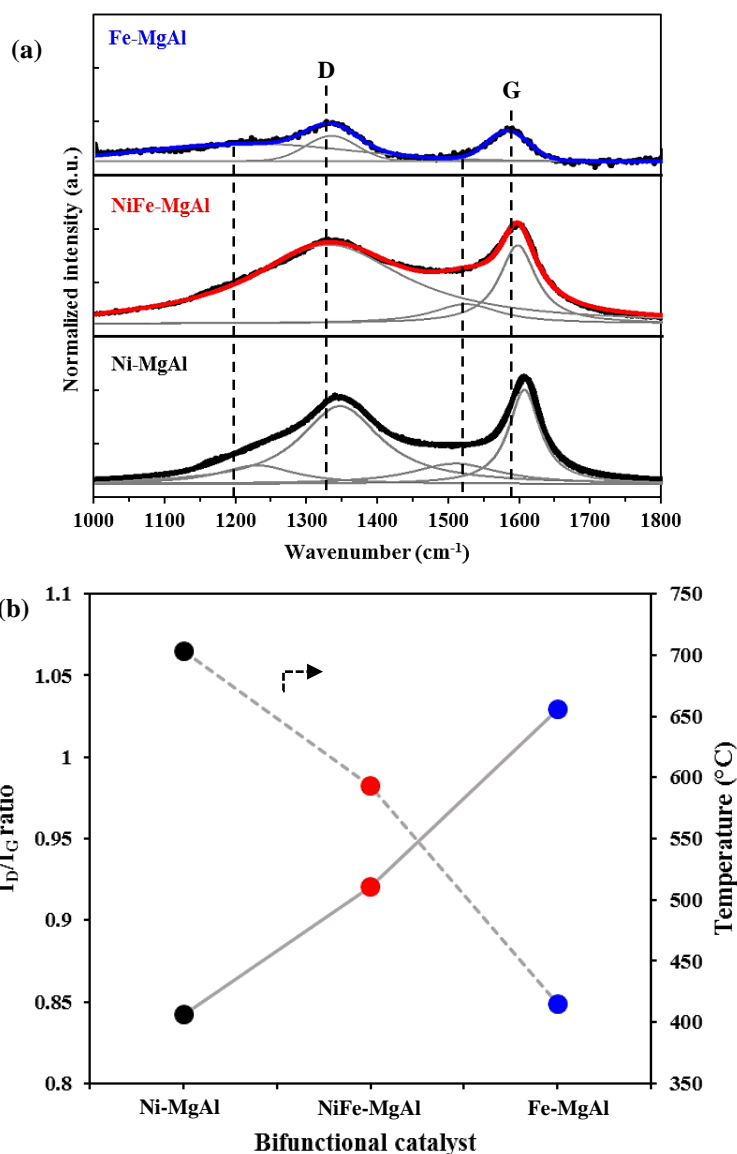
Figure 39 (a) Raman spectra fitting results of all catalysts after the carbon deposition (b) Ratio of D- and G-band intensities (I_D/I_G) and the temperature for coke removal

7.3 Catalytic performance of bimetallic NiFe-MgAl

From the above results, bimetallic NiFe-MgAl catalyst offered high H_2 selectivity of about 80 % owing to the ability of Ni added to break C-C and C-H bond and showed more stable behavior in long-term performance than monometallic catalyst due to the presence of Fe lead lower density of carbon deposition. To

investigate the role of Fe on carbon removal, the alternative pulse experiment was performed and monitored by MS. This experiment was focused on the oxidation with CO_2 for carbon removal. The use of CO_2 gas mainly involved the oxidation of only metallic Fe, while Ni is stable under this atmosphere. The result in the final step found that CO was produced on the NiFe-MgAl catalyst during the CO_2 pulse as shown in Figure 40, implying the reactions took place with Fe.
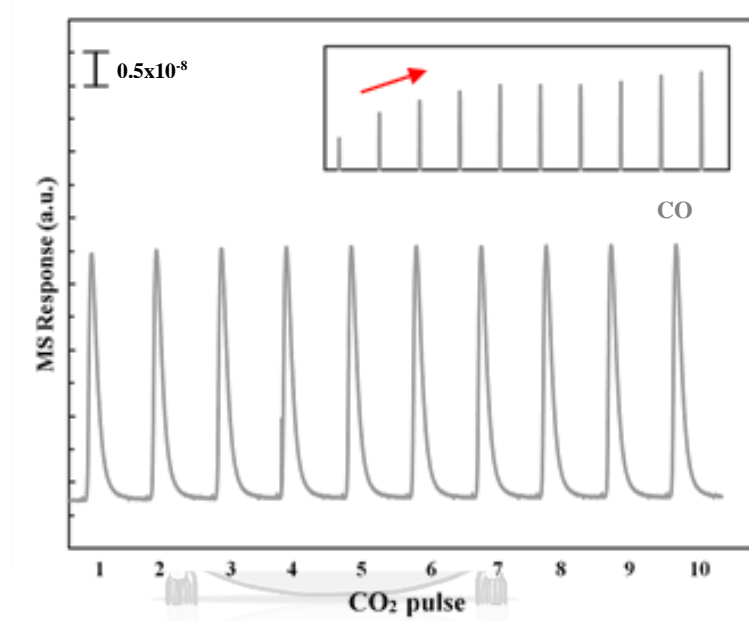
Figure 40 CO production during CO_2 pulse experiment over bimetallic NiFe-MgAl catalyst. Conditions: 1 mL s^{-1} of CO_2, 30 min.

To clarify the result, the surface chemical compositions and oxidation states of the Ni-Fe alloy particles in three samples at different conditions during pulse experiment including 1 CO_2 pulse, 5 CO_2 pulses and 10 CO_2 pulses were performed by XPS analysis. The deconvolution of XPS results are shown in Figure 41. The XPS spectra of the Fe 2p and Ni 2p are split into 2p$_{3/2}$ and 2p$_{1/2}$ doublets due to spin-orbit coupling. The Fe 2p spectra (Figure 7.8(a)) can be divided into five peaks, peak at ∼706 eV relating to Fe^0 species, peak at ∼709 eV attributing to Fe^{2+}, and the

peaks at ～711.4 eV and ～724 eV corresponding to Fe^{3+} with its satellite peak at ～718.6 eV. The surface compositions were calculated from the peaks area ratio of each element and the results are listed in Table 16. As can be seen in Table 16, the fraction of Fe^0 after 1 pulse of CO_2 was only about 2.7 % as it was reoxidized to higher valence states and the fractions of Fe^{3+} and Fe^{2+} were 67.3 % and 30.9 %, respectively. After 5 pulses of CO_2, the fraction of Fe^{2+} increased from 30.9 % to 33.1 % could be possible to the formation of FeO via the metallic Fe in alloy obtained lattice oxygen (O*) from CO_2 yielding CO (Eq. 7.1).

$$CO_2 + Fe \longrightarrow CO + FeO \qquad (7.1)$$

At the same time, the fraction of Fe^0 also increased to 5.1 % which can be explained by the FeO provides lattice oxygen to deposited carbon (Eq. 7.2) and oxidizing it leading to the more production of CO as shown in Figure 40, and the lower amount of Fe^{2+} was obtained after 10 pulses of CO_2.

$$FeO + C \longrightarrow CO + Fe \qquad (7.2)$$

For Ni 2p XPS spectra in Figure 41(b), the peaks at ～853.8 eV and ～871.2 eV were consistent to Ni^0, while the peaks at ～856 eV and ～873 eV were the feature of Ni^{2+} with its satellite peaks at ～861.5 eV and ～880 eV. The result from Table 16 revealed the remaining of metallic Ni composition during the pulse experiment as it cannot be oxidized by CO_2.
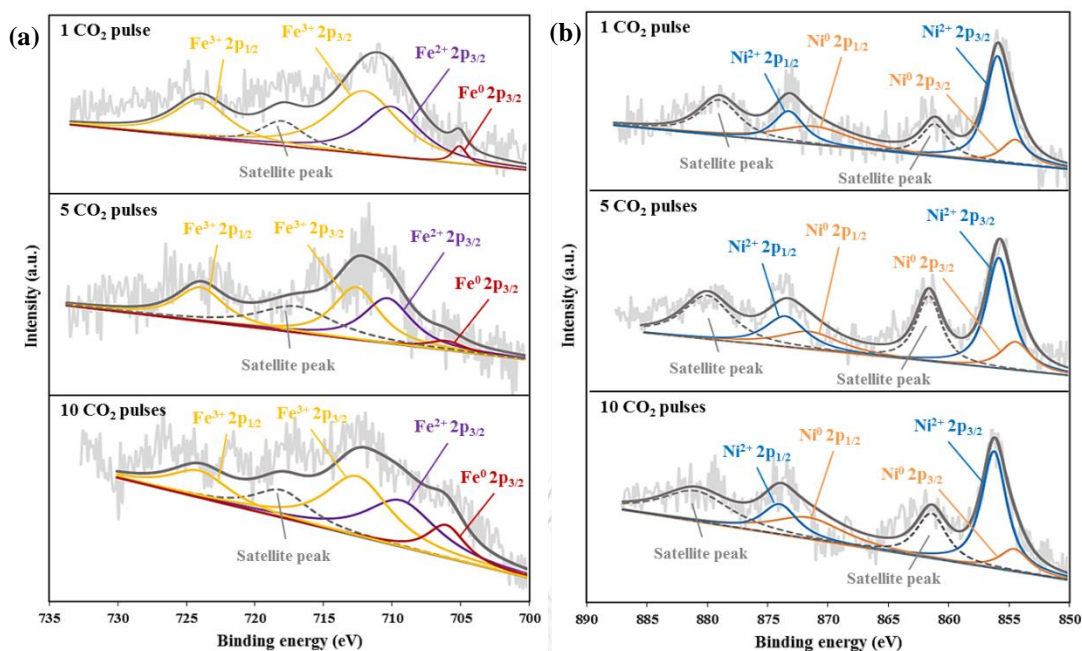
Figure 41 Surface chemical state evolution of the samples during CO_2 reduction process: (a) Fe 2p XPS spectra; (b) Ni 2p XPS spectra

Table 16 Element composition of XPS analysis under CO_2 pulse experiment of NiFe-MgAl catalyst

CO₂ pulse	Fe			Ni[b]	
	Fe³⁺	Fe²⁺	Fe⁰	Ni²⁺	Ni⁰
1	67.3	30.9	2.7	64.1	35.9
5	61.8	33.1	5.1	64.9	35.1
10	56.5	32.8	10.7	64.5	35.5

In order to obtain the direct information of the surface reaction and probe the evolution of intermediate species for carbon removal, *in situ* DRIFTS experiment under CLR was employed over NiFe-MgAl catalyst at 500 °C and the DRIFTS spectra as a function of TOS is shown in Figure 42 in the range between 780-1030 cm⁻¹. After exploring in the C_2H_5OH + H_2O mixture for 10 min, spectrum exhibits the weak bands

at 810, 890 and 1124 cm^{-1}, which are assigned to the Fe-O stretching mode suggesting the existence of FeO intermediate during the reaction. However, the intensity of these bands decreased after 20 min indicating the realloying of Fe. The particle was found to dealloy again after 30 min and lower intensities were obtained after an hour. According to the result, a graphical illustration of carbon species removal on catalytic surface of NiFe-MgAl is depicted in Figure 43.
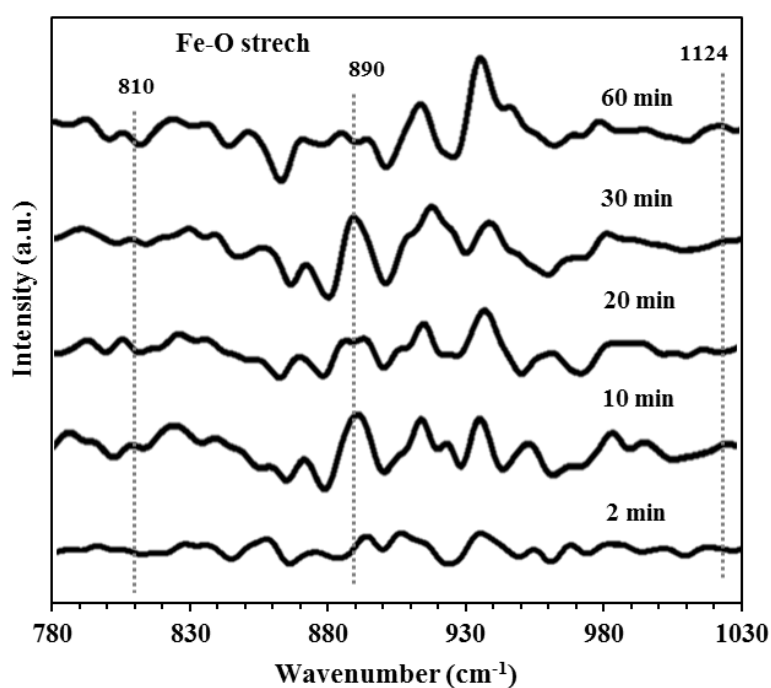
Figure 42 *In situ* DRIFTS spectra of NiFe-MgAl catalyst at 500°C under the reaction mixture containing ethanol and water (S/E ratio = 3) during an hour TOS.
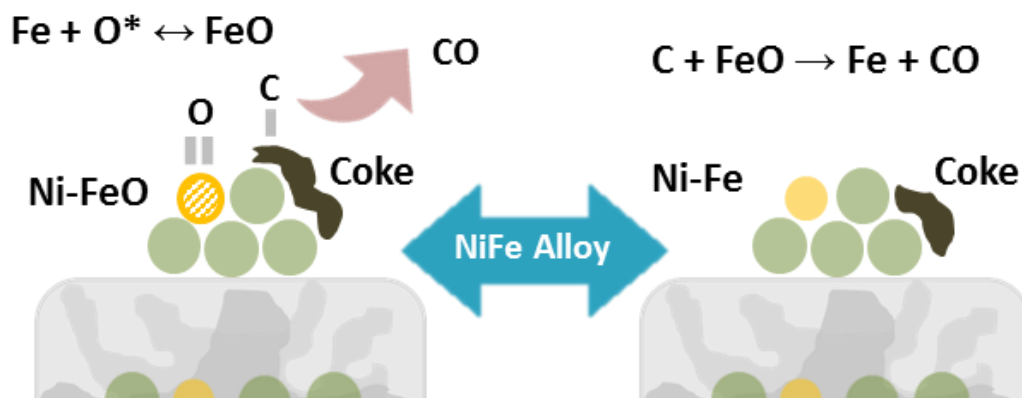
Figure 43 Schematic representation of carbon removal through the reduction of FeO
on the surface of NiFe-MgAl catalyst.

Moreover, it was necessary to study regenerability of catalyst as it is one of the most challenging problems for multicyclic operation in CLR process. Figure 44 demonstrates the product selectivity for catalytic regenerability of NiFe-MgAl over 10 consecutive cycles. After each cycle, the catalyst was regenerated by oxidation in air, followed by reaction test for 30 min. It can be seen from the result that H_2 selectivity can be maintained at ca. 80% indicating the complete recovery of bimetallic NiFe-MgAl catalyst.
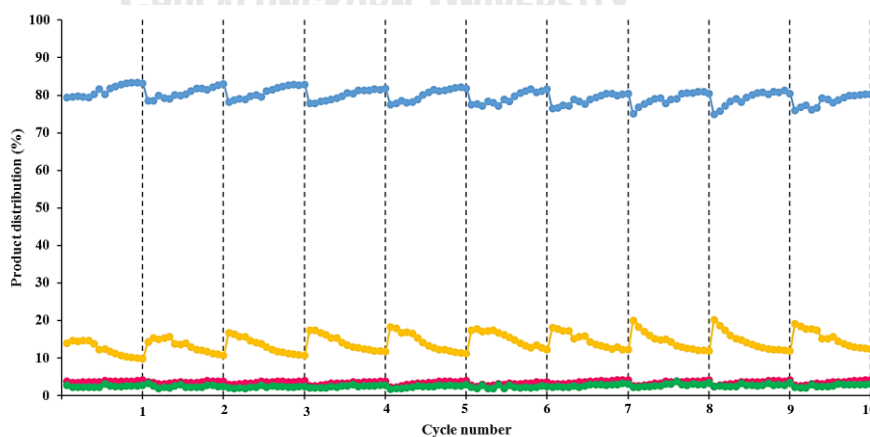
Figure 44 Product selectivity (%) on catalytic regenerability for CLR process over NiFe-MgAl at
500 °C: S_{H2} (blue), S_{CH4} (pink), S_{CO2} (yellow), and S_{CO} (green).

To gain an insight into the regenerability on the catalyst structure, the NiFe-MgAl catalyst after used at different cycles and after regeneration cycle were measured the structural changes by XRD. As shown in Figure 45, the catalyst after 1st regeneration shows the similar pattern with calcined catalyst. Moreover, after 2nd cycle, the (220) diffraction peak of alloy appeared at the same position with the 1st cycle and it disappeared after 2nd regeneration implying the both Ni^0 and Fe^0 were oxidized and incorporated into Mg(Ni, Fe,Al)O periclase. Similar pattern in structural changes were observed by repeating in multicyclic operation of CLR. Therefore, the catalytic regenerability of NiFe-MgAl is the result of alloy regeneration to resist the deactivation by agglomeration as well as carbon deposition.
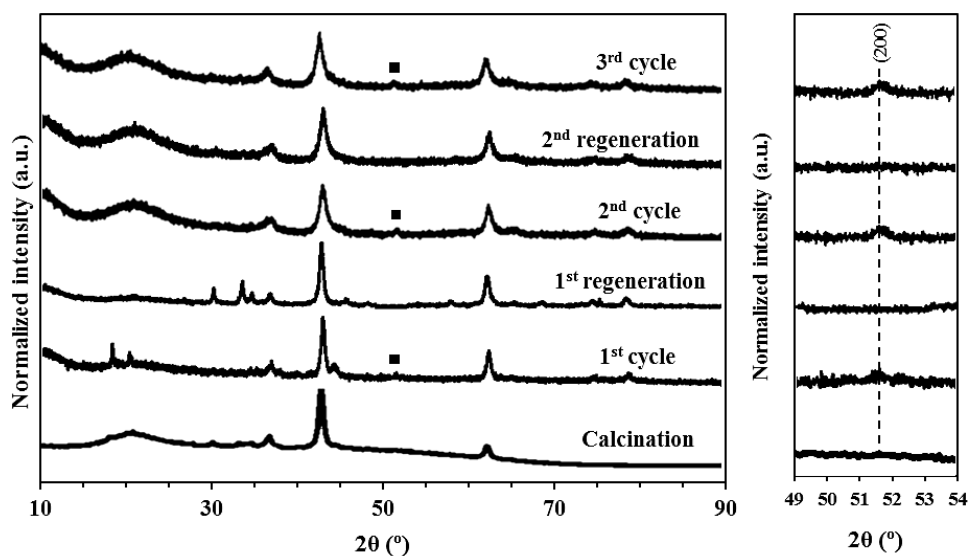
Figure 45 XRD patterns of NiFe-MgAl (Fe/Ni=0.2) used under different conditions.

CHAPTER VIII

Conclusions and recommendations

8.1 Conclusions

The results obtained from this work consists of simulation study for process comparison for H_2 production and experimental studies for development of suitable catalyst which are summarized in this chapter.

The process performance for hydrogen production from ethanol (conventional ESR, SESR, CLR and SECLR) were simulated and compared by focusing on maximum net hydrogen under basis of energy self-sufficient using NiO as oxygen carrier and CaO as CO_2 sorbent. The net hydrogen is the amount of hydrogen obtained after utilization for combustion equal to energy requirement. Different parameters (temperature, steam to ethanol ratio (*S/E*), solid to ethanol ratio and solid circulation) were varied to determine the optimal condition and energy requirement of each process. At their optimal condition, the processes with *in situ CO₂* separation (SESR and SECLR) offer better performance and enable operate at lower temperature with high hydrogen productivity and purity (up to 99%). The SECLR gives the maximum net hydrogen of 4.4 kmol/kmol and thermal efficiency of 86% as it provides better heat management which requires hydrogen only 12.5% of its production to sufficiently supply the lowest energy demand. The percentage of hydrogen utilization in other processes are 42%, 37.8% and 37.2% for conventional ESR, SESR and CLR, respectively, which is consistent with process's energy requirements and has a huge impact on net hydrogen.

In experimental work, the performance of iron-based oxygen carrier was investigated for hydrogen production. The performance of $Fe_2O_3/CaO-Al_2O_3$ multifunctional catalysts from SECLR was firstly examined. The result found that its activity depended on preparation method and iron content. Different phase formation and catalytic properties were observed from surface and textural characterization. The sol-gel method promoted the strong interaction of Fe-Ca by the formation of $Ca_2Fe_2O_5$ as the main phase but it can be improved by changing steps for adding iron precursor after acid peptization. The mechanical mixing method can suppress the formation of $Ca_2Fe_2O_5$. However, the partial densification of iron was observed leading to the lowest surface area. The similar performance for H_2 production was obtained in catalyst prepared by the sol-gel and mechanical mixing methods. The combination of iron oxide and calcium-alumina sorbent by impregnation method revealed better performance. The Imp5Fe/CaAl catalyst with 5 wt% Fe offered the best performance for SECLR to produce 70% of H_2 purity in pre-breakthrough period with the longest breakthrough time of 60 min and higher iron content cannot improve the H_2 production. Preparation with this method allowed the existence of $Ca_{12}Al_{14}O_{33}$ inert phase inside sorbent but also promoted the formation of $Ca_2Fe_2O_5$ phase. Moreover, the presence of both $Ca_{12}Al_{14}O_{33}$ inert support and $Ca_2Fe_2O_5$ phase in this material enhanced and stabilized the sorption capacity of CaO in the pre-breakthrough period of SECLR and oxygen carrier's performance of Fe_2O_3 in WS test leading to a stable material for at least 5 cycles. However, a decreased of its activity was observed in the subsequent 4th and 5th cycles which is ascribed to partial sintering during the phase transformation ($Fe_2O_3 \longrightarrow FeO/Fe^0 \longleftrightarrow Fe_3O_4$) and higher formation of other phases from strong

interaction between Fe-Ca. Therefore, to enhanced stability and developed performance of Fe-based oxygen carrier, the bimetallic NiFe-MgAl hydrotalcite-derived materials were studied and compared its performance with monometallic catalysts of Fe-MgAl and Ni-MgAl. From the result, all catalysts were successfully synthesized by co-precipitation method and employed as bifunctional catalyst in CLR of ethanol to produce hydrogen. At optimal condition of reforming temperature 500°C with *S/E* of 3, higher hydrogen selectivity about 80% were obtained in Ni modified catalysts. The NiFe-MgAl bimetallic catalyst exhibited much higher catalytic activity and stability than the corresponding monometallic Fe-MgAl and Ni-MgAl. After reaction test, the bimetallic catalyst observed the formation of NiFe alloy and coke with a lower crystallinity deposited on catalytic surface. The decreased in coke formation was due to (i) the Fe in NiFe alloy was partially oxidized to FeO, and (ii) the FeO intermediate reacted with deposited carbon and turn into NiFe realloy. The FeO redox cycle leads higher activity and resistance to coke deposition of this catalyst. In addition, the NiFe-MgAl offers a regenerable catalyst without a loss in catalytic performance during the catalyst regeneration over 10 repeated cycles of CLR process.

Finally, when considering the comparison of the performance of the multifunctional catalysts in the experimental works, it is very difficult to compare results of performance in hydrogen production because the studies were carried out under different conditions which influences activity, selectivity and stability of catalysts. However, the obtained experimental results of different nickel- and iron-based catalysts were summarized in Table 17. The catalysts' efficiencies expressed in terms of activity, stability and regenerability are indicated. It shows that NiFe-MgAl

exhibited very promising results under studied conditions with the highest activity and strongest resistance toward thermal and carbon deposition.

Table 17 Comparison of catalytic performance of various prepared catalysts for hydrogen production

Multifunctional catalyst	Preparation method	Metal loading (wt. %)	Reaction condition	H₂ purity (%)	Activity	Stability	Regenerability
5FeCaAl	Sol-gel			65	×	-	-
5Fe*CaAl					×	-	-
Mec5Fe/CaAl	Mechanical mixing	5	600°C, 2 g of catalyst, S/E=4, total flow rate = 50 ml min⁻¹, GHSV = 33.97 h⁻¹	64.8	×	-	-
Imp5Fe/CaAl	Impregnation				/	×	-
Imp10Fe/CaAl		10		70	×	-	-
Imp15Fe/CaAl		15			×	-	-
Fe-MgAl	Co-precipitation		500°C, 1 g of catalyst, S/E=3, total flow rate = 100 ml min⁻¹, GHSV = 26.21 h⁻¹	66.5	×	/	-
NiFe-MgAl		10		80.5	/	/	/
Ni-MgAl				81.3	/	×	-

8.2 Recommendations

This study has contributed to the understanding of process for efficient hydrogen production from ethanol and developing of materials (catalyst, sorbent and oxygen carrier) for enhancing process performance. As the study progressed, a few areas surfaced as suggested areas for future studies. The recommendations are as follows:

Table 18 Recommendations for future studies

Problems	Recommendations	Expectations
Process comparison	To assess the costs derived from each hydrogen production process such as capital investment, operating and utilities.	To support the owners and operators' financial decisions on the purchasing, installing and design of a plant.
	The error bar in chart should be added.	To indicate the error or uncertainty in a reported, i.e., how well the function describes the data.
H_2 production in SECLR step	The weight hourly space velocity (WHSV) can be varied.	To obtain optimal WHSV and more H_2 productivity.
	Several feed stocks such as methanol, glycerol, toluene, phenol and other hydrocarbons can be used.	To evaluate the feasibility of different fuels.
H_2 production in steam oxidation step	The operating condition such as water splitting temperature and steam feed flow rate can be varied.	To improve the maximum H_2 yield in this step.
Catalytic stability	The duration of the stability test should be extended until it is clearly seen the catalytic deactivation.	To obtain the catalyst lifetime.
Catalyst characterization	The investigation of metal dispersion on surface area supports should be estimated to obtain the number of active Ni sites, i.e., surface active metal sites for the reaction.	To describe the catalytic activity completely.

REFERENCES

[1]   Gielen D, Boshell F, Saygin D, Bazilian MD, Wagner N, Gorini R (2019) The role of renewable energy in the global energy transformation. Energy Strategy Reviews 24:38-50

[2]   Nikolaidis P, Poullikkas A (2017) A comparative overview of hydrogen production processes. Renewable and sustainable energy reviews 67:597-611

[3]   Hosseini SE, Wahid MA (2016) Hydrogen production from renewable and sustainable energy resources: promising green energy carrier for clean development. Renewable and Sustainable Energy Reviews 57:850-866

[4]   Hosseini SE, Abdul Wahid M, Jamil M, Azli AA, Misbah MF (2015) A review on biomass‑based hydrogen production for renewable energy supply. International journal of energy research 39 (12):1597-1615

[5]   Baykara SZ (2018) Hydrogen: a brief overview on its sources, production and environmental impact. International Journal of Hydrogen Energy 43 (23):10605-10614

[6]   Chattanathan SA, Adhikari S, Abdoulmoumine N (2012) A review on current status of hydrogen production from bio-oil. Renewable and Sustainable Energy Reviews 16 (5):2366-2372

[7]   Carotenuto G, Tesser R, Di Serio M, Santacesaria E (2013) Bioethanol as feedstock for chemicals such as acetaldehyde, ethyl acetate and pure hydrogen. Biomass Conversion and Biorefinery 3 (1):55-67

[8]   Dalena F, Senatore A, Iulianelli A, Di Paola L, Basile M, Basile A (2019) Ethanol from biomass: future and perspectives. In: Ethanol. Elsevier, pp 25-59

[9]   Chaubey R, Sahu S, James OO, Maity S (2013) A review on development of industrial processes and emerging techniques for production of hydrogen

from renewable and sustainable sources. Renewable and Sustainable Energy Reviews 23:443-462

[10]   Dutta S (2014) A review on production, storage of hydrogen and its utilization as an energy resource. Journal of Industrial and Engineering Chemistry 20 (4):1148-1156

[11]   Sharma YC, Kumar A, Prasad R, Upadhyay SN (2017) Ethanol steam reforming for hydrogen production: latest and effective catalyst modification strategies to minimize carbonaceous deactivation. Renewable and Sustainable Energy Reviews 74:89-103

[12]   Zheng Z, Sun C, Dai R, Wang S, Wu X, An X, Wu Z, Xie X (2017) Ethanol steam reforming on Ni-based catalysts: effect of Cu and Fe addition on the catalytic activity and resistance to deactivation. Energy & Fuels 31 (3):3091-3100

[13]   Abdelkader A, Daly H, Saih Y, Morgan K, Mohamed M, Halawy S, Hardacre C (2013) Steam reforming of ethanol over Co_3O_4–Fe_2O_3 mixed oxides. international journal of hydrogen energy 38 (20):8263-8275

[14]   Spath PL, Mann MK (2000) Life cycle assessment of hydrogen production via natural gas steam reforming. National Renewable Energy Lab., Golden, CO (US),

[15]   Vagia EC, Lemonidou AA (2008) Thermodynamic analysis of hydrogen production via autothermal steam reforming of selected components of aqueous bio-oil fraction. International Journal of Hydrogen Energy 33 (10):2489-2500

[16]   He L, Berntsen H, Chen D (2010) Approaching sustainable H_2 production: sorption enhanced steam reforming of ethanol. The Journal of Physical Chemistry A 114 (11):3834-3844

[17]   He L, Parra JMS, Blekkan EA, Chen D (2010) Towards efficient hydrogen production from glycerol by sorption enhanced steam reforming. Energy & Environmental Science 3 (8):1046-1056

[18]   Yancheshmeh MS, Radfarnia HR, Iliuta MC (2016) High temperature CO_2 sorbents and their application for hydrogen production by sorption enhanced steam reforming process. Chemical Engineering Journal 283:420-444

[19]   Dou B, Wang C, Song Y, Chen H, Jiang B, Yang M, Xu Y (2016) Solid sorbents for in-situ CO_2 removal during sorption-enhanced steam reforming process: A review. Renewable and Sustainable Energy Reviews 53:536-546

[20]   Cesário MR, Barros BS, Courson C, Melo DM, Kiennemann A (2015) Catalytic performances of Ni–CaO–mayenite in CO_2 sorption enhanced steam methane reforming. Fuel Processing Technology 131:247-253

[21]   Luis F, Ortiz M, Adánez J, García-Labiano F, Abad A, Gayán P (2008) Synthesis gas generation by chemical-looping reforming in a batch fluidized bed reactor using Ni-based oxygen carriers. Chemical Engineering Journal 144 (2):289-298

[22]   Rydén M, Lyngfelt A, Mattisson T (2006) Synthesis gas generation by chemical-looping reforming in a continuously operating laboratory reactor. Fuel 85 (12-13):1631-1641

[23]   Zheng Y, Li K, Wang H, Tian D, Wang Y, Zhu X, Wei Y, Zheng M, Luo Y (2017) Designed oxygen carriers from macroporous $LaFeO_3$ supported CeO_2 for

chemical-looping reforming of methane. Applied Catalysis B: Environmental 202:51-63

[24]   Imtiaz Q, Hosseini D, Müller CR (2013) Review of oxygen carriers for chemical looping with oxygen uncoupling (CLOU): thermodynamics, material development, and synthesis. Energy Technology 1 (11):633-647

[25]   Luo M, Yi Y, Wang S, Wang Z, Du M, Pan J, Wang Q (2018) Review of hydrogen production using chemical-looping technology. Renewable and Sustainable Energy Reviews 81:3186-3214

[26]   Diego Poza LFd, Ortiz Navarro M, García Labiano F, Adánez Elorza J, Abad Secades A, Gayán Sanz P (2009) Hydrogen production by chemical-looping reforming in a circulating fluidized bed reactor using Ni-based oxygen carriers.

[27]   Dueso C, Ortiz M, Abad A, García-Labiano F, Luis F, Gayán P, Adánez J (2012) Reduction and oxidation kinetics of nickel-based oxygen-carriers for chemical-looping combustion and chemical-looping reforming. Chemical Engineering Journal 188:142-154

[28]   Rydén M, Lyngfelt A, Mattisson T (2008) Chemical-looping combustion and chemical-looping reforming in a circulating fluidized-bed reactor using Ni-based oxygen carriers. Energy & Fuels 22 (4):2585-2597

[29]   Chen S, Shi Q, Xue Z, Sun X, Xiang W (2011) Experimental investigation of chemical-looping hydrogen generation using Al_2O_3 or TiO_2-supported iron oxides in a batch fluidized bed. international journal of hydrogen energy 36 (15):8915-8926

[30]   Chen S, Xiang W, Xue Z, Sun X (2011) Experimental investigation of chemical looping hydrogen generation using iron oxides in a batch fluidized bed. Proceedings of the Combustion Institute 33 (2):2691-2699

[31]   Kidambi PR, Cleeton JP, Scott SA, Dennis JS, Bohn CD (2012) Interaction of iron oxide with alumina in a composite oxygen carrier during the production of hydrogen by chemical looping. Energy & fuels 26 (1):603-617

[32]   Antzara A, Heracleous E, Lemonidou AA (2016) Energy efficient sorption enhanced-chemical looping methane reforming process for high-purity H_2 production: Experimental proof-of-concept. Applied Energy 180:457-471

[33]   Tippawan P, Thammasit T, Assabumrungrat S, Arpornwichanop A (2016) Using glycerol for hydrogen production via sorption-enhanced chemical looping reforming: thermodynamic analysis. Energy Conversion and Management 124:325-332

[34]   Pimenidou P, Rickett G, Dupont V, Twigg MV (2010) High purity H_2 by sorption-enhanced chemical looping reforming of waste cooking oil in a packed bed reactor. Bioresource technology 101 (23):9279-9286

[35]   Wang W (2014) Hydrogen production via sorption enhanced chemical looping reforming of glycerol using Ni-based oxygen carrier and Ca-based sorbent: Theoretical and experimental study. Korean Journal of Chemical Engineering 31 (2):230-239

[36]   Zhu L, Fan J (2015) Thermodynamic analysis of H_2 production from CaO sorption-enhanced methane steam reforming thermally coupled with chemical looping combustion as a novel technology. International Journal of Energy Research 39 (3):356-369

[37]   Cao A, Lu R, Veser G (2010) Stabilizing metal nanoparticles for heterogeneous catalysis. Physical Chemistry Chemical Physics 12 (41):13499-13510

[38]   Li D, Zeng L, Li X, Wang X, Ma H, Assabumrungrat S, Gong J (2015) Ceria-promoted Ni/SBA-15 catalysts for ethanol steam reforming with enhanced activity and resistance to deactivation. Applied Catalysis B: Environmental 176:532-541

[39]   Wang C, Dou B, Jiang B, Song Y, Du B, Zhang C, Wang K, Chen H, Xu Y (2015) Sorption-enhanced steam reforming of glycerol on Ni-based multifunctional catalysts. international journal of hydrogen energy 40 (22):7037-7044

[40]   Chanburanasiri N, Ribeiro AM, Rodrigues AE, Arpornwichanop A, Laosiripojana N, Praserthdam P, Assabumrungrat S (2011) Hydrogen production via sorption enhanced steam methane reforming process using Ni/CaO multifunctional catalyst. Industrial & engineering chemistry research 50 (24):13662-13671

[41]   Balat M, Balat H (2009) Recent trends in global production and utilization of bio-ethanol fuel. Applied energy 86 (11):2273-2282

[42]   The Crop Site (2010) Biofuel Production - Greater Shares of Commodities Used. [online] Available at: http://www.thecropsite.com/articles/1781/biofuel-production-greater-shares-of-commodities-used/ [Accessed 05.08.20]

[43]   RFA analysis of public and private data sources (2019) Focus Forward 2020 Pocket Guide to Ethanol [online] Available at: https://ethanolrfa.org/wp-content/ uploads/2020/02/2020-Outlook-Pocket-Guide-for-Web.pdf [Accessed 05.08.20]

[44]   Vizcaíno A, Carrero A, Calles J (2007) Hydrogen production by ethanol steam reforming over Cu–Ni supported catalysts. International Journal of Hydrogen Energy 32 (10-11):1450-1461

[45]   Mattos LV, Jacobs G, Davis BH, Noronha FB (2012) Production of hydrogen from ethanol: review of reaction mechanism and catalyst deactivation. Chemical reviews 112 (7):4094-4123

[46]   Haryanto A, Fernando S, Murali N, Adhikari S (2005) Current status of hydrogen production techniques by steam reforming of ethanol: a review. Energy & Fuels 19 (5):2098-2106

[47]   Wu Y-J, Li P, Yu J-G, Cunha A, Rodrigues A (2013) Sorption-enhanced steam reforming of ethanol on NiMgAl multifunctional materials: Experimental and numerical investigation. Chemical engineering journal 231:36-48

[48]   Da Silva AL, Müller IL (2011) Hydrogen production by sorption enhanced steam reforming of oxygenated hydrocarbons (ethanol, glycerol, n-butanol and methanol): thermodynamic modelling. International Journal of Hydrogen Energy 36 (3):2057-2075

[49]   Wu Y-J, Diaz Alvarado F, Santos JC, Gracia F, Cunha AF, Rodrigues AE (2012) Sorption-Enhanced Steam Reforming of Ethanol: Thermodynamic Comparison of CO_2 Sorbents. Chemical engineering & technology 35 (5):847-858

[50]   Diglio G, Bareschino P, Mancusi E, Pepe F (2016) Simulation of hydrogen production through chemical looping reforming process in a packed-bed reactor. Chemical Engineering Research and Design 105:137-151

[51]   Sengodan S, Lan R, Humphreys J, Du D, Xu W, Wang H, Tao S (2018) Advances in reforming and partial oxidation of hydrocarbons for hydrogen production

and fuel cell applications. Renewable and Sustainable Energy Reviews 82:761-780

[52]   Wang K, Dou B, Jiang B, Song Y, Zhang C, Zhang Q, Chen H, Xu Y (2016) Renewable hydrogen production from chemical looping steam reforming of ethanol using xCeNi/SBA-15 oxygen carriers in a fixed-bed reactor. International Journal of Hydrogen Energy 41 (30):12899-12909

[53]   Kale GR, Kulkarni BD, Bharadwaj K (2013) Chemical looping reforming of ethanol for syngas generation: a theoretical investigation. International journal of energy research 37 (6):645-656

[54]   García-Labiano F, De Diego L, García-Díez E, Serrano A, Abad A, Gayán P, Adánez J (2014) Combustion and reforming of ethanol in a chemical looping continuous unit. Energy Procedia 63:53-62

[55]   Hormilleja E, Durán P, Plou J, Herguido J, Peña J (2014) Hydrogen from ethanol by steam iron process in fixed bed reactor. International journal of hydrogen energy 39 (10):5267-5273

[56]   Nestl S, Voitic G, Lammer M, Marius B, Wagner J, Hacker V (2015) The production of pure pressurised hydrogen by the reformer-steam iron process in a fixed bed reactor system. Journal of power sources 280:57-65

[57]   Liu W, Shen L, Gu H, Wu L (2016) Chemical looping hydrogen generation using potassium-modified iron ore as an oxygen carrier. Energy & Fuels 30 (3):1756-1763

[58]   Bohn CD, Müller CR, Cleeton JP, Hayhurst AN, Davidson JF, Scott SA, Dennis JS (2008) Production of very pure hydrogen with simultaneous capture of carbon

dioxide using the redox reactions of iron oxides in packed beds. Industrial & engineering chemistry research 47 (20):7623-7630

[59]   Hafizi A, Rahimpour M, Heravi M (2019) Experimental investigation of improved calcium-based CO_2 sorbent and Co_3O_4/SiO_2 oxygen carrier for clean production of hydrogen in sorption-enhanced chemical looping reforming. International Journal of Hydrogen Energy 44 (33):17863-17877

[60]   Dou B, Zhang H, Cui G, Wang Z, Jiang B, Wang K, Chen H, Xu Y (2018) Hydrogen production by sorption-enhanced chemical looping steam reforming of ethanol in an alternating fixed-bed reactor: Sorbent to catalyst ratio dependencies. Energy Conversion and Management 155:243-252

[61]   Rydén M, Ramos P (2012) H2 production with CO_2 capture by sorption enhanced chemical-looping reforming using NiO as oxygen carrier and CaO as CO_2 sorbent. Fuel Processing Technology 96:27-36

[62]   Udomchoke T, Wongsakulphasatch S, Kiatkittipong W, Arpornwichanop A, Khaodee W, Powell J, Gong J, Assabumrungrat S (2016) Performance evaluation of sorption enhanced chemical-looping reforming for hydrogen production from biomass with modification of catalyst and sorbent regeneration. Chemical Engineering Journal 303:338-347

[63]   Phuluanglue A, Khaodee W, Assabumrungrat S (2017) Simulation of intensified process of sorption enhanced chemical-looping reforming of methane: comparison with conventional processes. Computers & Chemical Engineering 105:237-245

[64]   Yahom A, Powell J, Pavarajarn V, Onbhuddha P, Charojrochkul S, Assabumrungrat S (2014) Simulation and thermodynamic analysis of chemical

looping reforming and CO_2 enhanced chemical looping reforming. Chemical Engineering Research and Design 92 (11):2575-2583

[65]   Antzara A, Heracleous E, Bukur D, Lemonidou A (2015) Thermodynamic analysis of hydrogen production via chemical looping steam methane reforming coupled with in situ CO_2 capture. International Journal of Greenhouse Gas Control 32:115-128

[66]   Lyon RK, Cole JA (2000) Unmixed combustion: an alternative to fire. Combustion and Flame 121 (1-2):249-261

[67]   Kang K-S, Kim C-H, Bae K-K, Cho W-C, Kim S-H, Park C-S (2010) Oxygen-carrier selection and thermal analysis of the chemical-looping process for hydrogen production. International Journal of Hydrogen Energy 35 (22):12246-12254

[68]   Tang M, Xu L, Fan M (2015) Progress in oxygen carrier development of methane-based chemical-looping reforming: A review. Applied Energy 151:143-156

[69]   Protasova L, Snijkers F (2016) Recent developments in oxygen carrier materials for hydrogen production via chemical looping processes. Fuel 181:75-93

[70]   García-Labiano F, García-Díez E, de Diego LF, Serrano A, Abad A, Gayán P, Adánez J, Ruiz JAC (2015) Syngas/H_2 production from bioethanol in a continuous chemical-looping reforming prototype. Fuel Processing Technology 137:24-30

[71]   Zafar Q, Mattisson T, Gevert B (2005) Integrated hydrogen and power production with CO_2 capture using chemical-looping reforming redox reactivity

of particles of CuO, Mn_2O_3, NiO, and Fe_2O_3 using SiO_2 as a support. Industrial & engineering chemistry research 44 (10):3485-3496

[72] Wang K, Dou B, Jiang B, Zhang Q, Li M, Chen H, Xu Y (2016) Effect of support on hydrogen production from chemical looping steam reforming of ethanol over Ni-based oxygen carriers. international journal of hydrogen energy 41 (39):17334-17347

[73] Wei G, He F, Huang Z, Zhao K, Zheng A, Li H (2014) Chemical‐Looping Reforming of Methane Using Iron Based Oxygen Carrier Modified with Low Content Nickel. Chinese Journal of Chemistry 32 (12):1271-1280

[74] Hafizi A, Rahimpour M, Hassanajili S (2015) Calcium promoted Fe/Al_2O_3 oxygen carrier for hydrogen production via cyclic chemical looping steam methane reforming process. International Journal of Hydrogen Energy 40 (46):16159-16168

[75] Forutan H, Karimi E, Hafizi A, Rahimpour M, Keshavarz P (2015) Expert representation chemical looping reforming: A comparative study of Fe, Mn, Co and Cu as oxygen carriers supported on Al_2O_3. Journal of Industrial and Engineering Chemistry 21:900-911

[76] Yüzbasi NS, Kierzkowska A, Müller C (2017) Development of Fe_2O_3-based, Al_2O_3-stabilized oxygen carriers using sol-gel technique for H_2 production via chemical looping. Energy Procedia 114:436-445

[77] Hafizi A, Rahimpour M, Hassanajili S (2016) High purity hydrogen production via sorption enhanced chemical looping reforming: Application of $22Fe_2O_3/MgAl_2O_4$ and $22Fe_2O_3/Al_2O_3$ as oxygen carriers and cerium promoted CaO as CO_2 sorbent. Applied Energy 169:629-641

[78]   Li D, Koike M, Chen J, Nakagawa Y, Tomishige K (2014) Preparation of Ni–Cu/Mg/Al catalysts from hydrotalcite-like compounds for hydrogen production by steam reforming of biomass tar. International journal of hydrogen energy 39 (21):10959-10970

[79]   Yu X-P, Chu W, Wang N, Ma F (2011) Hydrogen production by ethanol steam reforming on NiCuMgAl catalysts derived from hydrotalcite-like precursors. Catalysis letters 141 (8):1228-1236

[80]   Wei G, Huang J, Fan Y, Huang Z, Zheng A, He F, Meng J, Zhang D, Zhao K, Zhao Z (2019) Chemical looping reforming of biomass based pyrolysis gas coupling with chemical looping hydrogen by using Fe/Ni/Al oxygen carriers derived from LDH precursors. Energy Conversion and Management 179:304-313

[81]   Lu H, Reddy EP, Smirniotis PG (2006) Calcium oxide based sorbents for capture of carbon dioxide at high temperatures. Industrial & engineering chemistry research 45 (11):3944-3949

[82]   Lu H, Khan A, Pratsinis SE, Smirniotis PG (2009) Flame-made durable doped-CaO nanosorbents for CO2 capture. Energy & Fuels 23 (2):1093-1100

[83]   Gruene P, Belova AG, Yegulalp TM, Farrauto RJ, Castaldi MJ (2011) Dispersed calcium oxide as a reversible and efficient CO_2- sorbent at intermediate temperatures. Industrial & engineering chemistry research 50 (7):4042-4049

[84]   Huang C-H, Chang K-P, Yu C-T, Chiang P-C, Wang C-F (2010) Development of high-temperature CO_2 sorbents made of CaO-based mesoporous silica. Chemical Engineering Journal 161 (1-2):129-135

[85]   Liu W, Feng B, Wu Y, Wang G, Barry J, Diniz da Costa JoC (2010) Synthesis of sintering-resistant sorbents for CO_2 capture. Environmental science & technology 44 (8):3093-3097

[86]   Zhou Z, Qi Y, Xie M, Cheng Z, Yuan W (2012) Synthesis of CaO-based sorbents through incorporation of alumina/aluminate and their CO_2 capture performance. Chemical Engineering Science 74:172-180

[87]   Osorio-Vargas P, Flores-González NA, Navarro RM, Fierro JL, Campos CH, Reyes P (2016) Improved stability of Ni/Al2O3 catalysts by effect of promoters (La_2O_3, CeO_2) for ethanol steam-reforming reaction. Catalysis Today 259:27-38

[88]   Yaakob Z, Bshish A, Ebshish A, Tasirin SM, Alhasan FH (2013) Hydrogen production by steam reforming of ethanol over nickel catalysts supported on sol gel made alumina: Influence of calcination temperature on supports. Materials 6 (6):2229-2239

[89]   Elias KF, Lucrédio AF, Assaf EM (2013) Effect of CaO addition on acid properties of Ni–Ca/Al_2O_3 catalysts applied to ethanol steam reforming. International Journal of Hydrogen Energy 38 (11):4407-4417

[90]   Abelló S, Bolshak E, Montane D (2013) Ni–Fe catalysts derived from hydrotalcite-like precursors for hydrogen production by ethanol steam reforming. Applied Catalysis A: General 450:261-274

[91]   Xu P, Zhou Z, Zhao C, Cheng Z (2016) Catalytic performance of Ni/CaO-$Ca_5Al_6O_{14}$ bifunctional catalyst extrudate in sorption-enhanced steam methane reforming. Catalysis Today 259:347-353

[92]   Phromprasit J, Powell J, Wongsakulphasatch S, Kiatkittipong W, Bumroongsakulsawat P, Assabumrungrat S (2016) Activity and stability

performance of multifunctional catalyst (Ni/CaO and Ni/Ca$_{12}$Al$_{14}$O$_{33}$-CaO) for bio-hydrogen production from sorption enhanced biogas steam reforming. International Journal of Hydrogen Energy 41 (18):7318-7331

[93]   Nimmas T, Jamrunroj P, Wongsakulphasatch S, Kiatkittipong W, Laosiripojana N, Gong J, Assabumrungrat S (2019) Influence of CaO precursor on CO$_2$ capture performance and sorption-enhanced steam ethanol reforming. International Journal of Hydrogen Energy 44 (37):20649-20662

[94]   Dou B, Zhang H, Cui G, Wang Z, Jiang B, Wang K, Chen H, Xu Y (2017) Hydrogen production and reduction of Ni-based oxygen carriers during chemical looping steam reforming of ethanol in a fixed-bed reactor. International Journal of Hydrogen Energy 42 (42):26217-26230

[95]   Silvester L, Antzara A, Boskovic G, Heracleous E, Lemonidou AA, Bukur DB (2015) NiO supported on Al$_2$O$_3$ and ZrO$_2$ oxygen carriers for chemical looping steam methane reforming. International Journal of Hydrogen Energy 40 (24):7490-7501

[96]   Hafizi A, Rahimpour M, Hassanajili S (2016) Hydrogen production via chemical looping steam methane reforming process: Effect of cerium and calcium promoters on the performance of Fe2O3/Al2O3 oxygen carrier. Applied Energy 165:685-694

[97]   Ashok J, Ang ML, Terence PZL, Kawi S (2016) Promotion of the Water-Gas-Shift Reaction by Nickel Hydroxyl Species in Partially Reduced Nickel-Containing Phyllosilicate Catalysts. ChemCatChem 8 (7):1308-1318

[98]   Lutz AE, Bradshaw RW, Keller JO, Witmer DE (2003) Thermodynamic analysis of hydrogen production by steam reforming. International Journal of Hydrogen Energy 28 (2):159-167

[99]   Engineering ToolBox, (2008). Combustion Processes and Combustion Efficiency. [online] Available at: https://www.engineeringtoolbox.com/combustion-process-efficiency-d_1025.html [Accessed 08.02.19].

[100]   Zamboni I, Courson C, Kiennemann A (2011) Synthesis of Fe/CaO active sorbent for CO_2 absorption and tars removal in biomass gasification. Catalysis today 176 (1):197-201

[101]   Engineering ToolBox, (2003). Optimal Combustion Process - Fuels and Excess Air. [online] Available at: https://www.engineeringtoolbox.com/fuels-combustion-efficiency-d_167.html [Accessed 08.02.19].

[102]   Krasnowski M, Grabias A, Kulik T (2006) Phase transformations during mechanical alloying of Fe–50% Al and subsequent heating of the milling product. Journal of alloys and compounds 424 (1-2):119-127

[103]   Phromprasit J, Powell J, Assabumrungrat S (2016) Metals (Mg, Sr and Al) modified CaO based sorbent for CO_2 sorption/desorption stability in fixed bed reactor for high temperature application. Chemical Engineering Journal 284:1212-1223

[104]   Sun X, Li J, Huang X, Sun C (2012) Recent advances in iron-catalyzed CH bond activation reactions. Current Inorganic Chemistry 2 (1):64-85

[105]   Handbook of Chemical Looping Technology. Wiley

[106]   Senin A, Kuznetsova O, Lykasov A (2006) Thermodynamic characteristic calculations for oxide melts by complete thermodynamic modeling. Russian journal of physical chemistry 80 (11):1773-1775

[107]   Jha A, Jeong D-W, Jang W-J, Lee Y-L, Roh H-S (2015) Hydrogen production from water–gas shift reaction over Ni–Cu–CeO$_2$ oxide catalyst: The effect of preparation methods. international journal of hydrogen energy 40 (30):9209-9216

[108]   Bian L, Wang W, Xia R, Li Z (2016) Ni-based catalyst derived from Ni/Al hydrotalcite-like compounds by the urea hydrolysis method for CO methanation. RSC advances 6 (1):677-686

[109]   Vedyagin AA, Mishakov I, Tsyrulnikov P (2016) The features of the CO disproportionation reaction over iron-containing catalysts prepared by different methods. Reaction Kinetics, Mechanisms and Catalysis 117 (1):35-46

[110]   Nogueira FGE, Assaf PG, Carvalho HW, Assaf EM (2014) Catalytic steam reforming of acetic acid as a model compound of bio-oil. Applied catalysis b: environmental 160:188-199

[111]   Zhu X, Zhang M, Li K, Wei Y, Zheng Y, Hu J, Wang H (2018) Chemical-looping water splitting over ceria-modified iron oxide: Performance evolution and element migration during redox cycling. Chemical Engineering Science 179:92-103

[112]   Chen Z-y, Bian L-z, Wang L-j, Yu Z-y, Zhao H-l, Li F-s, Chou K-c (2017) Topography, structure, and formation kinetic mechanism of carbon deposited onto nickel in the temperature range from 400 to 850° C. International Journal of Minerals, Metallurgy, and Materials 24 (5):574-583

APPENDIX

จุฬาลงกรณ์มหาวิทยาลัย
CHULALONGKORN UNIVERSITY

APPENDIX A

BLOCK COMPONENTS AND STREAM TABLE OF PROCESS SIMULATION

Table A.1 Summary of block components and stream for ESR process

Block	Model	Streams		Description
		Input	Output	
HX1		ETOH	FEED2	Ethanol preheating
HX2		FEED2	TOREFORM	Ethanol after temperature adjustment for steam reforming
HX3		H2O	HOTH2O	Water preheating
HX4		HOTH2O	STEAM	Steam production
HX5	HEATER	STEAM	SHSTEAM	Steam production
CL1		OUTREFOR	TOHTS	Products from reformer cooling down
CL2		OUTHTS	TOLTS	Products from HTS cooling down
CL3		OUTLTS	TOCOND	Products after temperature adjustment for separation
REFORMER		SHSTEAM / TOREFORM	OUTREFOR	H₂ production
HTS	RGIBBS	TOHTS	OUTHTS	Water-gas shift reaction for CO
LTS		TOLTS	OUTHTS	conversion
CONDENSE	Flash2	TOCOND	H2PROD	Water removal unit
			OUTCOND	Waste water
SPLT	FSPLT	H2PROD	H2NET	Amount of net H₂
			H2USED	Amount of H₂ utilization
FURNACE	RStoic	H2USED / AIR2	OUTFURNA	H₂ combustion for heat supply

Table A.2 Summary of block components and stream for SESR process

Block	Model	Streams		Description
		Input	Output	
HX1		ETOH	FEED2	Ethanol preheating
HX2		FEED2	TOREFORM	Ethanol after temperature adjustment for steam reforming
HX3	HEATER	H2O	HOTH2O	Water preheating
HX4		HOTH2O	STEAM	Steam production
HX5		STEAM	SHSTEAM	Steam production
REFORMER		SHSTEAM	OUTREFOR	H_2 production
		TOREFORM		
		RETOREFO		Regenerated CaO fed to reformer
	RGIBBS	TOCAL		$CaCO_3$ fed for calcination reaction
CALCINE		RETOCAL	OUTCAL	Regenerated CaO fed to calcination reactor for heat supply
		SWEEPGAS		CO_2 fed as sweep gas
CYCLONE1		OUTREFOR	H2H2O	Gas product stream
			TOCAL	Solid product stream of $CaCO_3$
CYCLONE2	CYCLONE	OUTCAL	CO2	CO_2 separated after calcination reaction
			OUTCY2	CaO after calcination reaction
SEP	Flash2	H2H2O	H2PROD	Water removal unit
			REWATER	Recycled water

Table A.2 Summary of block components and stream for SESR process (Cont.)

Block	Model	Streams		Description
		Input	Output	
SPLT	FSPLT	OUTCY2	RETOCAL	Regenerated CaO splitting for calcination reactor
			RETOREFO	Regenerated CaO splitting for reformer
SPLT2		CO2	SWEEPGAS	CO_2 splitting for sweep gas
			CO2TOATM	CO_2 to atmosphere
SPLT3		H2PROD	H2NET	Amount of net H_2
			H2USED	Amount of H_2 utilization
FURNACE	RStoic	H2USED AIR2	OUTFURNA	H_2 combustion for heat supply

Table A.3 Summary of block components and stream for CLR process

Block	Model	Streams		Description
		Input	Output	
HX1	HEATER	ETOH	FEED2	Ethanol preheating
HX2		FEED2	TOREFORM	Ethanol after temperature adjustment for steam reforming
HX3		H2O	HOTH2O	Water preheating
HX4		HOTH2O	STEAM	Steam production
HX5		STEAM	SHSTEAM	Steam production
REFORMER	RGIBBS	SHSTEAM	OUTREFOR	H_2 production
		TOREFORM		
		RETOREFO		Regenerated NiO fed to reformer
		TOAIR		Ni fed for air reaction
AIRREACT		RETOAIR	OUTAIR	Regenerated NiO fed to air reactor for heat supply
		AIR		Air fed as oxidant
CYCLONE1	CYCLONE	OUTREFOR	H2H2O	Gas product stream
			TOCAL	Solid product stream of Ni
CYCLONE2		OUTAIR	N2	N_2 separated after re-oxidation
			OUTCY2	NiO after re-oxidation
SEP	Flash2	H2H2O	H2PROD	Water removal unit
			REWATER	Recycled water

Table A.3 Summary of block components and stream for CLR process (Cont.)

Block	Model	Streams Input	Streams Output	Description
SPLT	FSPLT	OUTCY2	RETOAIR	Regenerated NiO splitting for air reactor
			RETOREFO	Regenerated NiO splitting for reformer
SPLT2		H2PROD	H2NET	Amount of net H_2
			H2USED	Amount of H_2 utilization
FURNACE	RStoic	H2USED AIR2	OUTFURNA	H_2 combustion for heat supply

Table A.4 Summary of block components and stream for SECLR process

Block	Model	Streams		Description
		Input	Output	
HX1		ETOH	FEED2	Ethanol preheating
HX2		FEED2	TOREFORM	Ethanol after temperature adjustment for steam reforming
HX3	HEATER	H2O	HOTH2O	Water preheating
HX4		HOTH2O	STEAM	Steam production
HX5		STEAM	SHSTEAM	Steam production
REFORMER		SHSTEAM	OUTREFOR	H_2 production
		TOREFORM		
		RETOREFO		Regenerated solids fed to reformer
		NINIOCAO		for hydrogen production and CO_2 adsorption
CALCINE	RGIBBS	NICACO3	OUTCAL	Ni and $CaCO_3$ fed for calcination reaction
		RETOCAL		Regenerated solids fed to calcination reactor for heat supply
		SWEEPGAS		CO_2 fed as sweep gas
AIRREACT		TOAIR	OUTAIR	Ni fed for re-oxidation at air reactor
		RETOAIR		Regenerated solids fed to air reactor for heat supply
		AIR		Air fed as oxidant
SEP	Flash2	H2H2O	H2PROD	Water removal unit
			REWATER	Recycled water
MIXER	MIX1	REWATER	MIXH2O	Mixing between water and recycled water
		H2O		

Table A.4 Summary of block components and stream for SECLR process **(Cont.)**

Block	Model	Streams		Description
		Input	Output	
CYCLONE1		OUTREFOR	H2H2O	Gas product stream
			NICACO3	Solid product stream of Ni and CaCO$_3$
CYCLONE2	CYCLONE	OUTCAL	CO2	CO$_2$ separated after calcination reaction
			OUTCY2	Solids after calcination reaction (Ni, NiO and CaO)
CYCLONE3		OUTAIR	N2	N$_2$ separated after re-oxidation
			OUTCY3	Solids after oxidation reaction (NiO and CaO)
SPLT		OUTCY2	NINIOCAO	Regenerated solids splitting to reformer
			TOAIR	Solids after calcination reaction and fed to air reactor for Ni regeneration to NiO
SPLT2	FSPLT	NIOCAO	RETOCAL	Regenerated solids splitting for calcination reactor
			RETOREFO	Regenerated solids splitting for reformer
SPLT3		CO2	SWEEPGAS	CO$_2$ splitting for sweep gas
			CO2TOATM	CO$_2$ to atmosphere
SPLT4		H2PROD	H2NET	Amount of net H$_2$
			H2USED	Amount of H$_2$ utilization

APPENDIX B

CALCULATION FOR CATALYST PREPARATION

B.1 Metal precursor calculation

For Fe_2O_3/CaO-Al_2O_3 multifunctional catalysts with a mass ratio of calcium to alumina of 70:30 and normalized with 5 wt% of iron, based on 10 gram of sample:

Fe	55.845 g/mol	in $Fe(NO_3)_3 \cdot 9H_2O$	404 g/mol
Fe	0.5 g	in $Fe(NO_3)_3 \cdot 9H_2O$	3.617 g = 0.009 mol
Ca	40.078 g/mol	in $Ca(CH_3COO)_2 \cdot H_2O$	158.17 g/mol
Ca	6.65 g	in $Ca(CH_3COO)_2 \cdot H_2O$	26.25 g = 0.166 mol
Al	26.981 g/mol	in $Al(NO_3)_3 \cdot 9H_2O$	375.13 g/mol
Al	2.85 g	in $Al(NO_3)_3 \cdot 9H_2O$	39.625 g = 0.106 mol

B.2 Citric acid and DI water calculation

1 mole of metal precursor: 1.2 mole of citric acid

So, using citric acid of 0.337 mol = 70.85 g

And, 1 mole of citric acid: 50 mole of DI water

So, using DI water of 16.855 mol = 304.3 ml

B.3 Calculation for synthesis of hydrotalcite-like compounds

For Fe-Ni-Mg-Al HTcls catalysts with 10 wt% of nickel and iron, based on 5 gram of sample:

Ni	58.693 g/mol	in $Ni(NO_3)_2 \cdot 6H_2O$	290.8 g/mol	
Ni	0.4 g	in $Ni(NO_3)_2 \cdot 6H_2O$	1.98 g = 0.0068 mol	
Fe	55.845 g/mol	in $Fe(NO_3)_3 \cdot 9H_2O$	404 g/mol	
Fe	0.1 g	in $Fe(NO_3)_3 \cdot 9H_2O$	0.72 g = 0.0018 mol	

From molar ratio of divalent metals (Ni^{2+} and Mg^{2+}) to trivalent metals (Fe^{3+} and Al^{3+}) equal to 2 with a concentration of all precursors of 1 M, yield

|				
Al	0.031 mol	in $Al(NO_3)_3 \cdot 9H_2O$	11.84 g	
and Mg	0.06 mol	in $Mg(NO_3)_2 \cdot 6H_2O$	15.35 g	
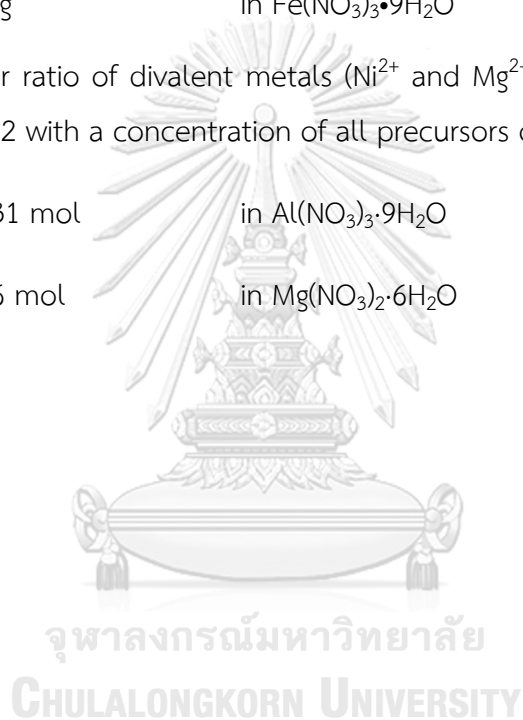
APPENDIX C

CALIBRATION CURVES

The instrument of gas chromatography (GC-8A SHIMADZU) with two detectors: flame ionization detector (FID) and thermal conductivity detector (TCD) equipped with two columns: Molecular sieve 5A and PoraPLOT Q are calibrated which shows the operating conditions for gas chromatography in Table C. 1. The calibration involves the preparation of a set of gas standards containing a known amount of the analyte of interest, measuring the peak area from instrument response for each standard and establishing the relationship between the peak area and mole of analytic gas. The calibration curves are shown in Figures C.1-C.7 for H_2, CO_2, CO, CH_4, N_2, O_2 and C_2H_5OH respectively.

Table C.1 Operating conditions for gas chromatography

Gas Chromatography	Shimadzu GC-8A		
Detector	TCD		FID
Column	Molecular sieve 5A	PoraPLOT Q	Inert cap WAX
- Material	SUS	SUS	Mixture
- Length (m)	2	2	60
- Outer diameter (mm)	4	4	0.32
- Inner diameter (mm)	3	3	1×10^{-3}
- Mesh range	60/80	60/80	n.a.
- Maximum temperature (^{o}C)	350	350	280
Carrier gas	Ar (99.999%)	Ar (99.999%)	He (99.999%)
Column temperature (^{o}C)			
- Initial	50	50	50
- Final	50	50	250
Injector temperature (^{o}C)	70	70	180
Detector temperature (^{o}C)	150	150	50
Current (mA)	70	70	n.a.
Analyzed gas	H_2, N_2, O_2, CH_4, CO	CO_2	C_2H_5OH
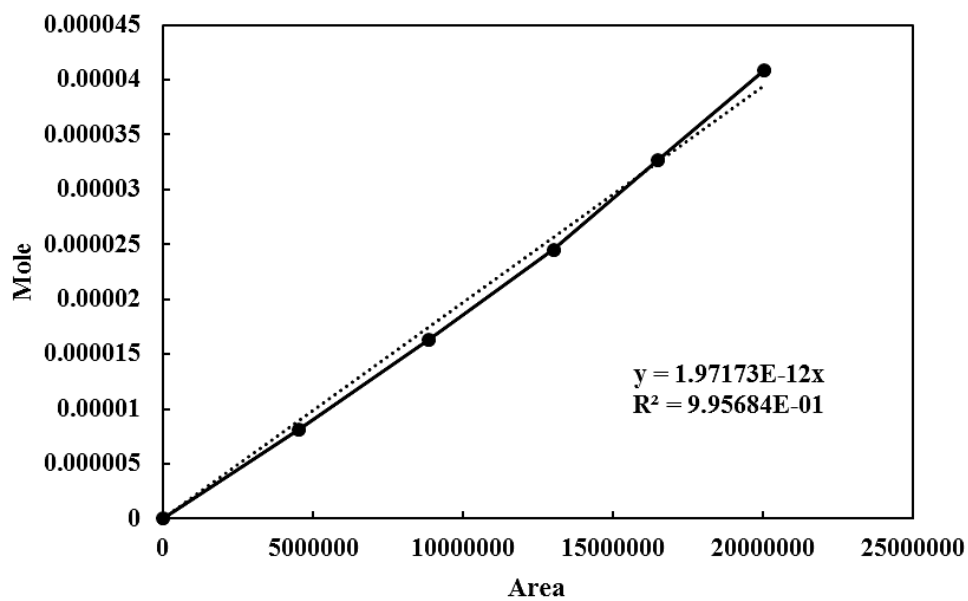
Figure C.1 H_2 Calibration curve
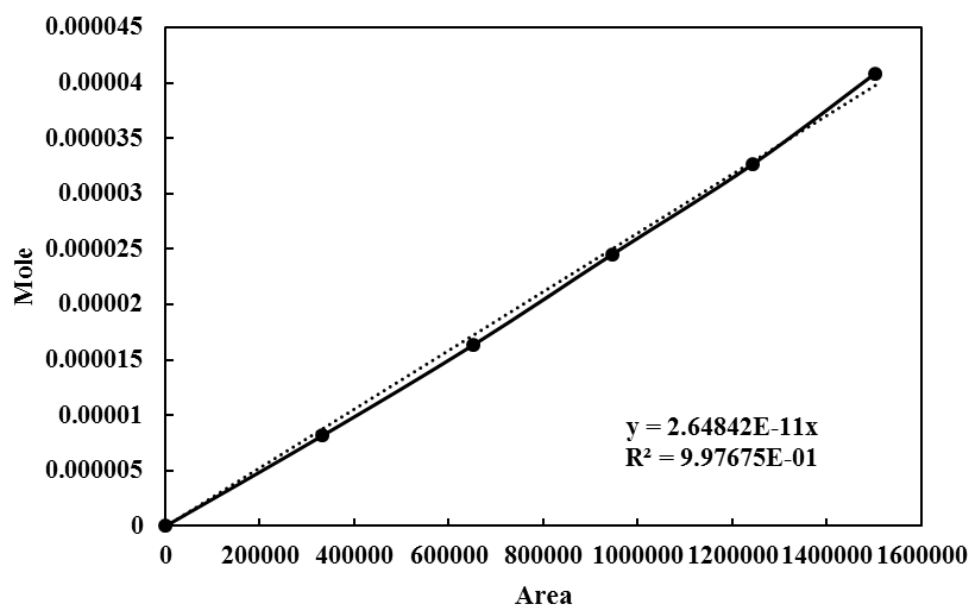
Figure C.2 CO_2 Calibration curve
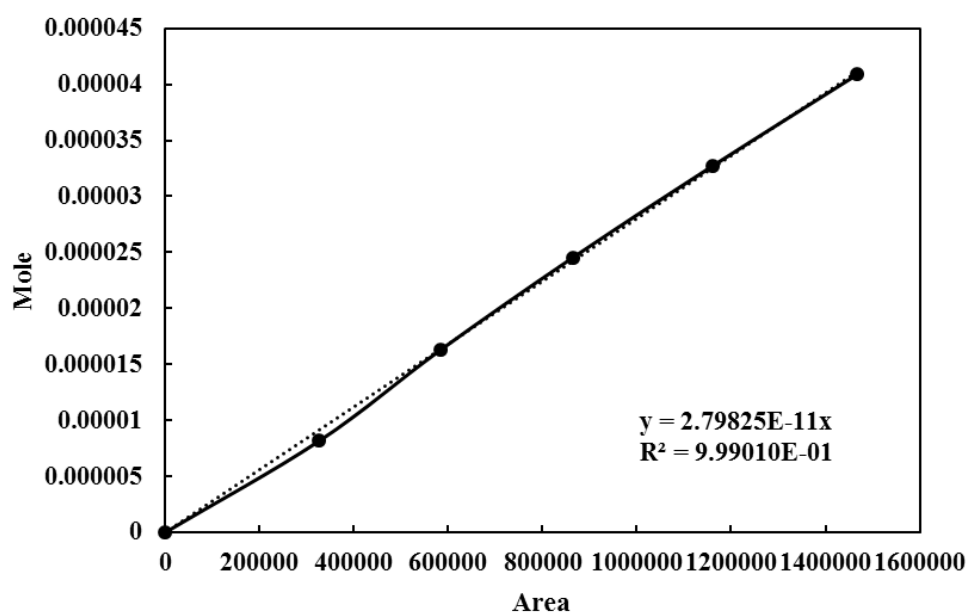
Figure C.3 CO Calibration curve
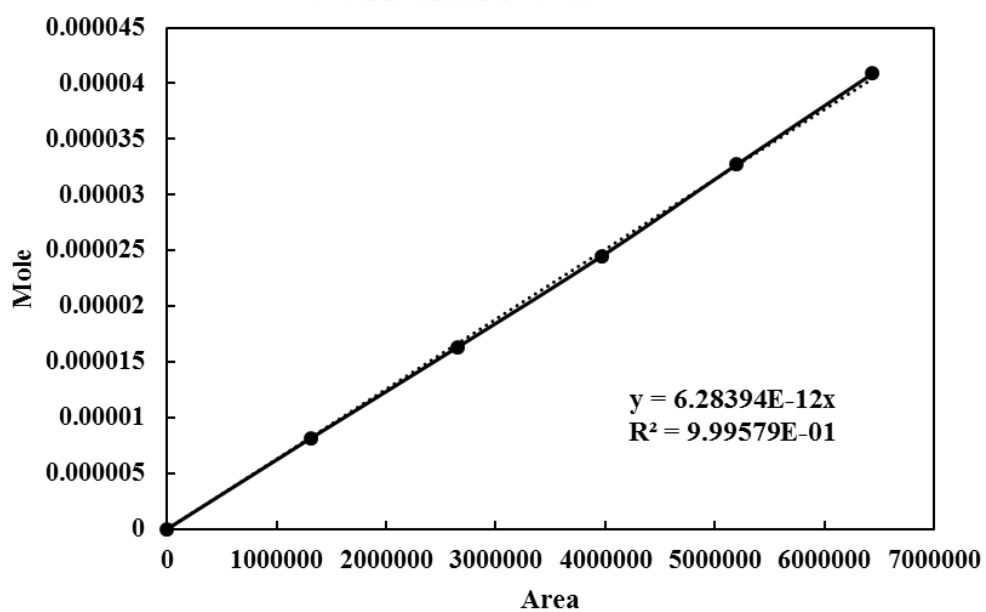
Figure C.4 CH$_4$ Calibration curve
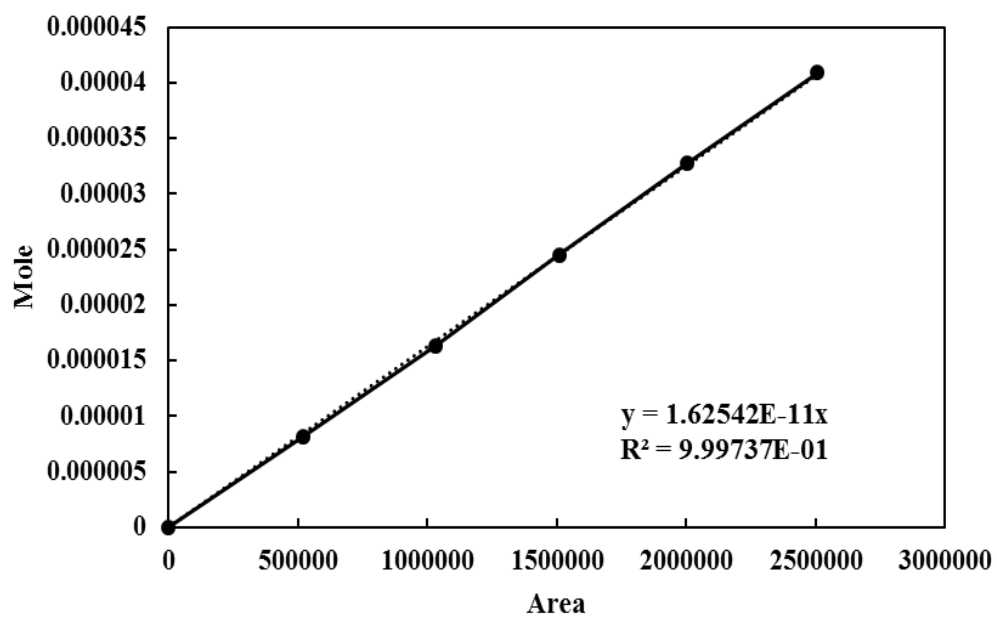
Figure C.5 N_2 Calibration curve
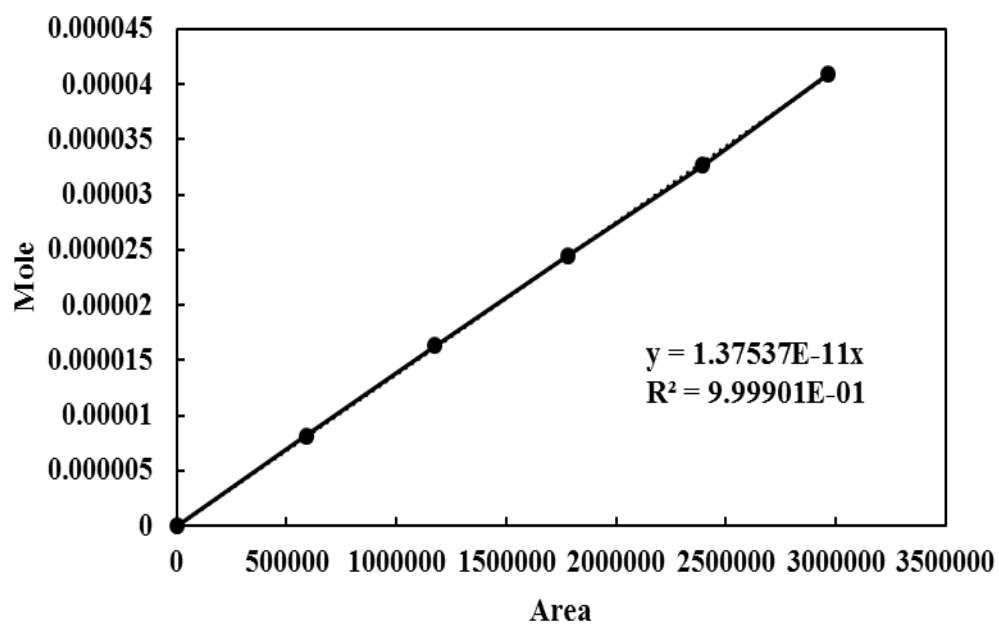
Figure C.6 O_2 Calibration curve
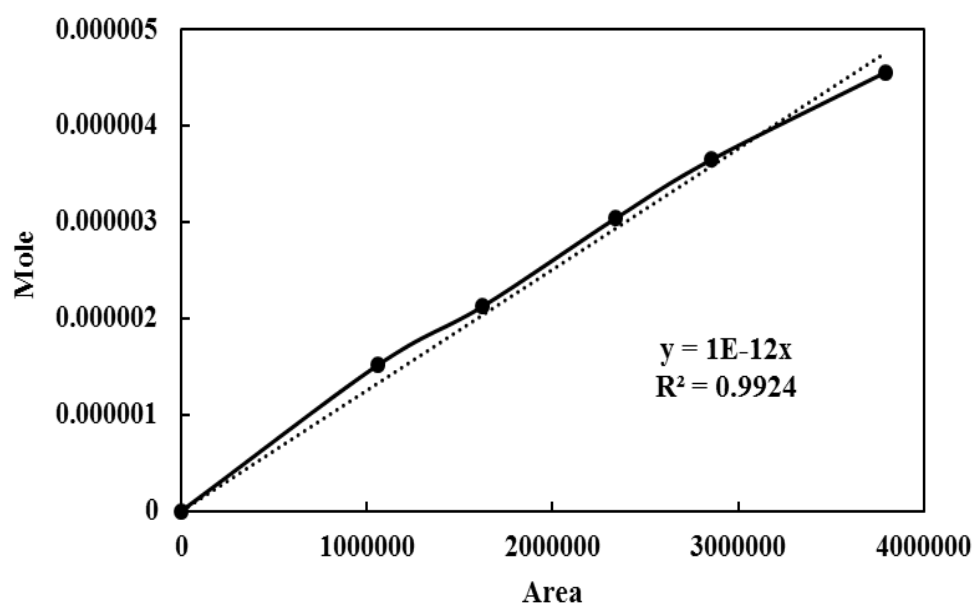
Figure C.7 C_2H_5OH Calibration curve

จุฬาลงกรณ์มหาวิทยาลัย

CHULALONGKORN UNIVERSITY

VITA

NAME	Janenipa Saupsor
DATE OF BIRTH	25 September 1992
PLACE OF BIRTH	Bangkok, Thailand
INSTITUTIONS ATTENDED	Phrapathom Witthayalai School (Science - Mathematics Bilingual Program: SMBP)
	Bachelor's degree of Chemical Engineering, Faculty of Engineering and Industrial Technology, Silpakorn University
HOME ADDRESS	449/42 Pipit Prasart Road, Phra Pathom Chedi Sub-district, Mueang Nakhon Pathom District, Nakhon Pathom 73000
PUBLICATION	1. J. Saupsor, N. Kasempremchit, P. Bumroongsakulsawat, P. Kim-Lohsoontorn, S. Wongsakulphasatch, W. Kiatkittipong, N. Laosiripojana, J. Gong, S. Assabumrungrat (2020) Performance comparison among different multifunctional reactors operated under energy self-sufficiency for sustainable hydrogen production from ethanol. International Journal of Hydrogen Energy, 45(36), 18309-18320.
	2. J. Saupsor, S. Wongsakulphasatch, P. Kim-Lohsoontorn, W. Kiatkittipong P. Bumroongsakulsawat, S. Ratchahat, S. Charojrochkul, J. Gong, S. Assabumrungrat (2020) Fe_2O_3/CaO-Al_2O_3 multifunctional catalyst for hydrogen production by sorption enhanced chemical looping reforming of ethanol. Biomass Conv. Bioref. (2020). https://doi.org/10.1007/s13399-020-00947-z
AWARD RECEIVED	First-class honors in bachelor's degree of Chemical Engineering